

2021

## Biocompatible and Multifunctional Trityl Spin Probes for Electron Paramagnetic Resonance Spectroscopy

Teresa D. Gluth

West Virginia University, [tdg0013@mix.wvu.edu](mailto:tdg0013@mix.wvu.edu)

Follow this and additional works at: <https://researchrepository.wvu.edu/etd>

 Part of the [Biochemistry Commons](#), [Medicinal-Pharmaceutical Chemistry Commons](#), [Organic Chemistry Commons](#), and the [Other Analytical, Diagnostic and Therapeutic Techniques and Equipment Commons](#)

---

### Recommended Citation

Gluth, Teresa D., "Biocompatible and Multifunctional Trityl Spin Probes for Electron Paramagnetic Resonance Spectroscopy" (2021). *Graduate Theses, Dissertations, and Problem Reports*. 8313.  
<https://researchrepository.wvu.edu/etd/8313>

This Thesis is protected by copyright and/or related rights. It has been brought to you by the The Research Repository @ WVU with permission from the rights-holder(s). You are free to use this Thesis in any way that is permitted by the copyright and related rights legislation that applies to your use. For other uses you must obtain permission from the rights-holder(s) directly, unless additional rights are indicated by a Creative Commons license in the record and/ or on the work itself. This Thesis has been accepted for inclusion in WVU Graduate Theses, Dissertations, and Problem Reports collection by an authorized administrator of The Research Repository @ WVU. For more information, please contact [researchrepository@mail.wvu.edu](mailto:researchrepository@mail.wvu.edu).

**Biocompatible and Multifunctional Trityl Spin Probes for Electron Paramagnetic Resonance Spectroscopy**

**Teresa D. Gluth**

**Thesis submitted  
to the School of Medicine  
at West Virginia University**

**in partial fulfillment of the requirements for the degree of**

**Masters of Science in  
Biomedical Sciences**

**Benoit Driesschaert, Ph.D., Chair  
Valery V. Khrantsov, Ph.D.  
Timothy D. Eubank, Ph.D.  
Mark L. McLaughlin, Ph.D.**

**Department of Biomedical Sciences**

**Morgantown, West Virginia  
2021**

**Keywords: EPR, electron paramagnetic resonance, trityl, triarylmethyl, pTAM, HOPE, HOPE71, oxygen, pH, inorganic phosphate, tumor microenvironment, extracellular  
Copyright 2021 Teresa D. Gluth**

## ABSTRACT

### Biocompatible and Multifunctional Trityl Spin Probes for Electron Paramagnetic Resonance Spectroscopy

Teresa D. Gluth

The primary objective of my thesis was to develop and utilize a biocompatible multifunctional trityl spin probe for concurrent measurement of  $pO_2$ ,  $pH_e$ , and  $[P_i]$  in vivo by electron paramagnetic resonance (EPR) spectroscopy (Chapter 2). My first goal was to synthesize the proposed probe we are terming HOPE71. Secondly, HOPE71 was characterized by X-band and L-band EPR spectroscopy. Next, the biocompatibility of HOPE71 was assessed through an albumin binding test, cytotoxicity assays, and in vivo intravenous tolerance. Then, the use of HOPE71 to measure the target parameters was demonstrated in a breast cancer mouse model. In tandem, I developed an application for user friendly fitting of the EPR spectrum of HOPE71 and the related monophosphated probe, pTAM (Chapter 3). Lastly, to demonstrate further skill in synthesis of trityl spin probes, I worked in collaboration with the Saxena lab at the University of Pittsburgh to develop a hydrophilic spin probe with a maleimide linker for structural biology studies using site directed spin labeling and dipolar EPR spectroscopy (Chapter 4).

## Table of Contents

<b>ABSTRACT</b> .....	ii
<b>CHAPTER 1 – Multi-Parameter Assessment of the Tumor Microenvironment (Review)</b> .....	1
<b>CHAPTER 2 – Biocompatible Monophosphonated Trityl Spin Probe, HOPE71, for In Vivo Measurement of <math>pO_2</math>, pH, and <math>[P_i]</math> in Mouse Tumors by Electron Paramagnetic Resonance Spectroscopy</b> .....	12
<b>CHAPTER 3 – Large-Scale Synthesis of a Monophosphonated Tetrathiatriarylmethyl Spin Probe for concurrent <i>in vivo</i> measurement of <math>pO_2</math>, pH and inorganic phosphate by EPR</b> .....	25
<b>CHAPTER 4 – Cleavage-resistant Protein Labeling with Hydrophilic Trityl Enables Distance Measurements <i>In-Cell</i></b> .....	31

## CHAPTER 1 – Multi-Parameter Assessment of the Tumor Microenvironment (Review)

### 1. Introduction/Abstract

The tumor microenvironment (TME) contains important elements for understanding tumorigenesis and therapy resistance. Three markers characteristic of the tumor microenvironment are hypoxia (low  $pO_2$ ), acidosis (low  $pH_e$ ), and elevated inorganic phosphate concentration [ $P_i$ ]. These attributes are vital to study cancer as they relate to the mechanisms of tumor growth, the aggressiveness of the cancer, and the response to therapy. There are various methods for measuring each of these parameters individually, each with benefits and drawbacks. One notable method is electronic paramagnetic resonance (EPR) spectroscopy utilizing pTAM, a monophosphonated trityl radical, which allows for concurrent, non-invasive measurement of  $pO_2$ ,  $pH$ , and [ $P_i$ ] for in vivo applications.

### 2. Tumor Microenvironment

With its complexity, prevalence, and burden on society, cancer is and will continue to be a significant and essential topic in research, and studying the tumor microenvironment (TME) is vital for understanding tumorigenesis and therapeutic response<sup>1, 2</sup>. The TME is a complex network of various immune and fibroblast cells, vasculature, and extracellular matrix<sup>2</sup>. Its characteristics are both affected by and affecters of the tumor story. Two physiological parameters of the TME, hypoxia and acidosis, are well-defined hallmarks of solid tumor development and play considerable roles in tumorigenesis and treatment resistance. More recently, high inorganic phosphate concentration was also identified as a tumor marker that may also indicate metastatic character<sup>3</sup>.

#### 2.1 Hypoxia

Oxygen is vital for normal metabolic function in the cell, and therefore, adequate oxygen supply to the tissue is essential for maintaining homeostasis. Tissue oxygenation ( $pO_2$ ) is a measurement of the net supply and demand of oxygen. An inadequate amount of oxygen to the body or specific tissue leads to hypoxia. Normal tissue oxygenation can range from approximately 10 to 70 mmHg, while hypoxia is defined as oxygen levels below 10 mmHg<sup>4-6</sup>. Hypoxia is a well-established hallmark of solid tumors, with the initial observation made over 60 years ago<sup>7</sup>, and the association has been verified across many types of cancer. The overall average oxygenation and the fraction of normoxic regions are considerably lower in tumors when compared to their corresponding tissue<sup>5</sup>.

Tumor hypoxia is caused by an imbalance between oxygen delivery and consumption. The high rates of metabolism and proliferation in cancer cells create higher demands for oxygen, while tumor vasculature fails to deliver sufficient and consistent oxygen<sup>8</sup>. There are two primary types of oxygen deprivation: chronic or diffusion-limited hypoxia, which is due to an increasing distance between blood vessels and cells, and acute or perfusion-limited hypoxia, which is caused by a temporary drop in blood flow<sup>9</sup>.

Tumor hypoxia has several consequences on tumorigenesis and therapeutic response. Evidence shows that a hypoxic environment may be present early in pre-malignant lesions due to the basal membrane limiting oxygen supply<sup>10</sup>. This creates a selected pressure towards cells resistant to hypoxia-induced apoptosis<sup>10</sup>. Hypoxia has also been associated with a more metastatic character due to two main effects: (1) continued selective pressure that can lead to greater survival of more aggressive cells, (2) hypoxia-induced expression of genes that leads to metastases<sup>8, 10, 11</sup>. Also, hypoxia can lead to recruitment of inflammatory cells and reprogramming of the inflammatory pathways that promote the tumor's ability to escape immune patrolling, proliferate, remodel the extracellular matrix, and migrate<sup>12, 13</sup>.

An additional major consequence of hypoxia is resistance to standard therapy, such as radiation and some chemotherapies. The radiosensitivity of a tumor is related to the oxygenation through the oxygen enhancement effect or oxygen enhancement ratio (OER)<sup>14</sup>. Radiation in the presence of oxygen creates oxygen-centered free radicals while damaged mitochondria leak more reactive oxygen species (ROS), both of which increase the DNA damage<sup>15</sup>. Consequently, hypoxic tissue requires up to three times more radiation dose than normoxic tissue for the same therapeutic effect<sup>14, 16</sup>. Hypoxic tumor cells can also be less sensitive to chemotherapy, which generally targets rapidly dividing cells, because of slowed proliferation from lack of nutrition<sup>8</sup>. The gene expression selected and induced by hypoxia can also protect cells from chemotherapy through loss of apoptosis<sup>8</sup>.

## 2.2 Acidosis

Another important chemical parameter in physiologic homeostasis is pH. Intracellular pH ( $pH_i$ ) is around 7.2 and tightly regulated to preserve normal intracellular metabolism and function<sup>17, 18</sup>. The pH of the blood and the interstitial space ( $pH_e$ ) of healthy tissue is generally around 7.4<sup>19</sup>. Systemically, the pH is maintained by the lungs and kidneys. Acidosis occurs when the tissue  $pH_e$  is more acidic, in the range of 6.5 to 6.9, and has been repeatedly associated with solid tumors for several decades<sup>20</sup>. In malignant tissue, there is an imbalance in increased proton secretion and poor proton removal. Cancer cells demonstrate a high rate of glycolysis to meet the high energy demands of a growing tumor<sup>21</sup>. An increased dependency on glycolysis can be a result of hypoxia, but glycolysis has been shown to persist even in well-oxygenated conditions, which suggests a high growth adaptation selected by intermittent hypoxia in the early stages of tumor development<sup>10</sup>. High rates of glycolysis create great amounts of lactate, which is exported from the cell along with protons<sup>22</sup>. As discussed earlier, the vasculature and perfusion of a tumor is often irregular and ineffective, and therefore, may not efficiently remove the buildup of protons.

Acidosis creates further selective pressure toward cells that are more resistant to acidic environments. It has also been associated with more aggressive and metastatic capabilities, possibly due to enhanced angiogenesis and degradation of the cellular matrix<sup>10</sup>. The acidic  $pH_e$  can have consequences on therapeutic response, especially when using chemotherapeutics with  $pK_a$  values around 6-8 because the increased protonation can alter the absorption, metabolism, and mechanism of action.

## 2.3 Inorganic Phosphate

Inorganic phosphate ( $P_i$ ) is a major building block in nucleotides of DNA and RNA and phospholipids in cellular membranes. Phosphates are also an essential component of metabolism, with ADP and ATP acting as the main energy exchange source for cellular processes. Additionally, phosphorylation and dephosphorylation, or esterification and hydrolysis of phosphate groups on organic macromolecules, play vital roles in many enzymatic reactions and signaling mechanisms. More recently, an increased concentration of inorganic phosphate in the extracellular space was reported as a tumor marker in mice, differing from healthy tissue even more dramatically than  $pO_2$  and  $pH_e$ <sup>3</sup>. Also, serum from patients with cancer had more than twice the amount of phosphorus from  $P_i$  than healthy patients<sup>23, 24</sup>. A major theory for this observation is related to the growth rate hypothesis (GRH), indicating that the tumor requires greater amounts of phosphorus to make components for excess proliferation<sup>25</sup>.  $P_i$  also may play a role in metastatic mechanisms as the concentration of interstitial phosphate has demonstrated a direct correlation with the metastatic potential of the cancer<sup>3</sup>. One aspect of the metastatic potential may be explained by the increased uptake of  $P_i$  which may enhance the ability of malignant cells to migrate and adhere<sup>26</sup>. The effects of phosphate on therapeutic response are still unclear, with studies showing differing results.

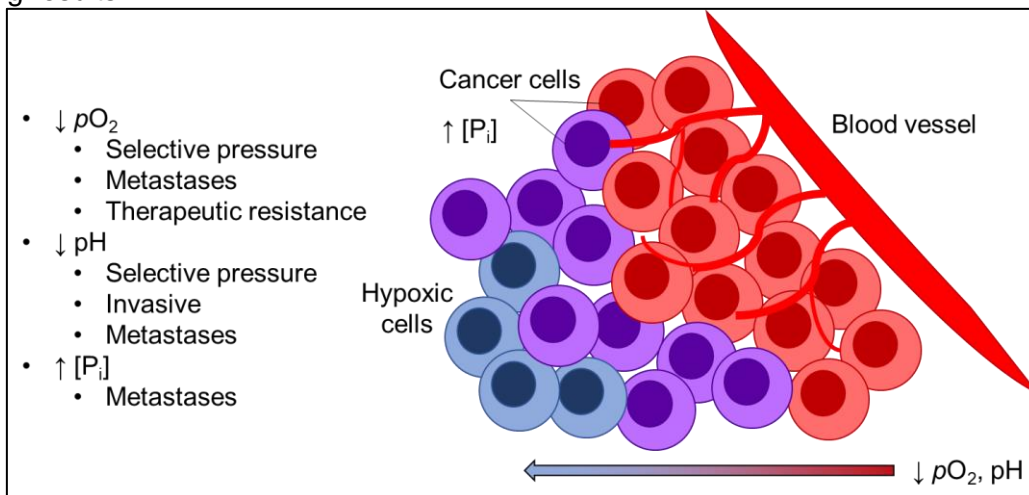


**Figure 1.** Summarized diagram of  $pO_2$ , pH, and  $[P_i]$  in the tumor microenvironment.

## 2.4 Importance for measurement and correlation

Hypoxia, acidosis, and elevated  $[P_i]$  are all strong indicators of malignancy, and they appear to have both cause-and-effect roles in tumor growth and aggression. Measurement of these parameters can be an instrumental tool in cancer research and therapy—studying the many mechanisms in tumorigenesis and metastasis, predicting outcomes, and optimizing therapeutic interventions. The ability to measure all three,  $pO_2$ ,  $pH_e$ , and  $[P_i]$ , unlocks even more potential investigations regarding the correlation between the variables.

Because these parameters can have significant temporal and special variance, more accurate correlation analysis would require the measurements to be made simultaneously and from the same location.

### 3 Measurement Techniques

There are currently methods for measuring each of these parameters in tissue independently. All these methods have their strengths and weaknesses. To the best of our knowledge, the only technique that allows for the simultaneous measurement of all three parameters of interest in vivo is Electron Paramagnetic Resonance (EPR) paired with a multifunctional radical probe. The following paragraphs aim at providing a short overview of the main techniques to measure  $pO_2$ , pH, and [P.] in vivo.

#### 3.1 Oxygen Measurement

There are quite a few methods for measuring tissue oxygenation in vivo. One of the most common methods for measuring  $pO_2$  is the Eppendorf polarographic electrode. This method can be used for in vivo tissue measurement using a microelectrode. However, this technique is invasive and consumes oxygen, which does not allow for repeated measurements in the same location<sup>8</sup>. Currently, there is no oxygen electrode available and suitable for clinical measurement of tumors<sup>5</sup>.

Another common oxygen sensing technique involves the use of a fiber-optic probe that measures oxygen-dependent fluorescence quenching. This method has the advantage of high sensitivity at low oxygen partial pressures and does not require regular calibration but is also invasive as it requires the insertion of the probe into the area of interest.<sup>8</sup> A related optical method utilizes oxygen-dependent phosphorescence quenching of a phosphorescent agent that can be injected in vivo. This method allows for tissue oxygenation measurement to only a few millimeters depth because of the light penetration ability, but some methods and agents have been developed to utilize deeper penetrating X-rays<sup>5</sup>.

Some drugs or markers selectively respond to hypoxic tissue. Bioreductive markers, such as those containing a 2-nitroimidazole moiety, are reduced selectively by hypoxic cells<sup>8</sup>. The reduced form covalently binds to thiols or amines of cellular components and therefore accumulates in hypoxic tissues. Pimonidazole (Hypoxyprobe) is a popular biomedical tool to image hypoxic tissue ex-vivo. However, this method requires hours of consistent hypoxia to viable cells<sup>5</sup>. PET tracers containing a nitroimidazole (e.g., [<sup>18</sup>F]FAZA) are used clinically to track hypoxic regions non-invasively<sup>27</sup>.

One way to indirectly measure tissue oxygenation is to measure oxygen in the blood. There is a strong relationship between the  $pO_2$  in the blood and the oxygen saturation of hemoglobin (Hb), so techniques that can detect differences between oxyhemoglobin (HbO<sub>2</sub>) and deoxyhemoglobin (dHb) can provide vascular  $pO_2$ <sup>8</sup>. However, vascular  $pO_2$  does not translate well to tissue  $pO_2$  because of the variable nature of perfusion and diffusion, especially in tumors, and the presence of myoglobin in some tissue<sup>5</sup>. The most clinically available method currently is pulse oximetry, which uses near-infrared range spectroscopy (NIRS) to measure the concentration of HbO<sub>2</sub> to total hemoglobin. It does have the major advantages of being inexpensive, real-time, and non-invasive.

Another technique that targets vascular oxygen is blood oxygen level-dependent (BOLD) MRI, where dHb acts as an endogenous contrast agent because of the paramagnetic electrons in Fe<sup>2+</sup><sup>8</sup>. Because BOLD contrast is only a function on the amount of deoxyhemoglobin, quantitative measurement of blood  $pO_2$  is very challenging, but BOLD MRI may provide valuable insight into changes in blood oxygen or volume and is clinically available and non-invasive<sup>5</sup>.

A more direct method for measuring tissue oxygenation uses <sup>19</sup>F-NMR probes. Molecular oxygen affects the NMR relaxation times of these probes. Therefore, biocompatible perfluorocarbons (PFOB, HFB, etc.) can be injected in vivo, and the relaxation times measured to derive the concentration of oxygen<sup>8</sup>. While MRI is readily available in most clinical settings, the use of <sup>19</sup>F-NMR spectroscopy and imaging is not yet available for clinical practice<sup>5</sup>. NMR-based methods are also limited by low resolution and very low sensitivity which is a major hurdle for exogenous perfluorocarbons probes<sup>28, 29</sup>.

Finally, electron paramagnetic resonance (EPR) oximetry operates on a similar principle as <sup>19</sup>F-NMR oximetry—molecular oxygen shortens the spin relaxation times of a paramagnetic probe. It results in a broadening of the EPR line of the probe. For soluble EPR probes, there is a linear relationship between the EPR linewidth of the probe and the oxygen concentration.<sup>8</sup> EPR oximetry is non-invasive and highly sensitive but does require the introduction of paramagnetic material or probes. Fortunately, the high sensitivity ( $\approx 1000$  times more sensitive than <sup>1</sup>H-NMR) allows for smaller amounts of spin probe than would be required for NMR. EPR oximetry is available for clinical use with particulate paramagnetic material, but clinical EPR instruments are not widely accessible today, and no soluble probes have been approved yet for use in humans<sup>5</sup>.

### 3.2 pH Measurement

One of the most common and oldest methods for measuring pH is with electrodes, and the glass electrode is generally used as the gold standard to calibrate and evaluate new methods<sup>30, 31</sup>. Most pH electrodes work by measuring the difference in potential across a membrane which depends on the concentration of  $H^+$  compared to a reference electrode. In general, pH electrodes have high sensitivity, accuracy, and pH response range between 2 and 9<sup>32</sup>. However, these electrodes are temperature-dependent and often suffer from stability issues and drift, requiring frequent calibrations<sup>32, 33</sup>. Microelectrodes have been made with various materials (glass, polymers, silicon, metal) in attempt to optimize biostability, biocompatibility, reliability, and accuracy for in vivo use<sup>32, 34</sup>. Still, these microelectrodes are limited to superficial readings and are invasive.

Optical-based methods are another common class of techniques for measuring pH in vivo. Generally, colorimetric or fluorescent pH indicator dyes are suspended in a solid matrix on an optical fiber-based sensor<sup>33</sup>. The optical fiber sensors can provide real-time blood or interstitial pH but can still experience drift from photobleaching<sup>33</sup>. These methods are also invasive, requiring implantation of the fiber into the area of interest. Therefore, the biocompatibility of the fiber, dye, and matrix is essential.

The first non-invasive method of measuring pH is with positron emission tomography (PET). Radiotracers will distribute between the extracellular and intracellular space depending on the pH and ion trapping of the cell membrane. Because the basis of the measurement is based on the affinity of the radio-labeled compound to cross the membrane, it can be imprecise and inaccurate.<sup>35</sup>

Magnetic Resonance Imaging (MRI) and spectroscopy (MRS) provide more valuable methods for measuring pH non-invasively. Specific gadolinium contrast agents have been developed with relaxivities modulated by the pH, providing pH-weighted MRI images<sup>36</sup>. Also, contrast agents for the chemical exchange saturation transfer (CEST) MRI modality have also been utilized for pH mapping in vivo<sup>20, 35</sup>. The major limitations to CEST-based MRI are that it requires relatively high concentrations (>10 mM) of contrast agent and a very stable magnetic field<sup>35</sup>. A clinically available way of measuring pH is by <sup>31</sup>P-NMR spectroscopy. The chemical shift between endogenous  $P_i$  and creatine phosphate on the MR spectrum can be used to calculate intracellular pH ( $pH_i$ )<sup>37</sup>. However, this method depends on the concentration of  $P_i$ , which is variable, lacks resolution, and is affected by ionic strength<sup>38, 39</sup>. In order to measure extracellular pH ( $pH_e$ ), a cell impermeable <sup>31</sup>P-NMR probe such as 3-aminopropylphosphonate (3-APP) needs to be injected<sup>40</sup>. 3-APP is highly biocompatible but has not been approved for use in humans<sup>40-42</sup>. More recently, 2-imidazole-1-yl-3-ethoxycarbonyl (IEPA) was developed as a pH-sensitive probe for <sup>1</sup>H-NMR<sup>35</sup>. The poor sensitivity of NMR techniques can be enhanced through dynamic nuclear polarization (DNP), which has been used to enhance the NMR signal of <sup>13</sup>C-labeled bicarbonate for pH measurement<sup>35</sup>. However, DNP suffers from the fast decay of hyperpolarization (in only a few minutes) and high instrumental, operation costs, and complexity of the technique.

EPR has an advantage over NMR by having a much larger analytical sensitivity and the absence of background signal. Similar to NMR, changes in pH caused shifts in peaks field positions and hyperfine splittings<sup>38</sup>. Early non-invasive EPR measurements of pH in vivo utilized pH-sensitive nitroxide radicals<sup>43, 44</sup>, but most nitroxides are quickly reduced in vivo to EPR-silent hydroxylamines<sup>45</sup>. Various trityl radicals, which have higher redox stability in vivo, have been shown to have an EPR spectrum sensitivity to both pH and oxygen<sup>38, 39, 46-48</sup>. Neither nitroxides nor trityl radicals are available for clinical use to date.

### 3.3 Phosphate measurement

Inorganic phosphate and phosphate-containing metabolites have been often measured in tumors using <sup>31</sup>P-NMR spectroscopy to differentiate from healthy tissue and to study growth mechanisms<sup>41, 49-51</sup>. The <sup>31</sup>P-NMR peaks are assigned to the different phosphates on NTP and NDP, phosphocreatine, phosphodiester, phosphomonoester, and inorganic phosphate, and the integrals of the peaks inform on the relative amount of each phosphorus-containing compound<sup>50, 51</sup>. However, this method using endogenous phosphorus does not allow for discrimination between extracellular and intracellular <sup>31</sup>P signals, and results in tumor tissue have been highly variable and unclear<sup>3</sup>.

In clinical practice,  $P_i$  is often measured in serum, plasma, blood, and urine samples using a colorimetric assay based on a complex between  $P_i$  and molybdate with a recording of the absorbance at 340 nm<sup>24</sup>. While phosphate is also generally elevated in the blood of patients with cancer<sup>23</sup>, it is not an accurate representation of the local  $[P_i]$  in the tumor. Microdialysis and colorimetric quantification of the extracellular  $[P_i]$  can be performed in pre-clinical settings, but this technique is invasive and difficult to implement<sup>52</sup>.

Within the past decade, a monophosphonated trityl radical EPR probe, pTAM, was developed for concurrent measurement of  $pO_2$  and  $pH_e$ , and it was also found to have spectral sensitivity to  $[P_i]$ <sup>48, 53, 54</sup>. With

increasing  $[P_i]$ , the proton exchange rate between the ionic species of pTAM increases and causes the EPR lines to coalesce<sup>48</sup>. The exchange rate can be calibrated against  $[P_i]$ <sup>3, 53, 54</sup>. Therefore, with pTAM and EPR spectroscopy, oxygen, pH, and  $[P_i]$  can be measured in vivo concurrently and non-invasively with high sensitivity<sup>3</sup>. Because all three parameters are derived from the same probe and not from multiple probes with different potential localization, pTAM allows for correlation analysis of these three parameters.

Table 1 summarizes the methods to measure  $pO_2$ , pH and  $[P_i]$  with their advantages and limitations.

Method	Advantages	Limitations	$pO_2$	pH	$[P_i]$	Concurrent
Microelectrode	- high accuracy - high sensitivity	- invasive - oxygen-consuming - frequent calibration	X	X		
Fiber-optic fluorescence	- high sensitivity	- invasive - photobleaching	X	X		
Fluorescence/phosphorescent imaging	- High resolution - non-invasive	- low penetration depth	X			
<sup>18</sup> F-FAZA PET (nitroimidazole)	- clinically available - non-invasive	- requires use of radioactive material	X			
NRIS	- inexpensive - real-time - non-invasive - clinically available	- blood fraction only	X			
BOLD-MRI	- non-invasive - clinically available	- not direct $pO_2$ measurement - blood fraction only	X			
<sup>19</sup> F-MRI	-- non-invasive	- low sensitivity	X			
pH-sensitive radiotracer PET	- clinically available - non-invasive	- imprecise - low accuracy		X		
CEST-MRI	- clinically available - non-invasive	- low sensitivity		X		
<sup>31</sup> P-MRI	- no exogenous compound required (except for $pH_e$ discrimination)	- low sensitivity - hard to discriminate between intracellular and extracellular $P_i$		X	X	X
Hyperpolarized <sup>13</sup> C-MRI	- non-invasive	- limited measurement time - high operational cost and complexity		X		
Colorimetric Assay with Molybdate	- clinically available	- blood or urine fraction			X	
EPR	- high sensitivity - non-invasive - extracellular specific	- low resolution	X	X	X	X

**Table 1.** Comparison of methods for in vivo measurement of the  $pO_2$ , pH, and  $[P_i]$ .

#### 4 EPR

Electron Paramagnetic Resonance (EPR) or Electron Spin Resonance (ESR) is based on the same principle as the most common nuclear magnetic resonance (NMR) technique, with a focus on the electron spins instead of the nuclear spins. Therefore, EPR applies to species with free electrons. A major difference between EPR and NMR is that the magnetic moment of the electron is 659 times greater than that of the proton, providing a much higher sensitivity<sup>8</sup>.

The most common EPR spectrometers operate at X-band (around 9.5 GHz) frequency. At this frequency, the non-resonant absorption of aqueous samples limits the penetration depth of the electromagnetic radiation to about 1 mm, insufficient for in vivo applications. Low-frequency EPR spectrometers (<1 GHz) allows for higher penetration depth but comes at a decrease in sensitivity.<sup>8</sup>

Another significant difference between NMR and EPR is the need for paramagnetic materials. With the exception of melanin, there are no endogenous species present in sufficient quantities to be detected directly by EPR *in vivo*. Therefore, *in vivo* applications of EPR require the injection of exogenous paramagnetic compounds or probes. In contrast, MRI detects the protons of endogenous water molecules which are present in large concentrations (>50M), allowing this method to thrive for *in vivo* applications despite its much lower sensitivity. The most popular application of *in vivo* EPR is EPR oximetry. While oxygen is paramagnetic with two unpaired electrons, its fast relaxation makes it undetectable in solution by EPR (the lines are too broad)<sup>8</sup>. However, the collisions between oxygen and a paramagnetic compound, introduced as probe, result in a shortening of the probe's relaxation times and a broadening of the EPR line (Figure 2) of the probe<sup>55</sup>. After calibration *in vitro*, the EPR linewidth of a probe measured *in vivo* reports the oxygen concentration in the vicinity of the probe.

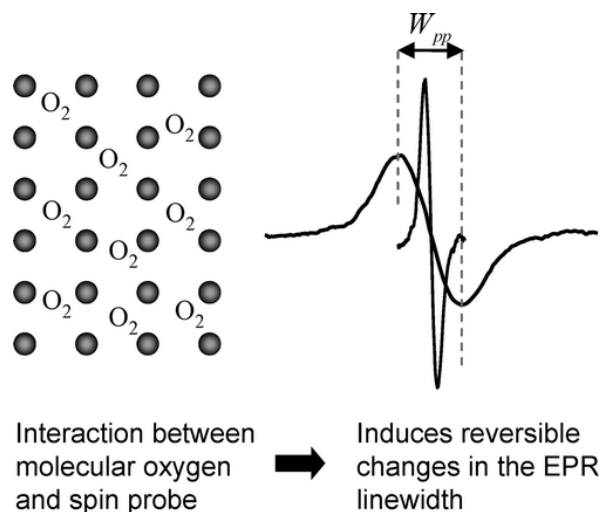


**Figure 2.** Effect of molecular oxygen on the EPR linewidth of a paramagnetic spin probe. Reproduced from Ahmad et. al.<sup>55</sup>.

#### 4.1 Paramagnetic Materials

There are two main categories of paramagnetic materials used for oxygen measurement, namely particulate and soluble probes.

Particulate paramagnetic substances, such as coals, chars, India ink, and lithium phthalocyanine, octa-n-butoxynaphthalocyanine (Figure 3A), have a high electron spin density and very high sensitivity to oxygen<sup>8, 55</sup>. They are also very stable and, once implanted *in vivo*, allow for repeated measurements at the same site over months. India ink and lithium octa-n-butoxynaphthalocyanine embedded in an FDA-approved biocompatible polymer (PDMS) are currently being used in clinics (Figure 3B)<sup>5</sup>. However, because of the variable nature of these materials, the EPR properties can vary between batches, and calibration of the oxygen sensitivity is required for each batch. Also, the high sensitivity of the probes to oxygen results in a significant loss in signal-to-noise ratio in normoxic conditions (as the intensity of the signal is inversely proportional to the square of the linewidth).<sup>8</sup>

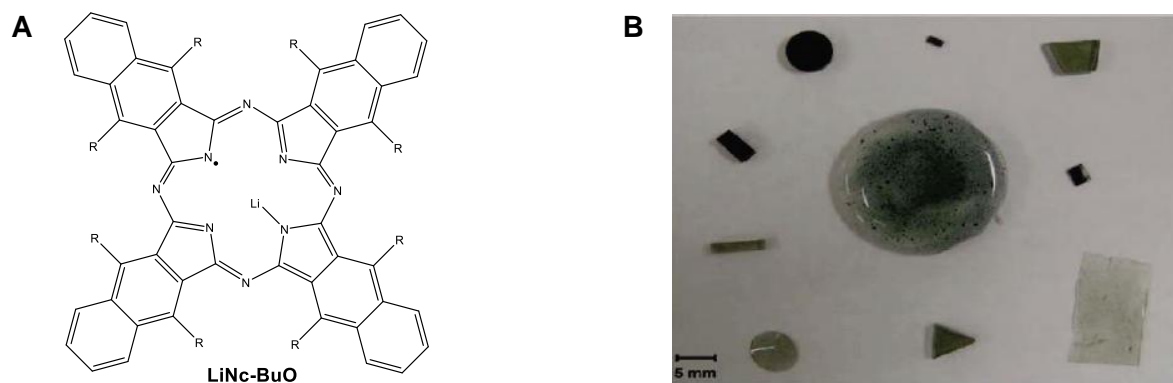


**Figure 3. A.** Structure of LiNc-BuO and **B.** LiNc-BuO emended into a gas permeable polymer. Reproduced from Ahmad et. al.<sup>55</sup>.

Soluble probes include nitroxides and trityl radicals (Figure 4). Nitroxides radicals have been first developed for EPR applications. The well-developed chemistry of nitroxides allowed for the synthesis of a large variety of structures with functional sensitivity to important parameters such as oxygen, pH, enzyme activity, redox status, or reactive oxygen species or with higher resistance to reduction. The main limitation of nitroxides is their fast bioreduction in vivo (a few seconds to a few minutes)<sup>45</sup>.

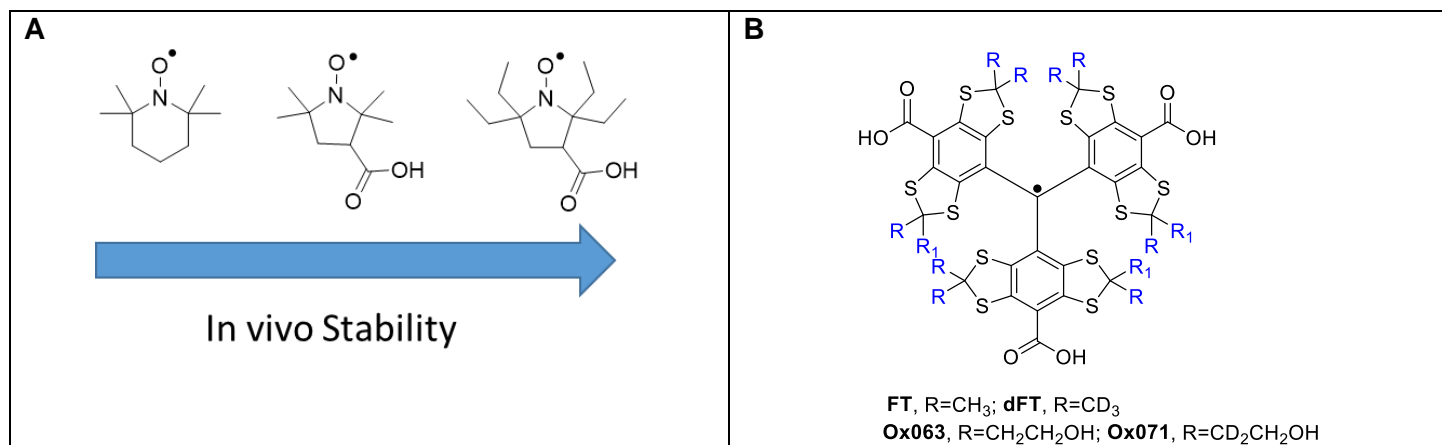


**Figure 4.** Structures of **A.** nitroxides and **B.** trityl radicals used for biomedical EPR.

On the other hand, triarylmethyl (TAM) or trityl radicals (Figure 4B) have extraordinary stability in vivo, with half-lives in blood in the range of hours to days and demonstrated resistance to most biological oxidoreductants<sup>56</sup>. Trityl radicals also have the advantages of longer relaxation time and narrower line widths, which allows for a higher signal-to-noise ratio, which is critical for in vivo application, and higher functional sensitivity<sup>8</sup>. The most popular structures are the Finland Trityl (FT), OX063, and their deuterated analogues dFT and OX071 (Figure 4B) developed in the late 90s by Nycomed Innovation (now subsidiary of GE Healthcare)<sup>57</sup>. Both structures exhibit extraordinary stability in biological media, high water solubility, and single-line EPR spectrum. Because of those features, trityl radicals are considered superior probes for biomedical EPR applications.

However, FTs and their derivatives have some major limitations for biological applications. Firstly, the lipophilic triarylmethyl core of the trityl is responsible for lipophilic interaction with biomacromolecules such as albumin<sup>58</sup>. This binding results in a broadening of the EPR line, which significantly reduces the signal intensity. FT and dFT both showed an 80% loss in signal intensity with equal molarity of trityl radical and bovine serum albumin<sup>58, 59</sup>. OX063 and OX071, on the other hand, are very hydrophilic with the addition of twelve hydroxyl groups, eliminating albumin binding and showing no loss in signal<sup>59</sup>. FTs and their derivatives are also toxic upon intravenous injection, with the doses required for spectroscopy being lethal, which prevent their systemic delivery<sup>60</sup>. However, in vivo measurements have been successfully made with small dose intratissue injections<sup>3</sup>. Again, OX063 and OX071 resolve this limitation with extremely low toxicity (LD<sub>50</sub>=8mmol/kg in mice) that is well above the required systemic dose for in vivo studies<sup>61-63</sup>. While the synthesis of FT was reported 20 years ago<sup>64</sup>, the synthesis of OX063/71 remained a trade secret for more than 25 years. For this reason, most of the synthetic efforts for the development of trityl radicals for biological EPR applications relied on the modification of the Finland trityl. Conjugating FT to dextran or polyethylene glycol (PEG) eliminated albumin binding but still lacked in biocompatibility and water solubility<sup>65</sup>. Replacing the carboxylates with sulfonates did significantly improve water solubility and reduced the affinity for albumin<sup>59</sup>. However, OX063/OX071 are still unmatched for their high aqueous solubility, low toxicity, and absence of interaction with blood biomacromolecules<sup>59, 61</sup>. Fortunately, our lab reported an efficient synthesis for OX063 and the deuterated OX071 in 2019<sup>66</sup>, making biocompatible trityl EPR probes more accessible for in vivo research and enabling the development of derivatives with enhanced functionality.

## 4.2 Trityl Derivatives

Over the last 20 years, several derivatives of trityl radicals have been developed with extended sensitivity to important parameters such as pH<sup>38, 46-48</sup>, redox status<sup>67</sup>, thiol concentration<sup>68</sup>, viscosity<sup>69</sup>, and inorganic phosphate concentration<sup>53</sup>. The concept of dual-function trityl  $pO_2$ /pH probes was introduced by the group of Dr. Khramtsov in 2007<sup>38</sup>. Since then, creative synthetic efforts and optimizations lead to a mono-phosphonated

triarylmethyl radical (pTAM or HOPE) as a multifunctional EPR probe to measure  $pO_2$ , pH, and  $[P_i]$  concurrently (Figure 5).

pTAM is a simplified doublet with good water solubility and a pH-sensitive shift in hyperfine splitting that is independent of the frequency<sup>48</sup>. This phosphonated trityl also showed a sensitivity to  $[P_i]$  because the rate of proton exchange is affected by the amount of phosphate, and when the exchange rate increases, the peaks of the two ionic states coalesce<sup>47, 48, 53</sup>. Importantly, pTAM has been used successfully to measure  $pO_2$ , pH, and  $[P_i]$  simultaneously in mouse models of breast cancer after intratissue injection<sup>3</sup>. This led to the identification of inorganic phosphate as a possibly powerful marker of tumors and metastatic character<sup>3</sup>. Also, the concurrent measurement allowed for true correlation analysis because it eliminates the temporal and location variances that would arise from using multiple methods or multiple probes. However, because pTAM is derived from FT, it has the biological limitations of binding to albumin and intravenous toxicity, which limits delivery to intratissue injection. Therefore, a major and clear improvement that can be made to the monophosphated trityl radical is better biocompatibility.

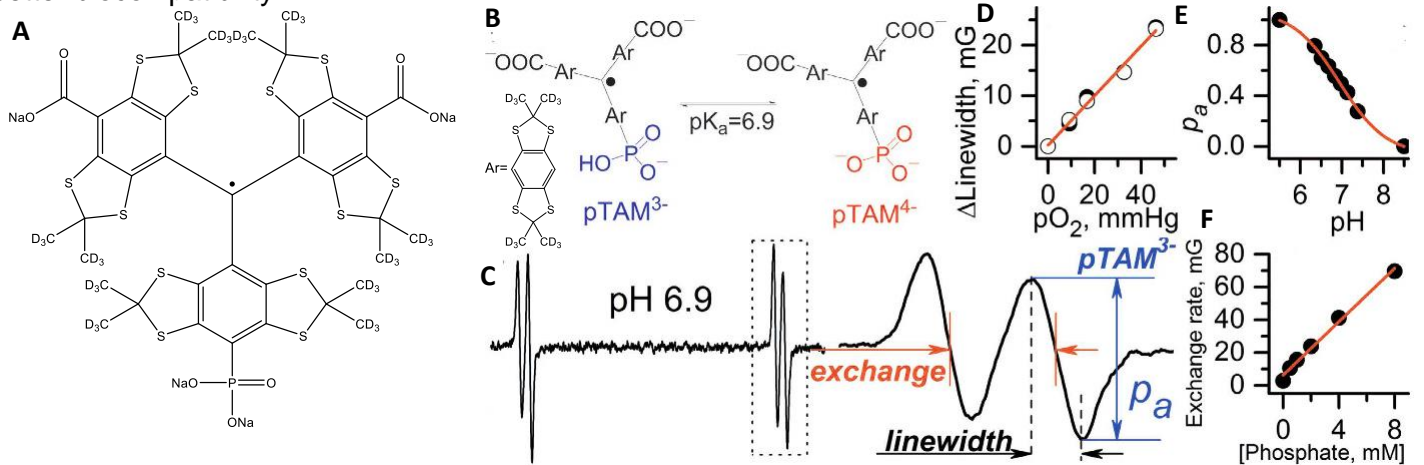


**Figure 5.** A. Structure of pTAM. B. Equilibrium of two ionic states of pTAM. C. Full EPR spectrum of pTAM and a zoom in on the high-field component with summary of effects of  $pO_2$ , pH, and  $[P_i]$  on spectral shape. D. Relationship between  $pO_2$  and EPR linewidth. E. Fraction of the acidic state ( $pTAM^{3-}$ ) against pH. F. The  $H^+$  exchange rate depends on the concentration of  $P_i$ . B-F Reproduced from Bobko et. al.<sup>3</sup>

## 5 Summary

Oxygenation ( $pO_2$ ), pH, and inorganic phosphate  $[P_i]$  are all important parameters of the tumor microenvironment that can inform on tumorigenesis, metastatic character, and therapeutic response. The ability to measure all three variables can help to better understand the tumor story, and simultaneous measurement with the same probe allows for deeper investigation with correlation analysis. EPR spectroscopy and imaging with the multifunctional probe, pTAM, provides a non-invasive way to concurrently measure  $pO_2$ , pH, and  $[P_i]$ . However, pTAM has major drawbacks in biological applications, and biocompatibility is a significant area for improvement.

## References

1. Torre, L. A.; Bray, F.; Siegel, R. L.; Ferlay, J.; Lortet-Tieulent, J.; Jemal, A., Global cancer statistics, 2012. *CA Cancer J Clin* **2015**, *65* (2), 87-108.
2. Arneth, B., Tumor Microenvironment. *Medicina (Kaunas)* **2019**, *56* (1).
3. Bobko, A. A.; Eubank, T. D.; Driesschaert, B.; Dhimitruka, I.; Evans, J.; Mohammad, R.; Tchekneva, E. E.; Dikov, M. M.; Khramtsov, V. V., Interstitial Inorganic Phosphate as a Tumor Microenvironment Marker for Tumor Progression. *Sci Rep* **2017**, *7*, 41233.
4. Carreau, A.; El Hafny-Rahbi, B.; Matejuk, A.; Grillon, C.; Kieda, C., Why is the partial oxygen pressure of human tissues a crucial parameter? Small molecules and hypoxia. *J Cell Mol Med* **2011**, *15* (6), 1239-53.
5. Swartz, H. M.; Flood, A. B.; Schaner, P. E.; Halpern, H.; Williams, B. B.; Pogue, B. W.; Gallez, B.; Vaupel, P., How best to interpret measures of levels of oxygen in tissues to make them effective clinical tools for care of patients with cancer and other oxygen-dependent pathologies. *Physiol Rep* **2020**, *8* (15), e14541.
6. McKeown, S. R., Defining normoxia, physoxia and hypoxia in tumours-implications for treatment response. *Br J Radiol* **2014**, *87* (1035), 20130676.

7. Thomlinson, R. H.; Gray, L. H., The histological structure of some human lung cancers and the possible implications for radiotherapy. *Br J Cancer* **1955**, 9 (4), 539-49.
8. Gallez, B.;Baudeflet, C.; Jordan, B. F., Assessment of tumor oxygenation by electron paramagnetic resonance: principles and applications. *NMR Biomed* **2004**, 17 (5), 240-62.
9. Harris, A. L., Hypoxia--a key regulatory factor in tumour growth. *Nat Rev Cancer* **2002**, 2 (1), 38-47.
10. Gatenby, R. A.; Gillies, R. J., Why do cancers have high aerobic glycolysis? *Nat Rev Cancer* **2004**, 4 (11), 891-9.
11. Michiels, C.;Tellier, C.; Feron, O., Cycling hypoxia: A key feature of the tumor microenvironment. *Biochim Biophys Acta* **2016**, 1866 (1), 76-86.
12. Whiteside, T. L., The tumor microenvironment and its role in promoting tumor growth. *Oncogene* **2008**, 27 (45), 5904-12.
13. Vito, A.;El-Sayes, N.; Mossman, K., Hypoxia-Driven Immune Escape in the Tumor Microenvironment. *Cells* **2020**, 9 (4).
14. Grimes, D. R., Estimation of the oxygen enhancement ratio for charged particle radiation. *Phys Med Biol* **2020**, 65 (15), 15NT01.
15. Richardson, R. B.; Harper, M. E., Mitochondrial stress controls the radiosensitivity of the oxygen effect: Implications for radiotherapy. *Oncotarget* **2016**, 7 (16), 21469-83.
16. Wenzl, T.; Wilkens, J. J., Modelling of the oxygen enhancement ratio for ion beam radiation therapy. *Phys Med Biol* **2011**, 56 (11), 3251-68.
17. Fellenz, M. P.; Gerweck, L. E., Influence of extracellular pH on intracellular pH and cell energy status: relationship to hyperthermic sensitivity. *Radiat Res* **1988**, 116 (2), 305-12.
18. Stubbs, M.;McSheehy, P. M. J.; Griffiths, J. R., Causes and consequences of acidic pH in tumors: a magnetic resonance study. *Advances in Enzyme Regulation: 1999; Vol. 39*, pp 13-30.
19. Justus, C. R.;Dong, L.; Yang, L. V., Acidic tumor microenvironment and pH-sensing G protein-coupled receptors. *Front Physiol* **2013**, 4, 354.
20. Chen, M.;Chen, C.;Shen, Z.;Zhang, X.;Chen, Y.;Lin, F.;Ma, X.;Zhuang, C.;Mao, Y.;Gan, H.;Chen, P.;Zong, X.; Wu, R., Extracellular pH is a biomarker enabling detection of breast cancer and liver cancer using CEST MRI. *Oncotarget* **2017**, 8 (28), 45759-45767.
21. Lunt, S. Y.; Vander Heiden, M. G., Aerobic glycolysis: meeting the metabolic requirements of cell proliferation. *Annu Rev Cell Dev Biol* **2011**, 27, 441-64.
22. Corbet, C.; Feron, O., Tumour acidosis: from the passenger to the driver's seat. *Nat Rev Cancer* **2017**, 17 (10), 577-593.
23. Papaloucas, C. D.;Papaloucas, M. D.;Kouloulias, V.;Neanidis, K.;Pistevou-Gompaki, K.;Kouvaris, J.;Zygogianni, A.;Mystakidou, K.; Papaloucas, A. C., Measurement of blood phosphorus: a quick and inexpensive method for detection of the existence of cancer in the body. Too good to be true, or forgotten knowledge of the past? *Med Hypotheses* **2014**, 82 (1), 24-5.
24. Iheagwara, O. S.;Ing, T. S.;Kjellstrand, C. M.; Lew, S. Q., Phosphorus, phosphorous, and phosphate. *Hemodial Int* **2013**, 17 (4), 479-82.
25. Lacerda-Abreu, M. A.;Russo-Abrahão, T.; Meyer-Fernandes, J. R., The Roles of Sodium-Independent Inorganic Phosphate Transporters in Inorganic Phosphate Homeostasis and in Cancer and Other Diseases. *Int J Mol Sci* **2020**, 21 (23).
26. Russo-Abrahão, T.;Lacerda-Abreu, M. A.;Gomes, T.;Cosentino-Gomes, D.;Carvalho-de-Araújo, A. D.;Rodrigues, M. F.;Oliveira, A. C. L.;Rumjanek, F. D.;Monteiro, R. Q.; Meyer-Fernandes, J. R., Characterization of inorganic phosphate transport in the triple-negative breast cancer cell line, MDA-MB-231. *PLoS One* **2018**, 13 (2), e0191270.
27. Melsens, E.;De Vlieghere, E.;Descamps, B.;Vanhove, C.;Kerseman, K.;De Vos, F.;Goethals, I.;Brans, B.;De Wever, O.;Ceelen, W.; Pattyn, P., Hypoxia imaging with. *Radiat Oncol* **2018**, 13 (1), 39.
28. Chapelin, F.;Capitini, C. M.; Ahrens, E. T., Fluorine-19 MRI for detection and quantification of immune cell therapy for cancer. *J Immunother Cancer* **2018**, 6 (1), 105.
29. Constantinides, C., Is There Preclinical and Clinical Value for. *Cell Transplant* **2020**, 29, 963689720954434.
30. Buck, R. P.;Rondinini, S.;Covington, A. K.;Baucke, F. G. K.;Brett, C. M. A.;Camoses, M. F.;Milton, M. J. T.;Mussini, M. J. T.;Naumann, R.;Pratt, K. W.;Spitzer, P.; Wilson, G. S., Measurement of pH. Definition, Standards, and Procedures. *International Union of Pure and Applied Chemistry: 2002; Vol. 74*, pp 2169-2200.
31. Pandolfino, J. E.;Ghosh, S.;Zhang, Q.;Heath, M.;Bombeck, T.; Kahrilas, P. J., Slimline vs. glass pH electrodes: what degree of accuracy should we expect? *Aliment Pharmacol Ther* **2006**, 23 (2), 331-40.

32. Zhou, D. D., Microelectrodes for in-vivo determination of pH. In *Electrochemical Sensors, Biosensors and Their Biomedical Applications*, Academic Press, Inc.: 2008; pp 261-305.
33. Wencel, D.;Kaworek, A.;Abel, T.;Efremov, V.;Bradford, A.;Carthy, D.;Coady, G.;McMorrow, R. C. N.; McDonagh, C., Optical Sensor for Real-Time pH Monitoring in Human Tissue. *Small* **2018**, *14* (51), e1803627.
34. Harsanyi, G., Chemical Sensors for Biomedical Applications. In *Biomedical Sensors*, Jones, D. P., Ed. Momentum Press: 2010; pp 323-384.
35. Zhang, X.;Lin, Y.; Gillies, R. J., Tumor pH and its measurement. *J Nucl Med* **2010**, *51* (8), 1167-70.
36. Aime, S.;Botta, M.;Crich, S. G.;Giovenzana, G.;Palmisano, G.; Sisti, M., A macromolecular Gd(III) complex as pH-responsive relaxometric probe for MRI applications. *Chemical Communications*: 1999; pp 1577-1578.
37. van den Thillart, G.;van Waarde, A.;Muller, H. J.;Erkelens, C.;Addink, A.; Lugtenburg, J., Fish muscle energy metabolism measured by in vivo <sup>31</sup>P-NMR during anoxia and recovery. *Am J Physiol* **1989**, *256* (4 Pt 2), R922-9.
38. Bobko, A. A.;Dhimitruka, I.;Zweier, J. L.; Khramtsov, V. V., Trityl radicals as persistent dual function pH and oxygen probes for in vivo electron paramagnetic resonance spectroscopy and imaging: concept and experiment. *J Am Chem Soc* **2007**, *129* (23), 7240-1.
39. Dhimitruka, I.;Bobko, A. A.;Hadad, C. M.;Zweier, J. L.; Khramtsov, V. V., Synthesis and characterization of amino derivatives of persistent trityl radicals as dual function pH and oxygen paramagnetic probes. *J Am Chem Soc* **2008**, *130* (32), 10780-7.
40. Gillies, R. J.;Liu, Z.; Bhujwalla, Z., <sup>31</sup>P-MRS measurements of extracellular pH of tumors using 3-aminopropylphosphonate. *Am J Physiol* **1994**, *267* (1 Pt 1), C195-203.
41. Lora-Michiels, M.;Yu, D.;Sanders, L.;Poulson, J. M.;Azuma, C.;Case, B.;Vujaskovic, Z.;Thrall, D. E.;Charles, H. C.; Dewhirst, M. W., Extracellular pH and P-31 magnetic resonance spectroscopic variables are related to outcome in canine soft tissue sarcomas treated with thermoradiotherapy. *Clin Cancer Res* **2006**, *12* (19), 5733-40.
42. Lutz, N. W.;Le Fur, Y.;Chiche, J.;Pouysségur, J.; Cozzone, P. J., Quantitative in vivo characterization of intracellular and extracellular pH profiles in heterogeneous tumors: a novel method enabling multiparametric pH analysis. *Cancer Res* **2013**, *73* (15), 4616-28.
43. Foster, M. A.;Grigor'ev, I. A.;Lurie, D. J.;Khramtsov, V. V.;McCallum, S.;Panagiotelis, I.;Hutchison, J. M.;Koptioug, A.; Nicholson, I., In vivo detection of a pH-sensitive nitroxide in the rat stomach by low-field ESR-based techniques. *Magn Reson Med* **2003**, *49* (3), 558-67.
44. Potapenko, D. I.;Foster, M. A.;Lurie, D. J.;Kirilyuk, I. A.;Hutchison, J. M.;Grigor'ev, I. A.;Bagryanskaya, E. G.; Khramtsov, V. V., Real-time monitoring of drug-induced changes in the stomach acidity of living rats using improved pH-sensitive nitroxides and low-field EPR techniques. *J Magn Reson* **2006**, *182* (1), 1-11.
45. Jagtap, A. P.;Krstic, I.;Kunjir, N. C.;Hänsel, R.;Prisner, T. F.; Sigurdsson, S. T., Sterically shielded spin labels for in-cell EPR spectroscopy: analysis of stability in reducing environment. *Free Radic Res* **2015**, *49* (1), 78-85.
46. Bobko, A. A.;Dhimitruka, I.;Komarov, D. A.; Khramtsov, V. V., Dual-function pH and oxygen phosphonated trityl probe. *Anal Chem* **2012**, *84* (14), 6054-60.
47. Driesschaert, B.;Marchand, V.;Levêque, P.;Gallez, B.; Marchand-Brynaert, J., A phosphonated triarylmethyl radical as a probe for measurement of pH by EPR. *Chem Commun (Camb)* **2012**, *48* (34), 4049-51.
48. Dhimitruka, I.;Bobko, A. A.;Eubank, T. D.;Komarov, D. A.; Khramtsov, V. V., Phosphonated trityl probes for concurrent in vivo tissue oxygen and pH monitoring using electron paramagnetic resonance-based techniques. *J Am Chem Soc* **2013**, *135* (15), 5904-10.
49. Rofstad, E. K.;DeMuth, P.; Sutherland, R. M., <sup>31</sup>P NMR spectroscopy measurements of human ovarian carcinoma xenografts: Relationship to tumour volume, growth rate, necrotic fraction and differentiation status. *Radiotherapy and Oncology*: 1988; Vol. 12, pp 315-326.
50. Stubbs, M.;Rodrigues, L. M.; Griffiths, J. R., Growth studies of subcutaneous rat tumours: comparison of <sup>31</sup>P-NMR spectroscopy, acid extracts and histology. *Br J Cancer* **1989**, *60* (5), 701-7.
51. Dewhirst, M. W.;Sostman, H. D.;Leopold, K. A.;Charles, H. C.;Moore, D.;Burn, R. A.;Tucker, J. A.;Harrelson, J. M.; Oleson, J. R., Soft-tissue sarcomas: MR imaging and MR spectroscopy for prognosis and therapy monitoring. Work in progress. *Radiology* **1990**, *174* (3 Pt 1), 847-53.
52. Scheller, D.;Kolb, J.;Peters, U.; Tegtmeier, F., The measurement of extracellular inorganic phosphate gives a more reliable indication for severe impairment of cerebral cell function and cell death than the measurement of extracellular lactate. *Acta Neurochir Suppl* **1996**, *67*, 28-30.

53. Bobko, A. A.; Dhimitruka, I.; Zweier, J. L.; Khramtsov, V. V., Fourier transform EPR spectroscopy of trityl radicals for multifunctional assessment of chemical microenvironment. *Angew Chem Int Ed Engl* **2014**, *53* (10), 2735-8.
54. Bobko, A. A., Chemical exchange induced Hahn echo modulation in pulsed electron paramagnetic resonance experiment. *J Magn Reson* **2020**, *315*, 106742.
55. Ahmad, R.; Kuppusamy, P., Theory, instrumentation, and applications of electron paramagnetic resonance oximetry. *Chem Rev* **2010**, *110* (5), 3212-36.
56. Liu, Y.; Villamena, F. A.; Zweier, J. L., Highly stable dendritic trityl radicals as oxygen and pH probe. *Chem Commun (Camb)* **2008**, (36), 4336-8.
57. Anderson, S.; Radner, F.; Rydbeck, A.; Servin, R.; Wistrand, L.-G. Free Radicals. 5530140, 1996.
58. Song, Y.; Liu, Y.; Liu, W.; Villamena, F. A.; Zweier, J. L., Characterization of the Binding of the Finland Trityl Radical with Bovine Serum Albumin. *RSC Adv* **2014**, *4* (88), 47649-47656.
59. Sanzhaeva, U.; Poncelet, M.; Tseytlin, O.; Tseytlin, M.; Gencheva, M.; Eubank, T. D.; Khramtsov, V. V.; Driesschaert, B., Synthesis, Characterization, and Application of a Highly Hydrophilic Triarylmethyl Radical for Biomedical EPR. *J Org Chem* **2020**, *85* (16), 10388-10398.
60. Lampp, L.; Rogozhnikova, O. Y.; Trukhin, D. V.; Tormyshev, V. M.; Bowman, M. K.; Devasahayam, N.; Krishna, M. C.; Mäder, K.; Imming, P., A radical containing injectable in-situ-oleogel and emulgel for prolonged in-vivo oxygen measurements with CW EPR. *Free Radic Biol Med* **2019**, *130*, 120-127.
61. Krishna, M. C.; English, S.; Yamada, K.; Yoo, J.; Murugesan, R.; Devasahayam, N.; Cook, J. A.; Golman, K.; Ardenkjaer-Larsen, J. H.; Subramanian, S.; Mitchell, J. B., Overhauser enhanced magnetic resonance imaging for tumor oximetry: coregistration of tumor anatomy and tissue oxygen concentration. *Proc Natl Acad Sci U S A* **2002**, *99* (4), 2216-21.
62. Epel, B.; Sundramoorthy, S. V.; Barth, E. D.; Mailer, C.; Halpern, H. J., Comparison of 250 MHz electron spin echo and continuous wave oxygen EPR imaging methods for in vivo applications. *Med Phys* **2011**, *38* (4), 2045-52.
63. Serda, M.; Wu, Y. K.; Barth, E. D.; Halpern, H. J.; Rawal, V. H., EPR Imaging Spin Probe Trityl Radical OX063: A Method for Its Isolation from Animal Effluent, Redox Chemistry of Its Quinone Methide Oxidation Product, and in Vivo Application in a Mouse. *Chem Res Toxicol* **2016**, *29* (12), 2153-2156.
64. Reddy, T. J.; Iwama, T.; Halpern, H. J.; Rawal, V. H., General synthesis of persistent trityl radicals for EPR imaging of biological systems. *J Org Chem* **2002**, *67* (14), 4635-9.
65. Poncelet, M.; Driesschaert, B.; Tseytlin, O.; Tseytlin, M.; Eubank, T. D.; Khramtsov, V. V., Dextran-conjugated tetrathiatriarylmethyl radicals as biocompatible spin probes for EPR spectroscopy and imaging. *Bioorg Med Chem Lett* **2019**, *29* (14), 1756-1760.
66. Poncelet, M.; Huffman, J. L.; Khramtsov, V. V.; Dhimitruka, I.; Driesschaert, B., Synthesis of hydroxyethyl tetrathiatriarylmethyl radicals OX063 and OX071. *RSC Adv* **2019**, *9* (60), 35073-35076.
67. Tan, X.; Song, Y.; Liu, H.; Zhong, Q.; Rockenbauer, A.; Villamena, F. A.; Zweier, J. L.; Liu, Y., Supramolecular host-guest interaction of trityl-nitroxide biradicals with cyclodextrins: modulation of spin-spin interaction and redox sensitivity. *Org Biomol Chem* **2016**, *14* (5), 1694-701.
68. Liu, Y.; Song, Y.; Rockenbauer, A.; Sun, J.; Hemann, C.; Villamena, F. A.; Zweier, J. L., Synthesis of trityl radical-conjugated disulfide biradicals for measurement of thiol concentration. *J Org Chem* **2011**, *76* (10), 3853-60.
69. Poncelet, M.; Driesschaert, B., A <sup>13</sup>C-Labeled Triarylmethyl Radical as an EPR Spin Probe Highly Sensitive to Molecular Tumbling. *Angew Chem Int Ed Engl* **2020**, *59* (38), 16451-16454.

## **CHAPTER 2 – Biocompatible Monophosphonated Trityl Spin Probe, HOPE71, for In Vivo Measurement of $pO_2$ , pH, and $[P_i]$ in Mouse Tumors by Electron Paramagnetic Resonance Spectroscopy**

Contribution: I am the primary contributor to this paper and performed all experiments. Acknowledgment goes to Martin Poncelet for synthesis of OX071, E. Hannah Hoblitzell for breeding and genotyping the mice, and Benoit Driesschaert for idea conception and advisement.

### **Biocompatible Monophosphonated Trityl Spin Probe, HOPE71, for In Vivo Measurement of $pO_2$ , pH, and $[P_i]$ in Mouse Tumors by Electron Paramagnetic Resonance Spectroscopy**

Teresa D. Gluth<sup>1,2</sup>, Martin Poncelet<sup>1,2</sup>, Marieta Gencheva<sup>2,3</sup>, E. Hannah Hoblitzell<sup>2,3</sup>, Valery V. Khrantsov<sup>2,3</sup>, Timothy D. Eubank<sup>2,4</sup> and Benoit Driesschaert<sup>1,2,\*</sup>

<sup>1</sup>Department of Pharmaceutical Sciences, West Virginia University, School of Pharmacy, Morgantown, WV, 26506, USA.

<sup>2</sup>In Vivo Multifunctional Magnetic Resonance center, Robert C. Byrd Health Sciences Center, West Virginia University, Morgantown, WV, 26506, USA.

<sup>3</sup>Department of Biochemistry, West Virginia University, School of Medicine, Morgantown, WV, 26506, USA.

<sup>4</sup>Department of Microbiology, Immunology, and Cell Biology, West Virginia University, School of Medicine, Morgantown, WV, 26506, USA.

#### **ABSTRACT**

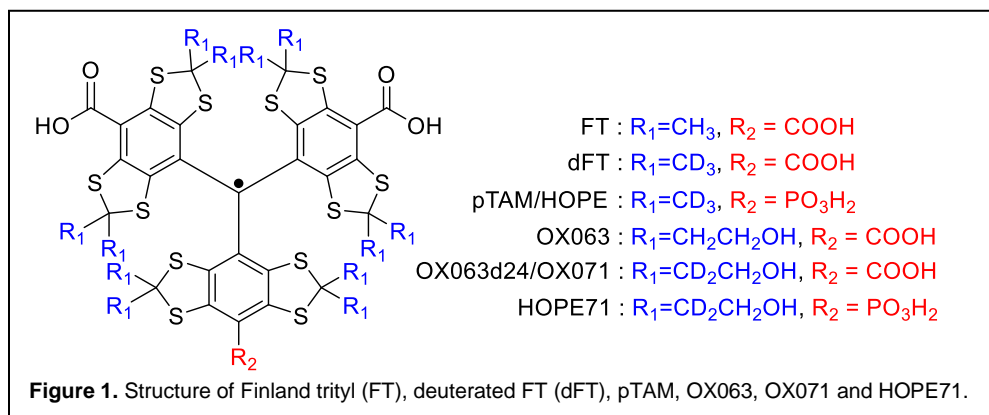
Hypoxia, acidosis, and elevated inorganic phosphate concentration are characteristic of the tumor microenvironment in solid tumors. There are a number of methods for measuring each parameter individually in vivo, but the only method to date for non-invasive measurement of all three variable simultaneously in vivo is electron paramagnetic spectroscopy paired with a monophosphonated trityl radical, pTAM. While pTAM has been successfully used for in vivo studies upon intratissue injection, it cannot be delivered intravenously due to systemic toxicity and albumin binding, which causes significant signal loss. Therefore, we present HOPE71, a monophosphonated trityl radical derived from the very biocompatible trityl probe, OX071. Here we present a straightforward synthesis of HOPE71 starting with OX071, and report its EPR sensitivities to  $pO_2$ , pH, and  $[P_i]$  with X-band and L-band EPR spectroscopy. We also confirm that HOPE71 lacks albumin binding, shows low cytotoxicity, and has systemic tolerance. Finally, we demonstrate its ability to profile tumors in vivo with a longitudinal tumor growth study.

## Introduction

In recent years, the tumor microenvironment (TME) has gained focus in cancer research because it can hold key information about tumorigenesis, immune escape, and therapeutic response. Several key physiological parameters of the TME that are of interest include tissue oxygenation ( $pO_2$ ), extracellular pH ( $pH_e$ ), and interstitial inorganic phosphate concentration [ $P_i$ ]. Hypoxia ( $pO_2 < 10$  mmHg) and acidosis ( $pH_e < 7$ ) have been recognized as hallmarks of solid tumors for quite some time, and elevated [ $P_i$ ] was more recently identified as a biomarker of the TME<sup>1</sup>. Hypoxia occurs in tumors because of increased oxygen consumption along with decreased oxygen delivery. Cancer cells demand higher amounts of oxygen to support their fast metabolism and proliferation rates<sup>2</sup>. Furthermore, irregular tumor vasculature fails to deliver sufficient oxygen because of increased distance between cells and blood vessels (diffusion-limited) and temporary drops in blood flow (perfusion-limited)<sup>3</sup>. Hypoxia can lead to aggressive disease with more metastatic character<sup>4-6</sup> and pathways for immune escape<sup>7, 8</sup>. Tumor hypoxia is also associated with therapeutic resistance, especially in radiation therapy. The presence of oxygen improves radiosensitivity, as described by the oxygen enhancement effect, and, as a result, hypoxic cells require up to three times the therapeutic radiation dose as normoxic cells<sup>9, 10</sup>. Cancer cells also demonstrate a high rate of glycolysis, even in well-oxygenated conditions, which leads to high amounts of lactate and protons being excreted from the cells, which may not be efficiently removed by tumor vasculature<sup>5, 11, 12</sup>. Acidosis has also been linked to more aggressive disease and metastatic potential<sup>5</sup>, and acidic extracellular pH may also affect the absorption and effectiveness of chemotherapy drugs. Finally, inorganic phosphate may be elevated in the TME due to high growth rate demands for nucleotides, phospholipids, and cell-signaling<sup>13</sup>. Also, phosphate concentration demonstrated the ability to discriminate between metastatic and non-metastatic disease<sup>1</sup>.

Therefore, measurement of  $pO_2$ ,  $pH_e$ , and [ $P_i$ ] is crucial for better understanding tumorigenesis, aggressive disease mechanisms, and therapy resistance. They also have the potential to play a role in optimizing therapy strategies clinically. There are various methods for measuring each parameter individually, and they all have their benefits and limitations, with the most notable drawbacks being invasiveness and low sensitivity. To our knowledge, Electron Paramagnetic Resonance (EPR) Spectroscopy with a monophosphonated trityl probe, pTAM (Fig. 1), is the only method for non-invasive measurement of all three parameters concurrently. The EPR spectrum of pTAM is a doublet with a linewidth sensitive to oxygen and hyperfine splitting is sensitive to pH. The signal is also sensitive to [ $P_i$ ] because the concentration of phosphate buffer affects the proton exchange rate on pTAM, which causes the different ionic species peaks to coalesce<sup>4, 14, 15</sup>. However, pTAM is a derivative of deuterated Finland trityl (dFT, Fig. 1), which has major limitations for biological applications. FTs bind to albumin which drastically reduces the signal intensity and may increase the line width<sup>16, 17</sup>. FTs are also toxic upon intravenous injection<sup>18</sup>, which limits in vivo work to intratissue delivery.

Alternatively, OX063 and the deuterated OX071 (Fig. 1), trityl probes with twelve hydroxyethyl groups, are very hydrophilic and does not bind to albumin<sup>17</sup>. They also have a remarkably low toxicity ( $LD_{50} = 8$  mmol/kg) in mice and has been used broadly for in vivo OMRI and EPR oximetry studies<sup>19-22</sup>. Therefore, we propose HOPE71 (Fig. 1), a monophosphonated derivative of OX071 as a more biocompatible multifunctional trityl probe for concurrent EPR measurement of  $pO_2$ ,  $pH_e$ , and [ $P_i$ ]. First, we report a straightforward synthesis of HOPE71 with a 2-step process starting from OX071. Then, we characterize the EPR sensitivities to  $pO_2$ ,  $pH_e$ , and [ $P_i$ ] with X-band and L-band spectroscopy. Next, we present biocompatibility improvements by showing the difference in albumin binding, performing cell viability assays, and testing intravenous tolerance in mice. Finally, we demonstrate the ability of HOPE71 to profile mammary gland tumors in mice models and report a longitudinal study indicating that TME pH increasing deviates from healthy tissue with tumor growth.



## Materials and Methods

### General

All reactions were carried out under argon in flame-dried glassware using anhydrous grade solvents, except for the phosphorylation of OX071 (1<sup>st</sup> step), which was performed in an aerated aqueous solution. All commercially available reagents were purchased from Sigma-Aldrich or Fisher Scientific and used as received without further purification. OX071 was synthesized according to a published protocol<sup>23</sup>. X-Band and L-Band EPR spectra were recorded using a Bruker Elexsys E580 (9.5 GHz) and a Magnettech (1.2 GHz) spectrometers, respectively. For X-band spectra, 50  $\mu$ L of the solution was filled into a gas-permeable Teflon tube (1.14 mm diameter and 60  $\mu$ m wall thickness) from Zeus, Inc. and the temperature and the nitrogen/oxygen gas mixture were controlled inside the resonator using a Noxygen temperature and gas controller. Gas was flushed for at least 10 min before the measurement or until the spectrum becomes time independent. For L-Band spectra, 800  $\mu$ L of the solution was filled into a 1.5 mL conical tube. The temperature was controlled using a circulation thermostat. Nitrogen/oxygen gas mixture from the gas controller was bubbled into the solution for 25-30 min before the measurement. HRMS spectra were recorded on a ThermoFisher Scientific Q Exactive Mass Spectrometer with an Electron Spray Ionization (ESI) source. HPLC-MS analyses were carried out using a Water Alliance e2695 separation module, a Water 2998 PDA detector, and a Water SQD2 mass detector. Purifications on C18 column were carried out using a CombiFlash Rf+ purification system using water (containing 0.1% TFA) and acetonitrile (containing 0.1% TFA). Freeze drying was carried out using a MartinChrist Alpha 2-4 LSCbasic. A Thermo Scientific Orion Star A111 Benchtop pH meter with a Fisherbrand Accumet Micro Glass Combination Electrode was used and was calibrated with 4.00 and 9.00 buffer solutions from Fisher Chemical before the experiments.

### Synthesis

**Step 1: Monophosphorylation of OX071.** The starting material, OX071 tri-sodium salt (959 mg, 0.661 mmol, 1 eq.), was dissolved to a concentration of 1 mM in Na-phosphate buffer (10 mM, pH=7.4, 660 mL). Then, a solution of potassium hexachloroiridate(IV),  $K_2IrCl_6$ , (940 mg, 1.946 mmol, 3 eq.) in deionized water (70 mL) was added to generate the triarylmethyl cation; the green solution turned deep green-blue. The reaction was stirred 10 seconds, and triethyl phosphite,  $P(OEt)_3$ , (2.195 g, 13.210 mmol, 2.27 mL, 20 eq.) was added. The reaction mixture was stirred for 10 minutes, and the conversion checked by HPLC-MS. The mixture was acidified to pH  $\leq$  2 using trifluoroacetic acid and loaded into a C18 loading cartridge (25 g). The crude product was purified by reverse-phase chromatography using a C18 column (86 g) with a gradient of acidic water/acetonitrile (95/5 to 85/15) and freeze-dried. 138 mg of **2** was recovered as a green solid (14% yield). 431 mg (47%) of OX071 was also recovered.

**Step 2: Deprotection of the phosphonic acid.** Diethyl phosphonate HOPE71 **2** (138 mg, 0.094 mmol, 1 eq.) was dissolved in anhydrous dimethylformamide (15 mL) under argon. The solution was cooled to 0°C, and bromotrimethylsilane, TMSBr, in excess (1mL) was slowly added. After stirring for 10 minutes at 0°C, the reaction was heated at 50°C for 5 hours, and the deprotection was monitored by HPLC-MS. The TMSBr was removed under reduced pressure. Methanol (10 mL) was added, stirred 1 min, and removed under reduced pressure. The DMF solution was diluted 20 times with deionized water and freeze-dried. The final product was purified using a C18 column (26 g) with a gradient from acidic water to acidic water/acetonitrile (80/20) and freeze-dried. The residue was dissolved in water and titrated to pH=7 with NaOH (0.1M) and freeze-dried again to afford 121 mg (88%) of HOPE71 as a green powder.

### Spectral sensitivity to oxygen, pH, and inorganic phosphate.

**X-band Acquisition parameters.** For each condition, a focus on the low-field part of the spectrum was recorded six times. For certain conditions (identified below), a full spectrum was recorded three times. Settings were as follows: power; 0.04743 mW, mod. freq.; 30 kHz, mod. Ampl.; 50 mG, conv. time; 30.01 ms, number of points; 2054 for the full spectrum and 1024 for the low-field spectrum, sweep width; 6.0 G for the full spectrum and 2.0 G for the low-field spectrum. All spectra were measured at 37°C.

**L-band Acquisition parameters.** For each condition, a focus on the low-field part of the spectrum was recorded four times. Parameter settings for the spectrometer were as follows: mod. freq.; 100 kHz, mod. Ampl.; 0.005 mT,

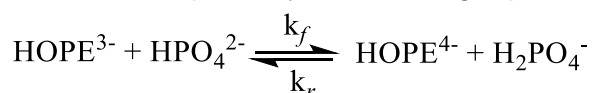
scan time; 30s, number of points; 4096, sweep width; 0.0960 mT and non-saturating power. All spectra were measured at 37°C.

**Spectral fitting.** A MATLAB-based application developed in house with graphical user interface for a non-linear fitting function (Isqcurvefit) was used to fit each EPR spectrum<sup>24</sup>(Fig. S2). Fitting was performed on the low-field focused spectra. The following values were determined as constants for the spectral modelling: Gaussian linewidth, individual intrinsic Lorentzian linewidth of the acidic and basic peaks, and the distant between the acidic and basic peaks. The Gaussian linewidth and intrinsic Lorentzian linewidths were determined by sextuplicate EPR spectra measured with no oxygen, and with acidic (pH < 5) or basic (pH > 10) conditions so that only the acid or basic peak was present. The acidic to basic peak distance was determined by sextuplicate EPR spectra measured with no oxygen and no phosphate buffer at pH≈7. The variable parameters that also contributed to or were dependent on the curve-fitting include oxygen-induced Lorentzian linewidth broadening, proton exchange rate, and acidic fraction of the population.

**X-band Oxygen calibration.** To determine the linewidth sensitivity to oxygen for both ionic forms. 200 μM solutions of HOPE71 in 1 mM phosphate buffer and 137 mM NaCl at pH=4.8 and 10 were prepared, and spectra were recorded for  $pO_2 = 0$  mmHg, 19 mmHg, 38 mmHg, 76 mmHg, 114 mmHg, and 159 mmHg. Full spectra were recorded for both pH=4.8 and pH=10 with  $pO_2 = 0$  mmHg. The spectral fitting described above was used to determine the oxygen-induced line broadening for each  $pO_2$ . Linear fit using OriginLab allow for determination of the oxygen sensitivity for both ionic forms combined.

**X-band pH calibration.** To determine the pKa of the probe, a 200 μM solution of HOPE71 1 mM phosphate buffer and 137 mM NaCl was titrated by addition of small amounts of HCl and NaOH. For each titrated pH, spectra were recorded with  $pO_2 = 0$  mmHg. Full spectra were recorded of pH=7.1. The spectral fitting described above was used to determine the acidic fraction at each measured pH. A plot of pH versus acidic fraction ( $P_a$ ) was fitted to the equation  $P_a = \frac{1}{1+10^{pH-pKa}}$  using OriginLab to determine the pKa.

**X-band Inorganic phosphate calibration.** To determine the exchange rate dependence to phosphate concentration, 200 μM solutions of HOPE71 at pH=7.2 and  $pO_2 = 0$  mmHg. were recorded for phosphate concentration of 0 mM, 1 mM, 4 mM, 7 mM, and 10 mM. The spectral fitting described above was used to determine the exchange rate for each phosphate concentration. The proton exchange between phosphate and HOPE71 is express by the following equation:



The rate of proton loss of HOPE<sup>3-</sup> to HPO<sub>4</sub><sup>2-</sup> is  $k_a = k_f [HPO_4^{2-}]$ . The rate constant  $k_f$  can be determine by linear approximation of the dependence of  $k_a$  on  $[HPO_4^{2-}]$  or the total phosphate concentration  $[P_i]$  using  $[HPO_4^{2-}] = [P_i] (H^+ + K_a^B)/(2\pi K_a^B)$ . Where  $K_a^B$  is the dissociation constant of phosphate buffer ( $K_a^B=10^{-6.66}$ )<sup>25</sup>. Linear fit of the equation  $\frac{k_a(H^+ + K_a^B)}{2\pi K_a^B} = k_f [P_i]$ , using OriginLab allows determination of the phosphate sensitivity.

**Validation of the calibration with blind sample. (X-band).** Three solutions with 200 μM of HOPE71 and 137 mM NaCl were prepared with various concentrations of inorganic phosphate (1-10 mM), pH and  $pO_2$  that were that were blinded to the researcher acquiring the spectra. The spectral fitting described above was used to extract the oxygen-induced Lorentzian linewidth broadening, proton exchange rate, and acidic fraction. The calibrations above were used to determine the EPR measured  $pO_2$ , pH, and  $[P_i]$ .

**L-band calibrations and validation.** The  $pO_2$ , pH, and  $[P_i]$  calibrations and validation were repeated for L-band EPR with 500 μM solution of HOPE71. Oxygen calibration spectra were recorded for  $pO_2 = 0$  mmHg, 17 mmHg, 34 mmHg, 68 mmHg, 103 mmHg, and 159 mmHg. Phosphate calibration spectra were recorded on solutions with 0 mM, 1 mM, 4 mM, 7 mM, and 10 mM of inorganic phosphate.

## **Biological Application Characterizations.**

**Albumin binding.** To study the interaction of HOPE71 with albumin, 200  $\mu\text{M}$  solutions of HOPE71 at pH=7 were prepared, one with no bovine serum albumin (BSA) as control and one with 200  $\mu\text{M}$  BSA (1 equiv.). For comparison, 200  $\mu\text{M}$  solutions of pTAM at pH=7 were also prepared with 0  $\mu\text{M}$ , 50  $\mu\text{M}$ , 100  $\mu\text{M}$ , and 200  $\mu\text{M}$  BSA. Spectra were recorded for each solution with X-band EPR. Spectra of pTAM were acquired with mod. Ampl. = 25 mG.

**MTT assay for cell toxicity.** MDA-MB-231 (triple-negative breast cancer) cells were plated on a 96-well flat-bottom plate and allowed to grow over night to 60-70% confluency. The medium used was DMEM with 10% fetal bovine serum. The cells were then incubated with increasing concentrations of pTAM or HOPE71 in medium for 24 hours. DMSO (2% and 5% in medium) was used as a cytotoxic control. Medium with corresponding concentrations of pTAM or HOPE71 were used as a background control. All conditions were performed in quadruplicate. The MTT assay was performed using ThermoFisher Vybrant MTT Cell Proliferation Assay Kit according to the manufacturer's protocol. Absorbance was measured at 570 nm minus 630 nm to correct for cell debris. Statistically analysis was performed using one-way ANOVA. This process was repeated with HUVECs (Human umbilical vein endothelial cells) using vascular cell basal medium plus ATCC Endothelial Cell Growth Kit-VEGF.

## **In vivo Applications.**

**Mouse model.** Female MMTV-PyMT (PyMT+/-) mice with spontaneous mammary tumors and their wildtype littermates (PyMT-/-), 10-15 weeks in age, were used for HOPE71 in vivo EPR studies. Mice were anesthetized by inhalation of isoflurane in air prior to injection and during acquisition of spectra.

**In vivo L-band Acquisition parameters.** For each in vivo EPR measurement of HOPE71, the resonator coil was placed on mammary gland 4 (MG4) or 9 (MG9). Focus on the low-field part of the spectrum was recorded six times. Parameter settings for the spectrometer were as follows: mod. freq.; 100 kHz, mod. Ampl.; 0.005 mT, scan time; 30s or 60s, number of points; 4096, sweep width; 0.0960 mT and non-saturating power.

**Intravenous Tumor Profiling.** Six female MMTV-PyMT mice, 10-15 weeks in age, with MG9 tumors approximately 1 cm in diameter (370-580  $\text{mm}^3$ ), were administered a bolus dose of HOPE71 in saline (90  $\mu\text{L}$  75mM, 10mg, 0.17-0.31 mmol/kg, pH=7) by retroorbital injection. EPR spectra focused on MG9 tumors were recorded immediately after injection.

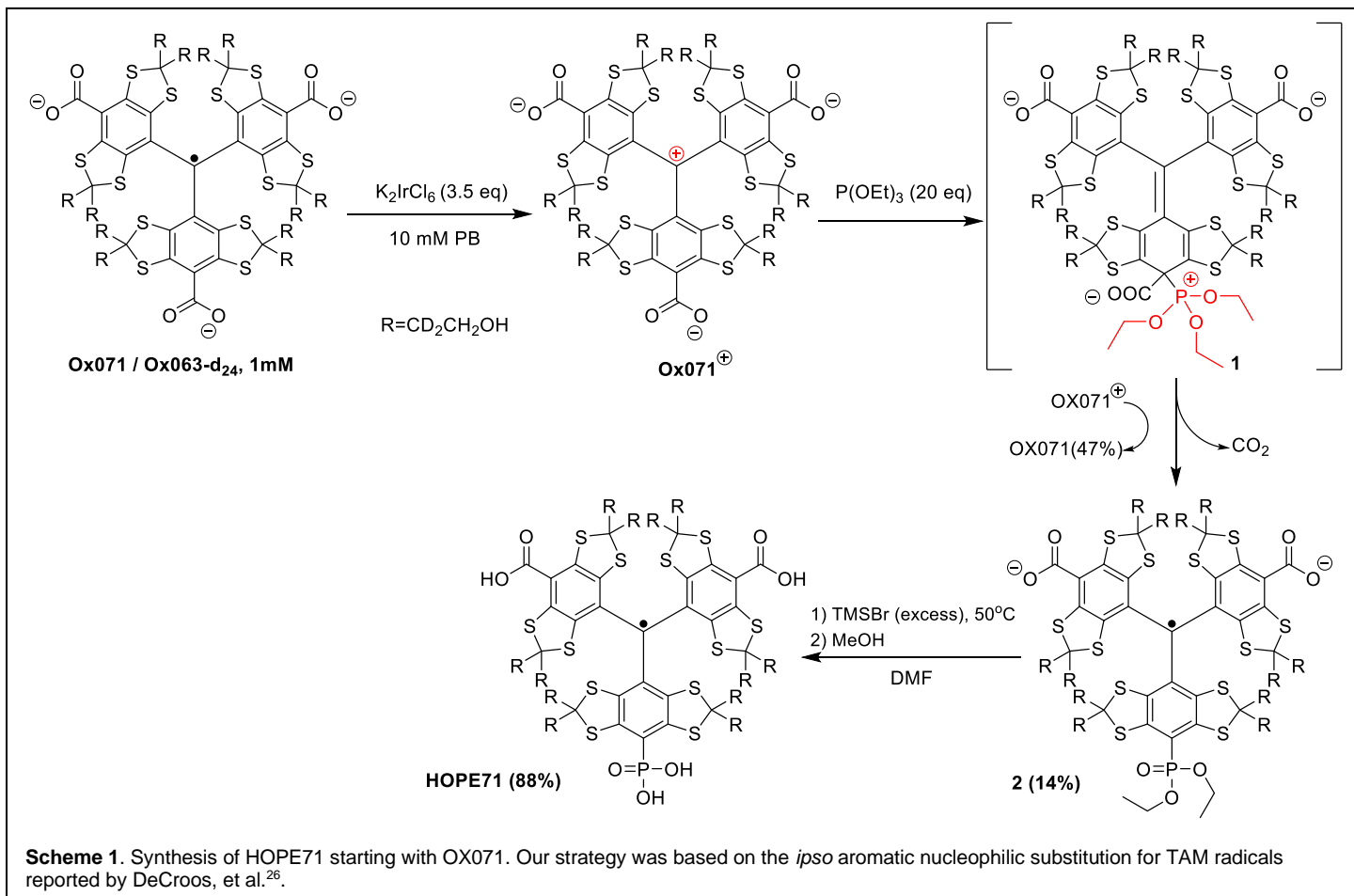
**Systemic Toxicity.** Six mice from the intravenous tumor profiling were observed for apparent signs of toxicity for 7-10 days after injection. The mass of five mice was tracked during this time.

**Longitudinal Tumor profiling.** Eight female MMTV-PyMT mice were watched starting at 9 weeks old for tumor growth on mammary gland 9 (MG9). Once palpable, the tumors on MG9 were profiled by HOPE71 EPR once to twice per week (once for early stage; twice for late stage). Four female wildtype (PyMT-/-) littermates were also profiled on the same days. The mass of the mice and the tumor volume ( $V=L \times W \times D \times 3.14/6$  or  $V= L \times W^2 \times 3.14/6$ ) was recorded along with each EPR measurement. HOPE71 in saline (15-50  $\mu\text{L}$  2mM, pH=7) was injected intratissually into the tumor or the fat pad mammary gland. EPR spectra were recorded immediately after injection. Correlation analysis was done using OriginLab software. T-tests were performed to detect differences in group means and slopes.

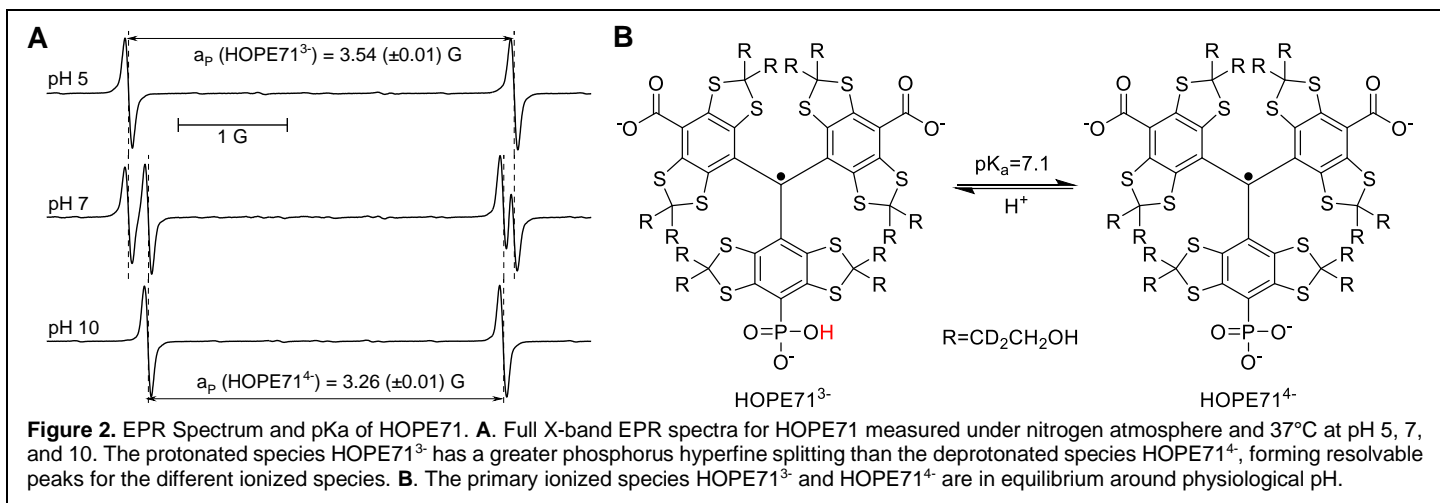
**Intratissue versus intravenous injection.** To detect if there are significant differences in the tumor profiling based on delivery method, the  $p\text{O}_2$ , pH, and  $[\text{P}_i]$  of tumors profiled with intravenous injection were compared to those of sized matched tumors profiled by intratissue injection. Two-tailed T-test for independent means was used test for statistically significant difference.

## Results and Discussion.

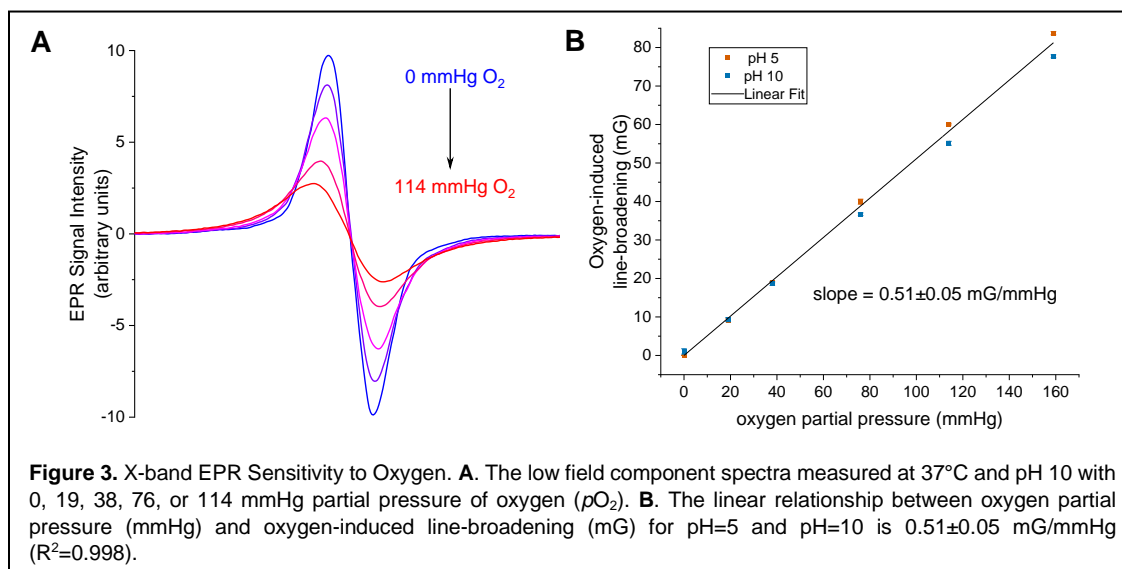
**Synthesis of HOPE71.** In order to make pTAM more biocompatible, we planned to substitute a carboxylic acid on OX071 with a phosphonate group. The strategy was to use the *ipso* aromatic nucleophilic substitution reaction for trityl radicals reported by DeCroos et. al.<sup>26</sup>. The one electron oxidation of OX071 using potassium hexachloroiridate(IV) in phosphate buffer leads to the trityl cation, which was delocalized across the aromatic groups. Then, the nucleophilic attack of triethyl phosphite at the para-position triggers an oxidative decarboxylation leading to the mono phosphonated trityl radical. The recovery of OX071 indicates that the oxidant of the intermediate **1** is the trityl cation. Therefore, for this mechanism, the theoretical yield of substituted product is capped at 50%. Also, the trityl cation was found to be very short lived in aqueous solution, and the best yield came from adding the phosphite within 10 seconds of adding the hexachloroiridate. Adding the triethyl phosphite first degraded the phosphite before forming the trityl cation. The first step afforded 14% of **2**, the protected target compound (HOPE71). Bromotrimethylsilane efficiently deprotected the phosphonate to yield 88% of HOPE71 after purification. (Sch. 1)



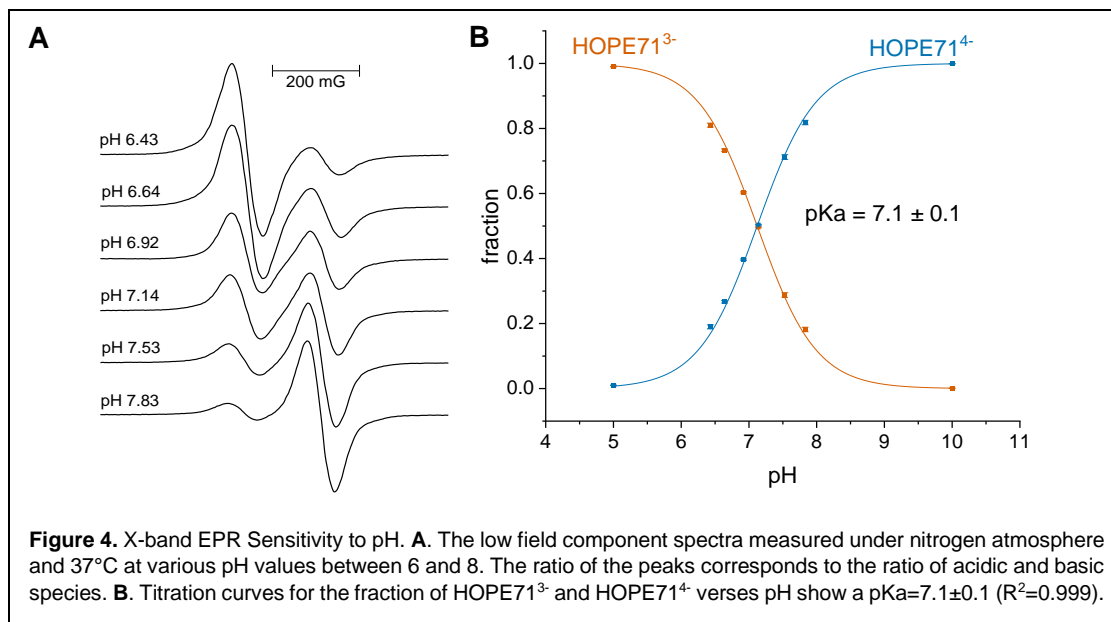
**EPR Characterization of HOPE71.** EPR characterization was first performed at X-band EPR. Fig. 2A shows the full spectrum doublet of HOPE71 at pH=5, 7, and 10. The phosphorus ( $I=1/2$ ) causes hyperfine splitting that is dependent on the protonation state. HOPE71<sup>3-</sup> has a greater hyperfine splitting constant ( $a_p = 3.54$  G, pH=5) than HOPE71<sup>4-</sup> ( $a_p = 3.26$  G, pH=10) (Fig. 2).



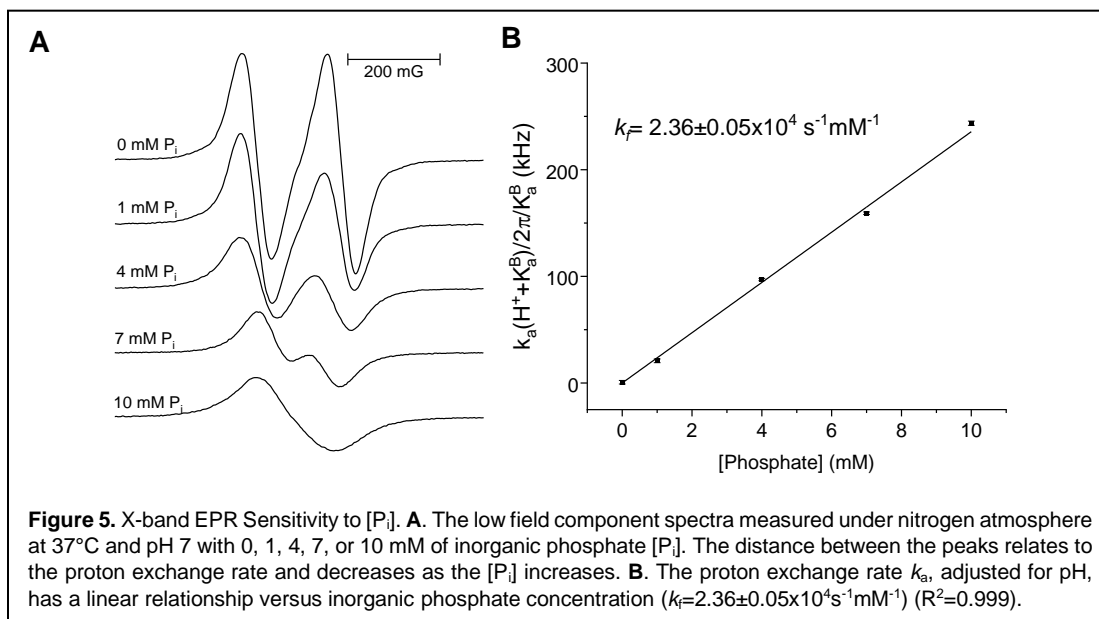
To determine the sensitivity to oxygen, low field spectra were recorded with increasing oxygen partial pressure on solutions of HOPE71 at pH=5 and 10. Fig. 3A demonstrates the effect of oxygen on the linewidth and signal intensity at pH=10. The extent of line-broadening was determined by fitting each spectrum, allowing the oxygen-induced Lorentzian linewidth to vary. The line-broadening has a strong linear correlation with oxygen partial pressure (0.51 mG/mmHg) (Fig. 3B).



In order to determine the pKa of HOPE71, a solution of HOPE71 was titrated with small amounts of acid or base, and X-band EPR spectra were recorded for six pH points between 6 and 8 in nitrogen atmosphere. The ratio of the peaks is directly correlated to the fraction of acidic and basic states (Fig. 4A). Spectral line fitting was used to determine the acidic fraction (HOPE71<sup>3-</sup>) for each pH point. By plotting the acidic and basic fractions versus pH, the titration curves show the pKa to be 7.1 ± 0.1 (Fig. 4B).



For the calibration of phosphate, solutions of HOPE71 with increasing concentrations of P<sub>i</sub> were placed under nitrogen atmosphere in the X-band EPR to record spectra of the low field peaks. The presence of phosphate buffer [HPO<sub>4</sub><sup>2-</sup>] increases the proton exchange rate on the phosphate group of HOPE71, which causes the acidic and basic peaks to coalesce (Fig. 5A). The proton exchange rate ( $k_a$ ) can be derived from spectral fitting. The exchange rate adjusted for pH has a linear relationship against [P<sub>i</sub>] and is equal to  $2.36 \pm 0.05 \times 10^4 \text{ s}^{-1} \text{ mM}^{-1}$  (Fig. 5B)<sup>25</sup>.

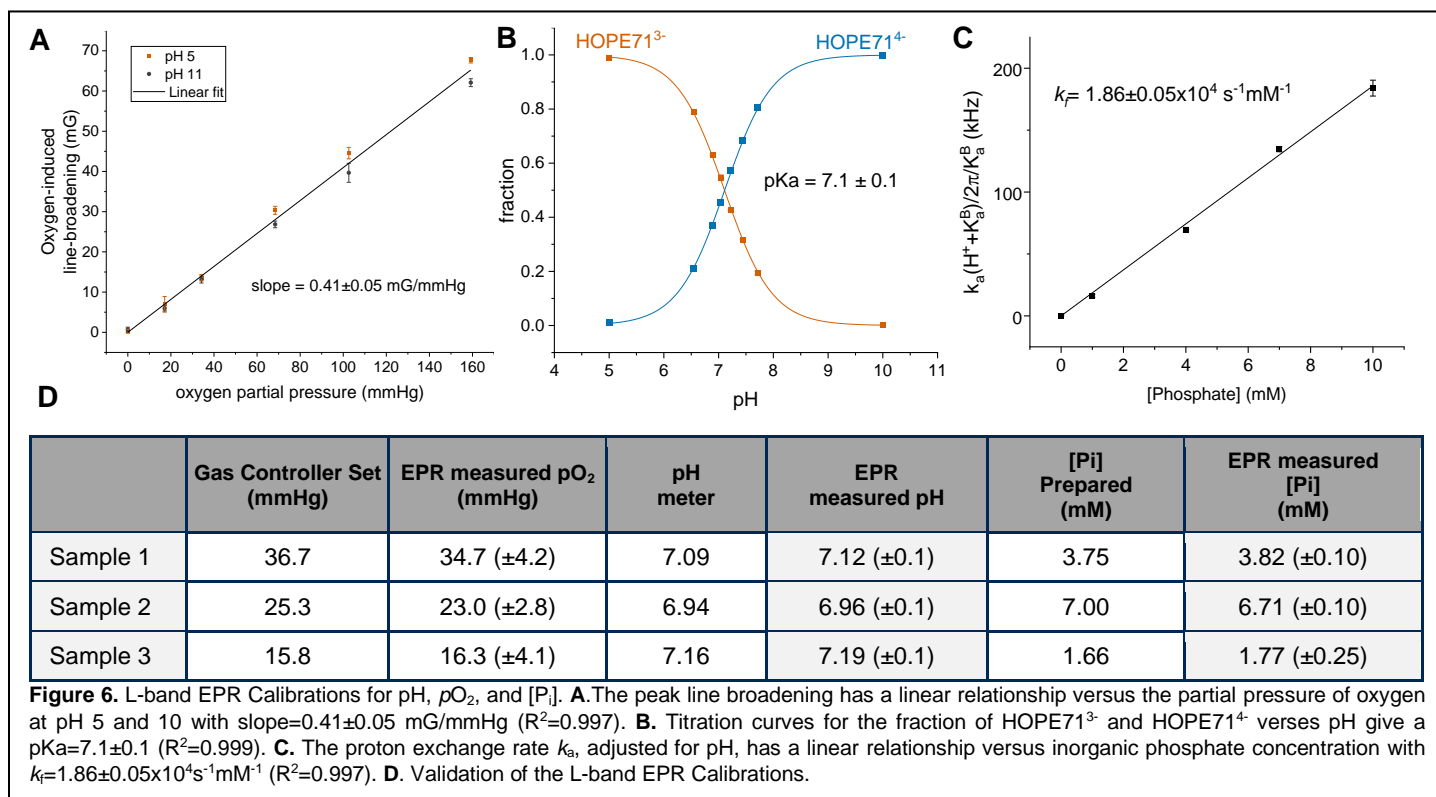


To validate the X-band sensitivities, EPR spectra were recorded for HOPE71 solutions with random  $pO_2$ , pH, and [P<sub>i</sub>] within range of the calibrations that were blinded at time of measurement. The spectra were fitted allowing oxygen linewidth, acidic fraction, and exchange rate to vary. The values for random  $pO_2$ , pH, and [P<sub>i</sub>] were extracted using the calibrations in Figs. 3-5. When comparing the prepared values to the EPR-derived values, the accuracy was within 2 mmHg of oxygen, 0.1 units of pH, and 0.3 mM of [P<sub>i</sub>] (Tbl. 1).

	Gas Controller Set (mmHg)	EPR measured $pO_2$ (mmHg)	pH meter	EPR measured pH	[Pi] Prepared (mM)	EPR measured [Pi] (mM)
Sample 1	47.9	47.0 ( $\pm 4.7$ )	7.28	7.26 ( $\pm 0.1$ )	1.88	2.14 ( $\pm 0.10$ )
Sample 2	34.9	32.2 ( $\pm 3.2$ )	7.09	7.08 ( $\pm 0.1$ )	6.88	7.00 ( $\pm 0.10$ )
Sample 3	19.0	17.3 ( $\pm 1.7$ )	6.94	6.97 ( $\pm 0.1$ )	8.25	8.22 ( $\pm 0.10$ )

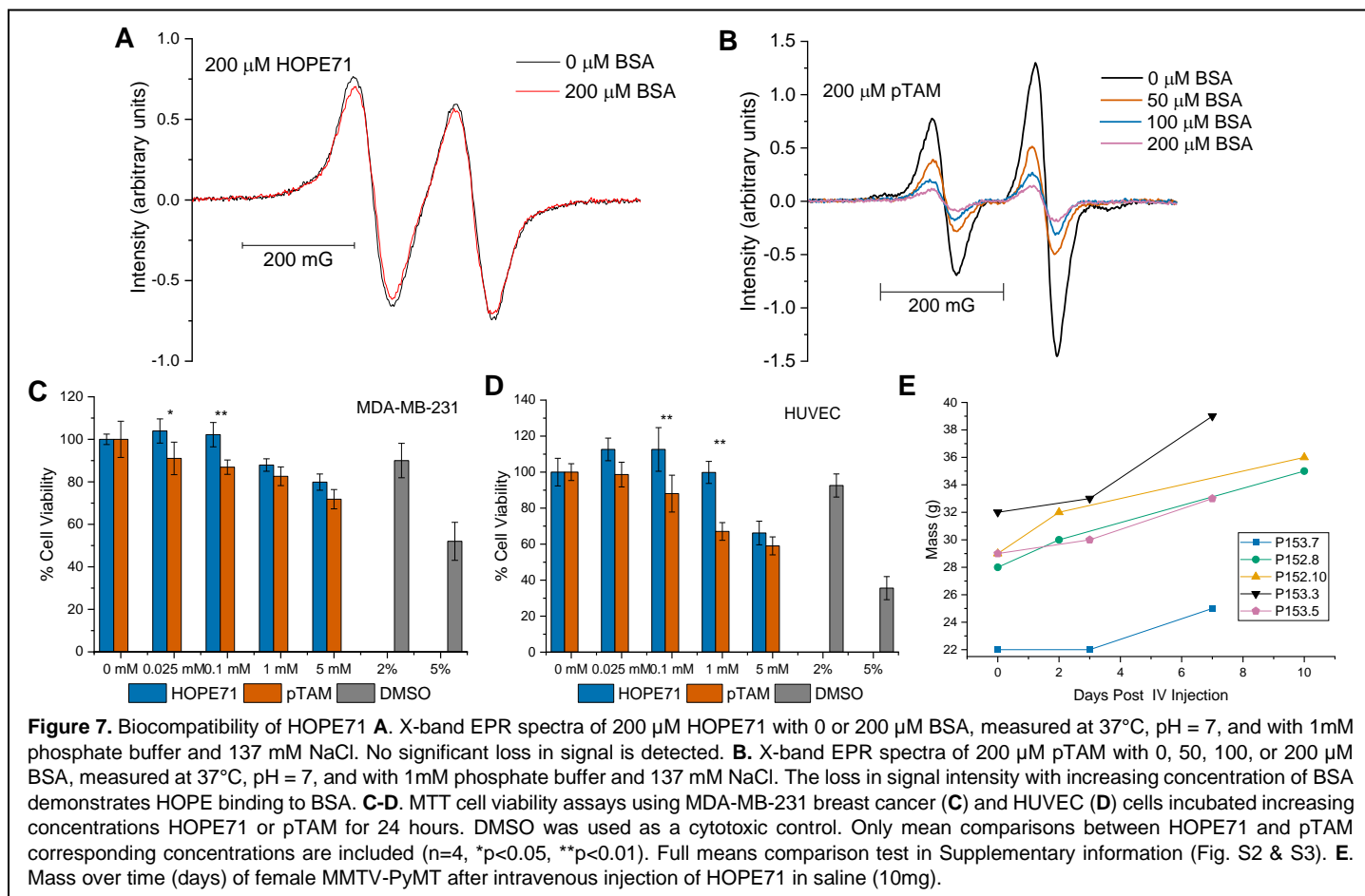
**Table 1.** Validation of the X-band EPR Calibrations. Low field component spectra were recorded for 3 samples with blinded values of pH,  $pO_2$ , and [Pi]. The spectra were fitted, and the corresponding values were derived using the calibrations in Figs. 2-4 and compared to the prepared values.

With the EPR sensitivities characterized at X-band, the calibrations were repeated for L-band for in vivo measurements. The oxygen and  $P_i$  calibrations needed to be repeated to adjust for small differences in line shape and width due to instrument variances. The pH calibration was repeated for rigor. The L-band slope for oxygen sensitivity was determined to be  $0.41 \pm 0.05$  mG/mmHg (Fig. 6A). The  $pK_a$  measured by L-band EPR agrees with the X-band measurement of  $7.1 \pm 0.1$  (Fig. 6B, Fig. 4B). For the calibration of inorganic phosphate, the L-band slope, or  $k_f$ , was found to be  $1.86 \pm 0.05 \times 10^4 s^{-1} mM^{-1}$  (Fig. 6C). Blind sample testing was repeated for the L-band calibrations and the accuracy is estimated to be within 4 mmHg of oxygen, 0.1 units of pH, and 0.3 mM of [Pi] (Fig. 6D).



**Biocompatibility of HOPE71.** The biocompatibility improvements of HOPE71 over pTAM were evaluated in several ways. Firstly, X-band EPR spectroscopy was used to show the difference in albumin interaction. For HOPE71, there was no significant loss in the spectrum signal intensity when BSA was included in equal concentration to the probe (Fig. 7A). In contrast, when equal concentration was included with pTAM, there was over 80% loss in signal intensity (Fig. 7B). This is likely due to the addition of twelve hydroxyethyl groups in HOPE71, increasing hydrophilicity and lessening protein interaction. Because albumin concentration is so high in blood, this lack of binding is imperative for intravenous dose efficiency. Next, the cytotoxicity of HOPE71 and pTAM were tested using MTT cell viability assays on rapidly dividing breast cancer cells (MDA-MB-231) and endothelial cells (HUVEC). On the breast cancer cells, both showed a minor loss in cell viability at higher concentrations (1-5mM), but cells treated with 25  $\mu M$  and 100  $\mu M$  HOPE71 had statistically more viability than those with the same concentrations of pTAM (Fig. 7C). Similarly, HUVECs had a significant loss in cell viability

for both at the highest concentration (5 mM), but with 100  $\mu$ M and 1mM, cells treated HOPE71 did better than those treated with pTAM (Fig. 7D). Because the target local concentration for L-band EPR spectroscopy is several hundred micromolar, we conclude that HOPE71 has a small decrease in cell toxicity at the required concentrations. However, in vivo systemic toxicity is much more complex than cytotoxicity. pTAM has been used in vivo by intratissue injection without obvious negative effects<sup>1</sup>, but whenever Finland based trityls are delivered intravenously, the mice quickly die<sup>18</sup>. Therefore, we observed the health of mice injected intravenously with a bolus dose of HOPE71 required for EPR spectroscopy. No mice died in the short time after injection or showed apparent signs of distress or weight loss for a week following the injection (Fig. 7E). While HOPE71 appears to have low toxicity in vivo, further evaluation by pharmacokinetics, histology, and acute toxicity (LD50) testing would help us better understand the systemic safety of HOPE71.



**Profiling tumors with HOPE71.** Because the major advantage of HOPE71 over pTAM is the potential for systemic delivery, we demonstrated its ability to profile tumors in the mammary glands of mice with spontaneous breast cancer. We found that 10 mg (0.17-0.31 mmol/kg) of HOPE71 in saline, was a sufficient bolus dose by intravenous injection to have a reliable signal-to-noise ratio for L-band EPR spectroscopy for at least 30 minutes after injection. These tumors were all on mammary gland 4 or 9 and approximately 1 cm in diameter (average volume =  $437 \pm 91$  mm<sup>3</sup>) and their  $pO_2$ , pH, and  $[P_i]$  were measured on average to be  $23.6 \pm 18.3$  mmHg,  $7.09 \pm 0.14$ , and  $4.68 \pm 0.45$  mM, respectively (Fig. 8A).

To investigate how these variables deviate from healthy tissue with tumor growth, mammary glands of the breast cancer mouse models and their wildtype littermates were longitudinally profiled by EPR spectroscopy. For these measurements, HOPE71 was injected directly into the tumor or mammary gland. The intention for intratissue (IT) as opposed to intravenous (IV) injection was to consume less probe per measurement and target the core of the tumor, which may be poorly vascularized. To determine if there was a significant difference in the EPR-measured values of  $pO_2$ , pH, and  $[P_i]$  with IV and IT injection, volume-matched data points from the IT longitudinal study were compared to the measured values in IT (n=6). Our hypothesis was that  $pO_2$  and pH measured with IV injection would be higher than those measure with IT injection because the probe would be delivered to the better vascularized regions of the tumor. The  $pO_2$  values had large variance in both groups so

no statistical conclusion can be made for oxygen, but the pH for IV delivery was significantly higher than pH for IT delivery (Fig. 8A). This may indicate that there is a pH gradient from the core of the tumor and that the probe is not as well delivered to the core upon intravenous injection. There also was no significant difference between IV and IT in the EPR-measured values of  $[P_i]$ , but elevated levels of  $P_i$  have been observed both locally in the tumor<sup>1</sup> and systemically in patients with cancer<sup>27</sup>.

Oxygenation, pH, and  $[P_i]$  of growing mammary gland tumors were compared to those of healthy mammary gland tissue of the wildtype littermate, based on the days since the tumors were recorded to be palpable. The wildtype mice were assigned a palpable date that matched their tumor littermates for comparison purposed. Throughout the entire tumor growth period, oxygen measurements appeared to be generally lower in tumors, but did not show significant difference from the wild type (Fig. 8B & 8F). On the other hand, pH was not significantly different in early tumors, but a difference did begin around 20-29 days (Fig. 8C). Acidosis continued to deviate significantly in tumors from healthy tissue as time went on (Fig. 8C & 8G). Inorganic phosphate was found to be elevated throughout most of the tumorigenesis (Fig. 8D), but linear deviation from healthy tissue was not clear (Fig. 8H). No significant correlation was found between  $pO_2$ , pH, and  $[P_i]$  (Fig. S5).

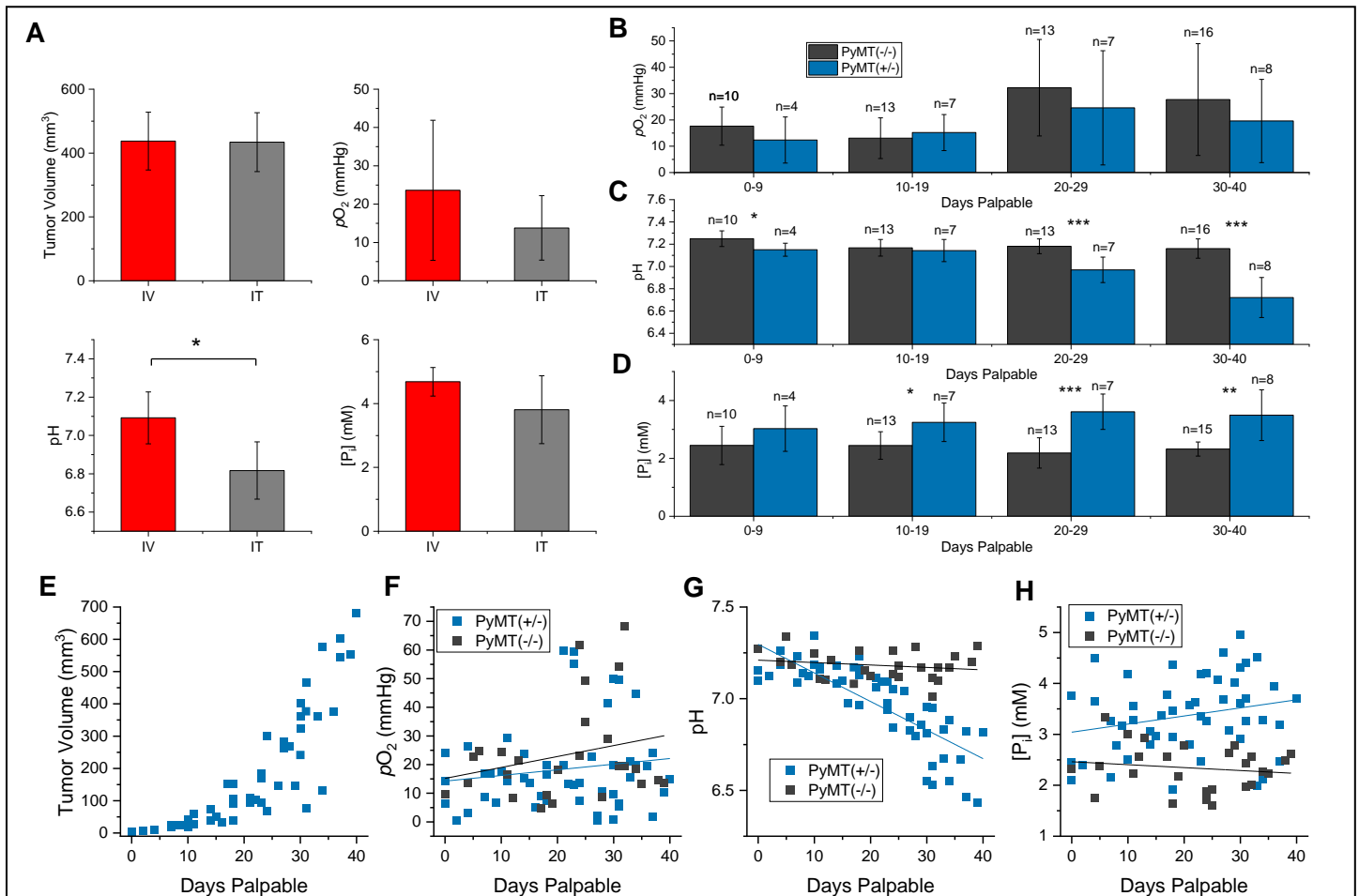


**Figure 8.** Profiling mouse breast tumors with HOPE71 **A.** The volumes,  $pO_2$ , pH, and  $[P_i]$  of tumors profiled by EPR after either intravenous (IV) or intratissue (IT) injection of HOPE71 ( $n=6$ ,  $*p<0.01$ ). **B-D.** Average  $pO_2$ , pH, and  $[P_i]$  for  $PyMT(-/-)$  ( $n=4$ ) and  $PyMT(+/-)$  ( $n=8$ ) for days palpable grouped by 10 days ( $*p<0.05$ ,  $**p<0.01$ ,  $***p<0.001$ ). **B.** No significant difference for  $pO_2$ . **C.** The difference in pH grew and was significant at 20-29 and 30-40 days. **D.** The difference in  $[P_i]$  was significant at 10-19, 20-29 and 30-40 days. **E-H.** Data points by days since palpable ( $PyMT(+/-)$  mice=8,  $n=52$ ;  $PyMT(-/-)$  mice=4,  $n=26$ ) **E.** Tumor volume of  $PyMT(+/-)$  show exponential growth versus days palpable. **F.** No significant correlation was found between  $pO_2$  and days palpable for  $PyMT(+/-)$  ( $r=0.15$ ,  $p=0.30$ ) or  $PyMT(-/-)$  ( $r=0.25$ ,  $p=0.21$ ), and no significant difference was detected between  $PyMT(+/-)$  and  $PyMT(-/-)$  slopes ( $p=0.60$ ). **G.** The slope between pH and days palpable for  $PyMT(+/-)$  was significantly different from zero, using the F-test ( $r=-0.80$ ,  $p=1.5\times 10^{-12}$ ), but the slope for  $PyMT(-/-)$  was not ( $r=-0.19$ ,  $p=0.35$ ). Significant difference was detected between  $PyMT(+/-)$  and  $PyMT(-/-)$  slopes ( $p=1\times 10^{-8}$ ). **H.** No significant correlation was found between  $[P_i]$  and days palpable for  $PyMT(+/-)$  ( $r=0.23$ ,  $p=0.09$ ) or  $PyMT(-/-)$  ( $r=-0.15$ ,  $p=0.48$ ), and no significant difference was detected between  $PyMT(+/-)$  and  $PyMT(-/-)$  slopes ( $p=0.08$ ).

## Conclusion

In conclusion, we propose HOPE71, a monophosphated hydroxyethyl trityl radical probe, as a biocompatible multifunctional EPR probe for in vivo measurement of  $pO_2$ , pH, and  $[P_i]$ . HOPE71 can be synthesized starting with OX071 by a 2-step process. The EPR-sensitivities of HOPE71 with X-band and L-band spectroscopy were verified and comparable to pTAM. Furthermore, HOPE71 has clear biocompatibility improvements over pTAM, including lack of albumin binding and systemic tolerance. The ability of HOPE71 to profile tumors in mouse models of breast cancer by EPR spectroscopy was demonstrated with both intravenous and intratissue injection. Finally, HOPE71 was used to longitudinally profile mammary gland tumors in mice, which found that pH strongly deviates with tumor growth and inorganic phosphate appears to be consistently elevated throughout most of the tumorigenesis.

## Acknowledgment

This work was partially supported by the NIH grants (USA) EB023990, EB028553, CA194013, CA192064, U54GM104942. The content is solely the responsibility of the authors and does not necessarily represent the official views of the NIH. West Virginia University Health Sciences Center is acknowledged for start-up fund to B. D. We acknowledge use of the WVU Shared Research Facilities.

## References

1. Bobko, A. A.; Eubank, T. D.; Driesschaert, B.; Dhimitruka, I.; Evans, J.; Mohammad, R.; Tchekneva, E. E.; Dikov, M. M.; Khramtsov, V. V., Interstitial Inorganic Phosphate as a Tumor Microenvironment Marker for Tumor Progression. *Sci Rep* **2017**, *7*, 41233.
2. Harris, A. L., Hypoxia—a key regulatory factor in tumour growth. *Nat Rev Cancer* **2002**, *2* (1), 38-47.
3. Gallez, B.; Baudalet, C.; Jordan, B. F., Assessment of tumor oxygenation by electron paramagnetic resonance: principles and applications. *NMR Biomed* **2004**, *17* (5), 240-62.
4. Driesschaert, B.; Marchand, V.; Levêque, P.; Gallez, B.; Marchand-Brynaert, J., A phosphonated triarylmethyl radical as a probe for measurement of pH by EPR. *Chem Commun (Camb)* **2012**, *48* (34), 4049-51.
5. Gatenby, R. A.; Gillies, R. J., Why do cancers have high aerobic glycolysis? *Nat Rev Cancer* **2004**, *4* (11), 891-9.
6. Michiels, C.; Tellier, C.; Feron, O., Cycling hypoxia: A key feature of the tumor microenvironment. *Biochim Biophys Acta* **2016**, *1866* (1), 76-86.
7. Whiteside, T. L., The tumor microenvironment and its role in promoting tumor growth. *Oncogene* **2008**, *27* (45), 5904-12.
8. Vito, A.; El-Sayes, N.; Mossman, K., Hypoxia-Driven Immune Escape in the Tumor Microenvironment. *Cells* **2020**, *9* (4).
9. Wenzl, T.; Wilkens, J. J., Modelling of the oxygen enhancement ratio for ion beam radiation therapy. *Phys Med Biol* **2011**, *56* (11), 3251-68.
10. Grimes, D. R., Estimation of the oxygen enhancement ratio for charged particle radiation. *Phys Med Biol* **2020**, *65* (15), 15NT01.
11. Lunt, S. Y.; Vander Heiden, M. G., Aerobic glycolysis: meeting the metabolic requirements of cell proliferation. *Annu Rev Cell Dev Biol* **2011**, *27*, 441-64.
12. Corbet, C.; Feron, O., Tumour acidosis: from the passenger to the driver's seat. *Nat Rev Cancer* **2017**, *17* (10), 577-593.
13. Lacerda-Abreu, M. A.; Russo-Abrahão, T.; Meyer-Fernandes, J. R., The Roles of Sodium-Independent Inorganic Phosphate Transporters in Inorganic Phosphate Homeostasis and in Cancer and Other Diseases. *Int J Mol Sci* **2020**, *21* (23).
14. Dhimitruka, I.; Bobko, A. A.; Eubank, T. D.; Komarov, D. A.; Khramtsov, V. V., Phosphonated trityl probes for concurrent in vivo tissue oxygen and pH monitoring using electron paramagnetic resonance-based techniques. *J Am Chem Soc* **2013**, *135* (15), 5904-10.
15. Bobko, A. A.; Dhimitruka, I.; Zweier, J. L.; Khramtsov, V. V., Fourier transform EPR spectroscopy of trityl radicals for multifunctional assessment of chemical microenvironment. *Angew Chem Int Ed Engl* **2014**, *53* (10), 2735-8.
16. Song, Y.; Liu, Y.; Liu, W.; Villamena, F. A.; Zweier, J. L., Characterization of the Binding of the Finland Trityl Radical with Bovine Serum Albumin. *RSC Adv* **2014**, *4* (88), 47649-47656.

17. Sanzhaeva, U.;Poncelet, M.;Tseytlin, O.;Tseytlin, M.;Gencheva, M.;Eubank, T. D.;Khramtsov, V. V.; Driesschaert, B., Synthesis, Characterization, and Application of a Highly Hydrophilic Triarylmethyl Radical for Biomedical EPR. *J Org Chem* **2020**, *85* (16), 10388-10398.
18. Lampp, L.;Rogozhnikova, O. Y.;Trukhin, D. V.;Tormyshev, V. M.;Bowman, M. K.;Devasahayam, N.;Krishna, M. C.;Mäder, K.; Imming, P., A radical containing injectable in-situ-oleogel and emulgel for prolonged in-vivo oxygen measurements with CW EPR. *Free Radic Biol Med* **2019**, *130*, 120-127.
19. Krishna, M. C.;English, S.;Yamada, K.;Yoo, J.;Murugesan, R.;Devasahayam, N.;Cook, J. A.;Golman, K.;Ardenkjaer-Larsen, J. H.;Subramanian, S.; Mitchell, J. B., Overhauser enhanced magnetic resonance imaging for tumor oximetry: coregistration of tumor anatomy and tissue oxygen concentration. *Proc Natl Acad Sci U S A* **2002**, *99* (4), 2216-21.
20. Matsumoto, K.;English, S.;Yoo, J.;Yamada, K.;Devasahayam, N.;Cook, J. A.;Mitchell, J. B.;Subramanian, S.; Krishna, M. C., Pharmacokinetics of a triarylmethyl-type paramagnetic spin probe used in EPR oximetry. *Magn Reson Med* **2004**, *52* (4), 885-92.
21. Epel, B.;Sundramoorthy, S. V.;Barth, E. D.;Mailer, C.; Halpern, H. J., Comparison of 250 MHz electron spin echo and continuous wave oxygen EPR imaging methods for in vivo applications. *Med Phys* **2011**, *38* (4), 2045-52.
22. Serda, M.;Wu, Y. K.;Barth, E. D.;Halpern, H. J.; Rawal, V. H., EPR Imaging Spin Probe Trityl Radical OX063: A Method for Its Isolation from Animal Effluent, Redox Chemistry of Its Quinone Methide Oxidation Product, and in Vivo Application in a Mouse. *Chem Res Toxicol* **2016**, *29* (12), 2153-2156.
23. Poncelet, M.;Huffman, J. L.;Khramtsov, V. V.;Dhimitruka, I.; Driesschaert, B., Synthesis of hydroxyethyl tetrathiatriarylmethyl radicals OX063 and OX071. *RSC Adv* **2019**, *9* (60), 35073-35076.
24. Gluth, T. D.;Poncelet, M.;DeVience, S.;Gencheva, M.;Hoblitzell, E. H.;Khramtsov, V. V.;Eubank, T. D.; Driesschaert, B., Large-Scale Synthesis of a Monophosphonated Tetrathiatriarylmethyl Spin Probe for concurrent *in vivo* measurement of  $pO_2$ , pH and inorganic phosphate by EPR. Submitted to RSC Advances, 2021.
25. Bobko, A. A., Chemical exchange induced Hahn echo modulation in pulsed electron paramagnetic resonance experiment. *J Magn Reson* **2020**, *315*, 106742.
26. Decroos, C.;Prangé, T.;Mansuy, D.;Boucher, J. L.; Li, Y., Unprecedented ipso aromatic nucleophilic substitution upon oxidative decarboxylation of tris(p-carboxyltetrathiaryl)methyl (TAM) radicals: a new access to diversely substituted TAM radicals. *Chem Commun (Camb)* **2011**, *47* (16), 4805-7.
27. Papaloucas, C. D.;Papaloucas, M. D.;Kouloulis, V.;Neanidis, K.;Pistevou-Gompaki, K.;Kouvaris, J.;Zygogianni, A.;Mystakidou, K.; Papaloucas, A. C., Measurement of blood phosphorus: a quick and inexpensive method for detection of the existence of cancer in the body. Too good to be true, or forgotten knowledge of the past? *Med Hypotheses* **2014**, *82* (1), 24-5.

## CHAPTER 3 – Large-Scale Synthesis of a Monophosphonated Tetrathiatriarylmethyl Spin Probe for concurrent *in vivo* measurement of $pO_2$ , pH and inorganic phosphate by EPR

Contribution: This paper was written in co-authorship with labmate, Martin Poncelet. My contribution was in the development of the MATLAB-based fitting application and performing and analyzing the cytotoxicity assay. The manuscript was recently accepted in RSC Advances.

### Large-Scale Synthesis of a Monophosphonated Tetrathiatriarylmethyl Spin Probe for concurrent *in vivo* measurement of $pO_2$ , pH and inorganic phosphate by EPR

Teresa D. Gluth<sup>ab||</sup>, Martin Poncelet<sup>ab||</sup>, Stephen DeVience<sup>bc</sup>, Marieta Gencheva<sup>bc</sup>, E. Hannah Hoblitzell<sup>bd</sup>, Valery V. Khramtsov<sup>bc</sup>, Timothy D. Eubank<sup>bd</sup> and Benoit Driesschaert<sup>ab\*</sup>

<sup>a</sup>Department of Pharmaceutical Sciences, West Virginia University, School of Pharmacy, Morgantown, WV, 26506, USA. Benoit.driesschaert@hsc.wvu.edu

<sup>b</sup>In Vivo Multifunctional Magnetic Resonance center, Robert C. Byrd Health Sciences Center, West Virginia University, Morgantown, WV, 26506, USA.

<sup>c</sup>Department of Biochemistry, West Virginia University, School of Medicine, Morgantown, WV, 26506, USA.

<sup>d</sup>Department of Microbiology, Immunology, and Cell Biology, West Virginia University, School of Medicine, Morgantown, WV, 26506, USA.

<sup>||</sup>These authors contributed equally.

#### ABSTRACT

Low-field electron paramagnetic resonance spectroscopy paired with pTAM, a mono-phosphonated triarylmethyl radical, is an unmatched technique for concurrent and non-invasive measurement of oxygen concentration, pH, and inorganic phosphate concentration for *in vivo* investigations. However, the prior reported synthesis is limited by its low yield and poor scalability, making wide-spread application of pTAM unfeasible. Here, we report a new strategy for the synthesis of pTAM with significantly greater yields demonstrated on a large scale. We also present a standalone application with user-friendly interface for automatic spectrum fitting and extraction of  $pO_2$ , pH, and [P<sub>i</sub>] values. Finally, we confirm that pTAM remains in the extracellular space and has low cytotoxicity appropriate for local injection.

Low-field Electron Paramagnetic Resonance (EPR) with the use of a molecular spin probe is a powerful technique to non-invasively measure important physiological parameters in a living animal<sup>1, 2</sup>. EPR combines high sensitivity and good penetration depth. Stable tetrathiatriarylmethyl radicals (TAMs or trityls) are ideal spin probes for in vivo EPR applications. They exhibit unprecedented stability in vivo and ultra-narrow linewidths, which result in a high signal-to-noise ratio.<sup>3</sup> TAM structures with spectral sensitivity to oxygen<sup>4</sup>, pH<sup>5, 6</sup>, thiol concentration<sup>7, 8</sup>, microviscosity<sup>9</sup>, ROS<sup>10-12</sup>, or redox<sup>13, 14</sup> have been developed. We recently reported on a mono-phosphonated tetrathiatriarylmethyl radical **pTAM** (Figure 1) whose EPR spectrum is sensitive to multiple parameters, namely oxygen concentration, pH, and inorganic phosphate concentration, [P<sub>i</sub>].<sup>15-18</sup> This multifunctional probe was utilized to profile the tumor microenvironment (TME) in various mouse models of cancer.<sup>17</sup> The unmatched capability to measure [P<sub>i</sub>] has resulted in the identification of this biomarker as a new TME marker for tumor progression.<sup>17</sup> Moreover, the ability to measure *p*O<sub>2</sub>, pH, and [P<sub>i</sub>] concurrently using the same probe allows for the direct correlation of these important parameters independent of the probe distribution, providing insight into the biological processes occurring in the TME.

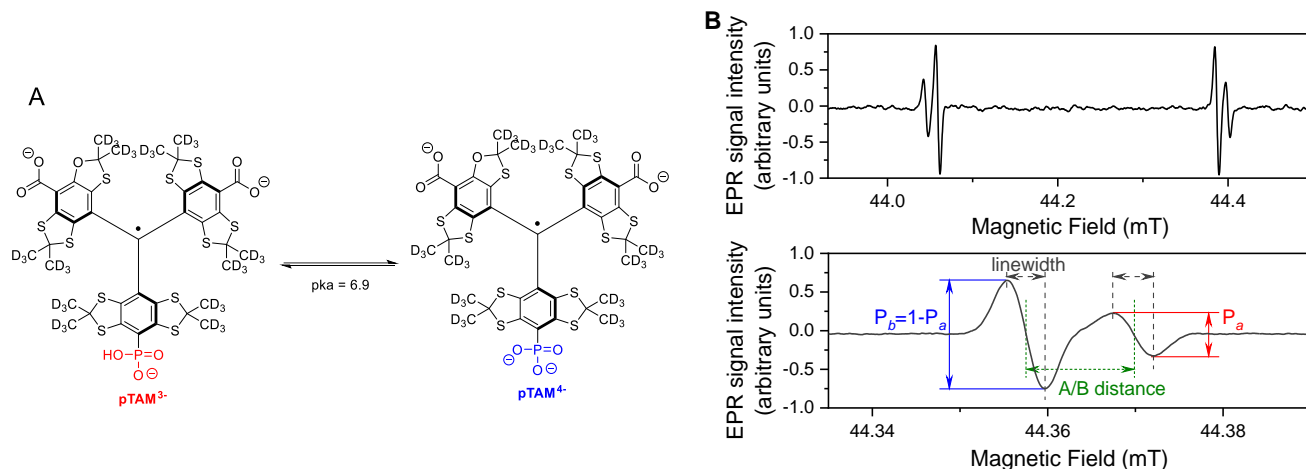
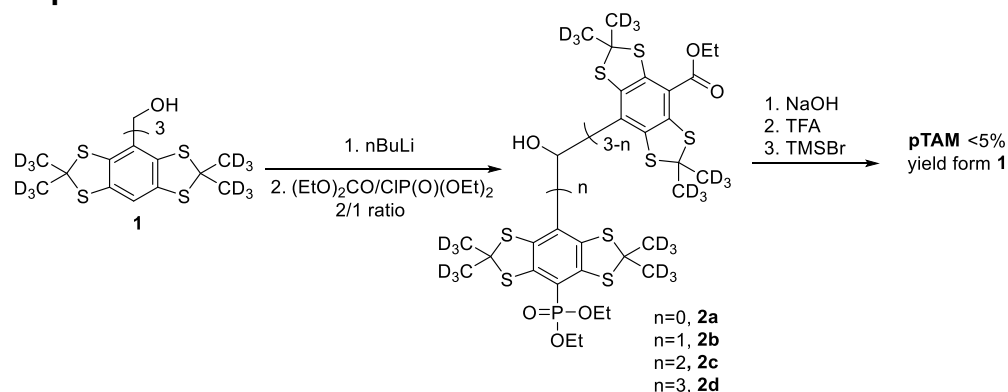


**Fig. 1.** A. Structure of **pTAM** spin probe and ionic forms at physiological pH. B. L-Band full spectrum (top) of **pTAM** at pH=7.13 showing both ionic forms present in the spectrum and zoom on the high field component (bottom). The molar fraction of the acidic form  $P_a$  versus basic form  $P_b$  is a function of the pH of the solution while the linewidths are functions of the oxygen concentration. Inorganic phosphate modulates the exchange rate between the two ionic forms and the A/B distance. Spectral simulation allows the three parameters to be extracted from the spectrum.

While this spin probe has proven to be of great importance for the study of tissue microenvironment in vivo, its current synthesis suffers from a very low yield. Indeed, the published synthesis<sup>15</sup> (Scheme 1) uses a lithiation of tetrathiatriarylmethanol **1** and subsequent reaction with a (2:1) mixture of diethyl carbonate and diethyl chlorophosphate. This reaction leads to a statistical mixture of mono-, di- and tri-phosphonated tetrathiatriarylmethanol **2n** that requires tedious purification and drastically decreases the yield of the desired **2b**. After hydrolysis of the ethyl esters using sodium hydroxide and deprotection of the phosphonic acid by TMSBr, the final **pTAM** probe was isolated with a yield of less than 5% from **1**. The published procedure allowed for isolating milligram quantity of the probe for limited in vivo studies.<sup>17</sup> However, more extensive utilization of this probe would require a synthetic method that enables gram-scale synthesis of **pTAM**.



**Scheme 1.** The first reported synthesis of **pTAM** from **1**.<sup>15</sup>

Hereby we report an efficient protocol for the large-scale production of the **pTAM** probe as well as a MATLAB application for the automatic fitting of the EPR spectra and determination of the physiological parameters, namely pH,  $pO_2$ , and  $[P_i]$ . Our new strategy takes advantage of a reaction of *ipso* nucleophilic substitution of an aromatic hydrogen or a carboxyl group on tetrathiatriarylmethyl radicals reported previously.<sup>19, 20</sup> Our synthesis starts with the deuterated Finland trityl (**dFT**) which can be synthesized at large scale without chromatography (Figure 2A).<sup>21, 22</sup> The one-electron oxidation of **dFT** with one equivalent of potassium hexachloroiridate(IV),  $K_2IrCl_6$ , in water leads to the trityl carbocation **dFT**<sup>+</sup>, which is immediately treated with ten equivalents of trimethyl phosphite. The nucleophilic addition of the phosphite in the *para*-position of the aryl ring triggers an oxidative decarboxylation, leading to the mono-phosphonic ester **pTAM-(OMe)<sub>2</sub>** in 35% conversion, as determined by HPLC/MS (Figure 2B and S6). Importantly, the HPLC/MS chromatogram shows that **dFT** radical was also generated back from the trityl carbocation **dFT**<sup>+</sup> in 65% yield, consistent with preferential oxidation of intermediate **3** by **dFT**<sup>+</sup> in line with previous reports.<sup>19, 20</sup> **dFT** can therefore be recycled for future reactions. In addition, <5% of quinone methide (**QM**) was also generated from the nucleophilic addition of water on the trityl cation (See ESI for mechanism). The use of additional equivalents of  $K_2IrCl_6$  did not increase the yield of **pTAM-(OMe)<sub>2</sub>** but did lead to higher conversion to the **QM**, TAMs with multiple phosphonates, and unidentified products. The preferential oxidation of **3** by **dFT**<sup>+</sup> explains 50% of the back conversion of the trityl radical from the cation. The slightly higher formation of **dFT** observed (65%) could be the result of the direct reduction of the trityl cation by the trimethyl phosphite.

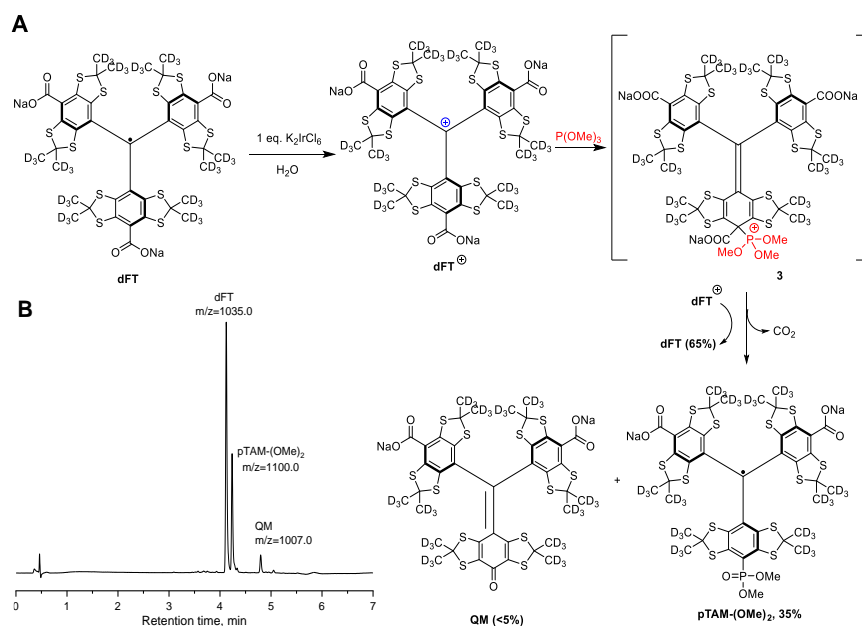
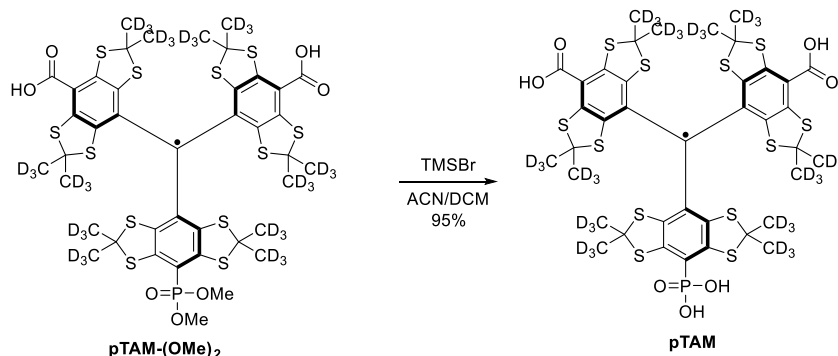


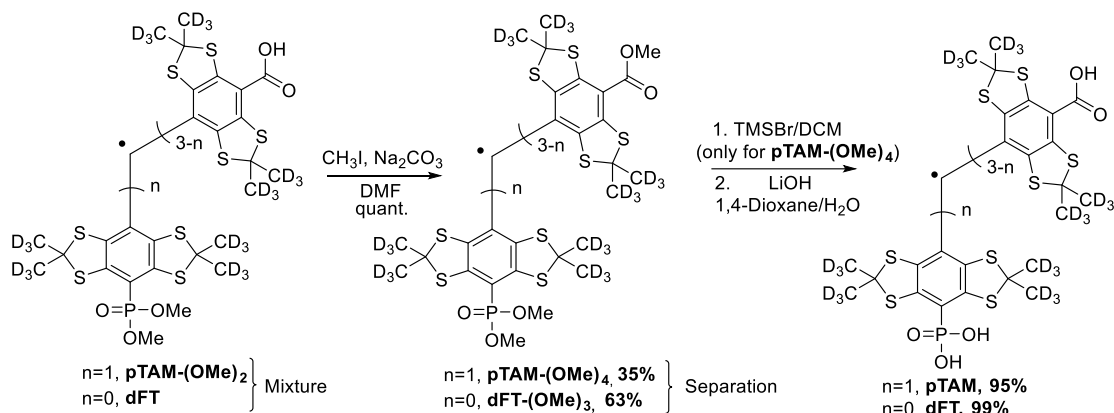
**Fig. 2.** A. Synthesis of **pTAM-(OMe)<sub>2</sub>** from **dFT** and B. HPLC/MS chromatogram and m/z ratio of the products after addition of  $P(OMe)_3$ .

The mono-phosphonated derivatives **pTAM-(OMe)<sub>2</sub>**, and **dFT** can be separated using a C18 column in 30% and 60% yield, respectively. Finally, the phosphonic acid was deprotected by treatment of **pTAM-(OMe)<sub>2</sub>** with TMSBr in 95% yield (Scheme 2).



**Scheme 2.** Deprotection of the phosphonic acid leading to **pTAM**.

However, for a multigram scale, we found the separation of **dFT** and **pTAM-(OMe)<sub>2</sub>** to be more challenging. The use of other phosphites with longer alkyl chains (triethyl-, triallyl- or tributyl phosphite), allowed for easier purification but led to smaller conversion (15-25%). On a large scale (tens of grams), the quantitative esterification of the carboxylic acids using methyl iodide and sodium carbonate in DMF directly on the **dFT/pTAM-(OMe)<sub>2</sub>** mixture (Scheme 3) allowed for easy purification by flash chromatography on silica gel. The esterified **pTAM-(OMe)<sub>4</sub>** was isolated in 35% yield from **dFT** starting material alongside with **dFT-(OMe)<sub>3</sub>** (63%). Then, the phosphonic acid was deprotected by TMSBr in DCM, and the methyl esters hydrolyzed using lithium hydroxide in 1,4-dioxane/water leading to **pTAM** in 95% yield after purification on a C18 column. **dFT-(OMe)<sub>3</sub>** was also hydrolyzed, leading to **dFT** in 99% yield with no purification needed. The relatively low conversion of **dFT** to the monophosphonated ester is compensated by the recovery of the starting material. The calculated yield based on the recovery of the starting material reaches 92%. Our large scale synthesis allowed for the selective mono-phosphorylation of **dFT** in 4 steps and two purifications. The key step is the nucleophilic quenching of the trityl cation by trimethyl phosphite leading to the mono-phosphonated derivative.



**Scheme 3.** Esterification of the carboxyl groups to allow for large-scale separation of **pTAM-(OMe)<sub>2</sub>** and **dFT-(OMe)<sub>3</sub>**. Then the carboxyl and phosphonic acids are deprotected, leading to **pTAM** and **dFT**.

The extraction of  $p\text{O}_2$ , pH, and  $[\text{P}_i]$  from the spectrum can be achieved using spectral fitting of the whole spectrum (see Fig. 1B, top) or only the high or low field EPR lines (Fig. 1B, bottom) using a homemade MATLAB algorithm as reported previously.<sup>16, 17</sup> However, to provide a user-friendly interface for those unfamiliar with MATLAB, we developed a graphical user interface for fitting the spectra and deriving the values for  $p\text{O}_2$ , pH, and  $[\text{P}_i]$ . Figure 3 demonstrates the use of the standalone application to fit a spectrum of **pTAM** administered into the mammary gland of a MMTV-PyMT mouse (See SI for calibration and use of the App).

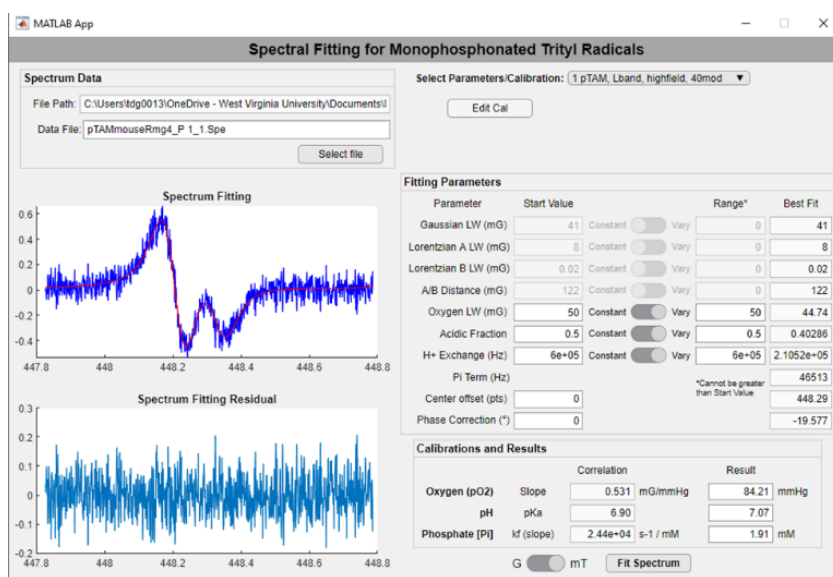


**Fig. 3.** Screenshot of the **pTAM** spectrum fitting App developed in-house with a spectrum measured of **pTAM** injected directly in the mammary gland of a MMTV-PyMT mouse. Values of  $p\text{O}_2=84.21$  mmHg,  $\text{pH}=7.07$  and  $[\text{P}_i]=1.91$  mM are automatically calculated from the experimental spectrum.

When applied in vivo, the charged nature of the probe and its large size (MW = 1073 g/mol) is expected to prevent its diffusion through the cell membrane. In order to verify that **pTAM** cannot enter the cytosol, **pTAM** (200  $\mu$ M) was incubated with  $8.5 \times 10^6$  MDA-MB-231 cells (human triple negative breast cancer cells) with and without 10 mM Gd-DTPA, a paramagnetic extracellular broadening agent.<sup>5</sup> Figure 4 shows a large broadening of the EPR lines of **pTAM** upon addition of Gd-DTPA and no residual narrow component confirming the absence of **pTAM** spin probe in the intracellular compartment. In vivo, the physiological parameters reported by **pTAM** are therefore the extracellular ones.

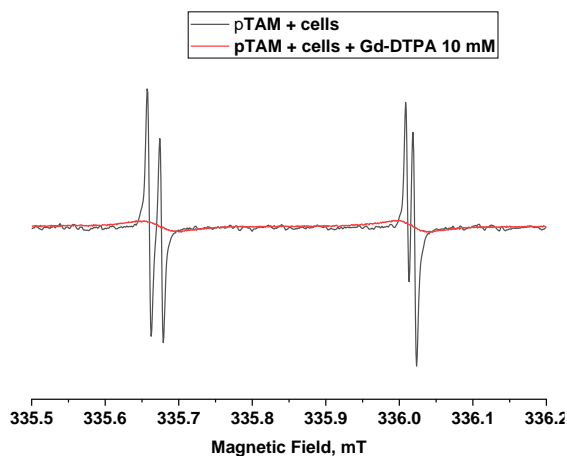


**Fig. 4.** X-Band EPR spectra of **pTAM** (200  $\mu$ M, 100  $\mu$ L) incubated with  $8.5 \times 10^6$  MDA-MB-231 cells without (black) and with 10 mM of Gd-DTPA (red) as extracellular broadening agent.

Next we assessed **pTAM** cell toxicity using the MTT assay for cell viability and proliferation. MDA-MB-231 cells at 60-70% confluency were incubated with various concentration of **pTAM** for 24h. The result (Figure 5) shows that up to 1 mM, the probe is well tolerated with  $\sim 80\%$  cell viability after 24h. It is worth noting that only a few hundred micromolar range is required for in vivo L-Band spectroscopy and the MTT results show no significant difference between 100  $\mu$ M of probe and the control. Moreover, the **pTAM** was incubated 24h with cells while in vivo the probe is cleared from the tissue in less than 1h.<sup>23</sup> Therefore, the probe can be considered as non-toxic upon local injection, which is the mode of delivery for **pTAM**.<sup>17</sup>

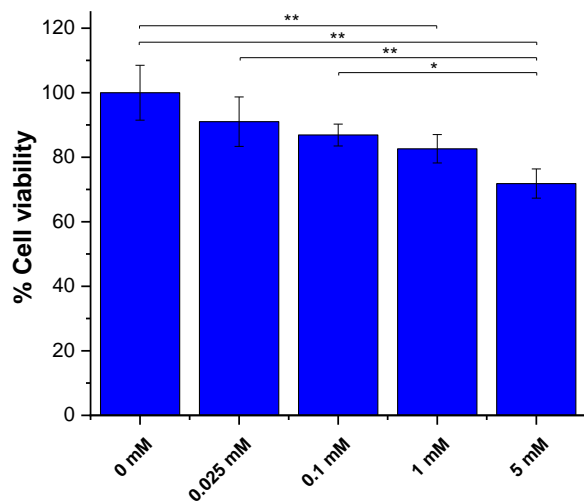


**Fig. 5.** MTT assays for **pTAM** at various concentration incubated with MDA-MB-231 cells for 24h. (n=3, \*p<0.05, \*\*p<0.01).

## Conclusions

In conclusion, we have reported a procedure to synthesize gram quantities of **pTAM** and a MATLAB application for automatic extraction of  $pO_2$ , pH, and  $[P_i]$  from an experimental spectrum. Furthermore, we showed that **pTAM** does not cross the cell membrane and has a low cell toxicity for local delivery.

## Author Contributions

B.D. conceived, supervised the project, performed the experiment and wrote the manuscript. T. D. G developed the App, performed the MTT assay and wrote the manuscript, M.P performed the synthesis and wrote the manuscript. S.D developed the fitting algorithm. M.G performed the cell and animal work, E.H.H performed the animal work. T.D.E supervised and discussed the cell and animal work. V.V.K. provided guidance on the fitting of pTAM radical and provided the initial fitting function. All authors have read and edited the manuscript.

## Acknowledgements

This work was partially supported by the NIH grants (USA): EB023990, EB028553, CA194013, CA192064, U54GM104942. The content is solely the responsibility of the authors and does not necessarily represent the official views of the NIH. West Virginia University Health Sciences Center is acknowledged for start-up fund to B.D. Andrey A. Bobko is acknowledged for sharing the initial MATLAB fitting function of pTAM.

## Conflicts of interest

There are no conflicts to declare.

## Notes and references

1. V. V. Khramtsov, A. A. Bobko, M. Tseytlin and B. Driesschaert, *Anal. Chem.*, 2017, **89**, 4758-4771.
2. J. R. Biller and J. E. McPeak, *Appl Magn Reson*, 2021, DOI: 10.1007/s00723-020-01304-z, 1-27.
3. J. H. Ardenkjær-Larsen, I. Laursen, I. Leunbach, G. Ehnholm, L. G. Wistrand, J. S. Petersson and K. Golman, *J. Magn. Reson.*, 1998, **133**, 1-12.
4. U. Sanzhaeva, M. Poncelet, O. Tseytlin, M. Tseytlin, M. Gencheva, T. D. Eubank, V. V. Khramtsov and B. Driesschaert, *J. Org. Chem.*, 2020, **85**, 10388-10398.
5. V. Marchand, P. Levêque, B. Driesschaert, J. Marchand-Brynaert and B. Gallez, *Magn. Reson. Med.*, 2017, **77**, 2438-2443.
6. B. Driesschaert, V. Marchand, P. Levêque, B. Gallez and J. Marchand-Brynaert, *Chem. Commun.*, 2012, **48**, 4049-4051.
7. Y. Liu, Y. Song, A. Rockenbauer, J. Sun, C. Hemann, F. A. Villamena and J. L. Zweier, *J. Org. Chem.*, 2011, **76**, 3853-3860.
8. X. Tan, K. Ji, X. Wang, R. Yao, G. Han, F. A. Villamena, J. L. Zweier, Y. Song, A. Rockenbauer and Y. Liu, *Angew. Chem. Int. Ed.*, 2020, **59**, 928-934.
9. M. Poncelet and B. Driesschaert, *Angew. Chem. Int. Ed.*, 2020, **59**, 16451-16454.
10. B. Driesschaert, A. A. Bobko, V. V. Khramtsov and J. L. Zweier, *Cell Biochem. Biophys.*, 2017, **75**, 241-246.
11. C. Rizzi, A. Samouilov, V. Kumar Kutala, N. L. Parinandi, J. L. Zweier and P. Kuppusamy, *Free. Rad. Biol. Med.*, 2003, **35**, 1608-1618.
12. V. K. Kutala, N. L. Parinandi, J. L. Zweier and P. Kuppusamy, *Arch. Biochem. Biophys.*, 2004, **424**, 81-88.
13. Y. Liu, F. A. Villamena, Y. Song, J. Sun, A. Rockenbauer and J. L. Zweier, *J. Org. Chem.*, 2010, **75**, 7796-7802.
14. Y. Liu, F. A. Villamena, A. Rockenbauer and J. L. Zweier, *Chem. Commun.*, 2010, **46**, 628-630.
15. I. Dhimitruka, A. A. Bobko, T. D. Eubank, D. A. Komarov and V. V. Khramtsov, *J. Am. Chem. Soc.*, 2013, **135**, 5904-5910.
16. A. A. Bobko, I. Dhimitruka, J. L. Zweier and V. V. Khramtsov, *Angew. Chem. Int. Ed.*, 2014, **53**, 2735-2738.
17. A. A. Bobko, T. D. Eubank, B. Driesschaert, I. Dhimitruka, J. Evans, R. Mohammad, E. E. Tchekneva, M. M. Dikov and V. V. Khramtsov, *Sci. Report.*, 2017, **7**, 41233.
18. A. Taguchi, S. DeVience, B. Driesschaert, V. V. Khramtsov and H. Hirata, *Analyst*, 2020, **145**, 3236-3244.
19. C. Decroos, T. Prangé, D. Mansuy, J.-L. Boucher and Y. Li, *Chem. Commun.*, 2011, **47**, 4805-4807.
20. O. Y. Rogozhnikova, V. G. Vasiliev, T. I. Troitskaya, D. V. Trukhin, T. V. Mikhailina, H. J. Halpern and V. M. Tormyshev, *Eur. J. Org. Chem.*, 2013, **2013**, 3347-3355.
21. I. Dhimitruka, M. Velayutham, A. A. Bobko, V. V. Khramtsov, F. A. Villamena, C. M. Hadad and J. L. Zweier, *Bioorg. Med. Chem. Lett.*, 2007, **17**, 6801-6805.
22. I. Dhimitruka, O. Grigorieva, J. L. Zweier and V. V. Khramtsov, *Bioorg. Med. Chem. Lett.*, 2010, **20**, 3946-3949.
23. A. A. Gorodetskii, T. D. Eubank, B. Driesschaert, M. Poncelet, E. Ellis, V. V. Khramtsov and A. A. Bobko, *Sci. Report.*, 2019, **9**, 12093.

## CHAPTER 4 – Cleavage-resistant Protein Labeling with Hydrophilic Trityl Enables Distance Measurements *In-Cell*

Contribution: This paper was prepared in collaboration with the Saxena lab at the University of Pittsburgh. My contribution was in the synthesis of mOX063-d<sub>24</sub>, a hydrophilic trityl probe for cleavage-resistant spin labeling of proteins. This paper has been published in the Journal of Physical Chemistry part B.

J. Phys. Chem. B **2021**; 125(20):5265-5274.

### Cleavage-resistant Protein Labeling with Hydrophilic Trityl Enables Distance Measurements *In-Cell*

Zikri Hasanbasri†, Kevin Singewald†, Teresa D. Gluth‡, Benoit Driesschaert‡\*, Sunil Saxena†\*

†Department of Chemistry, University of Pittsburgh, Pittsburgh, Pennsylvania 15260, United States

‡Department of Pharmaceutical Sciences, School of Pharmacy & In Vivo Multifunctional Magnetic Resonance (IMMR) Center, Health Sciences Center, West Virginia University, Morgantown, West Virginia 26506, United States

#### ABSTRACT

Sensitive *in-cell* distance measurements of proteins using pulsed-Electron Spin Resonance (ESR) requires spin-labels that are both reduction-resistant and cleavage-resistant. Among the reduction-resistant radical moieties, the hydrophilic trityl core known as OX063 is particularly promising due to its long phase-memory relaxation time ( $T_m$ ). This property of OX063 allows for the detection of sufficiently intense ESR signal to reliably measure longer distances. Furthermore, the OX063's  $T_m$  remains sufficiently long at higher temperatures, which opens up the possibility for distance measurements to be done at temperatures above 50 K. In this work, we synthesized a deuterated OX063 with a maleimide linker (mOX063-d<sub>24</sub>). The combination of deuterated OX063's hydrophilicity and the maleimide linker allows for highly efficient labeling of protein while also being uncleavable in cells. We show that the long  $T_m$  of mOX063-d<sub>24</sub> allow distance measurements at temperatures up to 150 K. Additionally, the distance measurement at 150 K is more sensitive than the measurement at 80 K. The sensitivity gain is due to the significantly short longitudinal relaxation time ( $T_1$ ) at higher temperatures which allows for more data to be averaged given the same amount of time. In addition to *in vitro* experiments, we show that mOX063-d<sub>24</sub> allows distance measurements in *Xenopus laevis* oocytes. Interestingly, the  $T_m$  of mOX063-d<sub>24</sub> is still sufficiently long even in the crowded environment of the cell, which allows for distance measurements in-cells. Overall, mOX063-d<sub>24</sub> provides highly sensitive distance measurements both *in vitro* and *in-cells*.

## Introduction

Understanding how proteins adapt in their cellular environments is of immense interest in structural biology. The crowded environment inside cells can affect protein folding and stability<sup>1-7</sup>. For example, phosphoglycerate kinase (PGK) is more stable in zebrafish tissues<sup>8</sup> and human osteosarcoma cells<sup>5</sup> than *in vitro*. The increase in stability due to molecular crowding has also been observed with other proteins such as frataxin<sup>9</sup>, ubiquitin<sup>10</sup>, hen egg white lysozyme<sup>11</sup>, and calcineurin<sup>12</sup>. In contrast, the dimerization of baculoviral IAP repeat (BIR1) domain of X chromosome-linked inhibitor of apoptosis (XIAP) is destabilized *in vivo*<sup>13</sup>. The destabilization effect are also seen in other protein dimers that are not spherical in shape<sup>14,15</sup>. These experiments are indicators that the *in-cell* environment modulates protein structure and function, which vary case-by-case. Overall, *in-cell* experiments are required to understand the behavior of proteins in the context of cellular function.

Electron Spin Resonance (ESR) emerged as a widely applicable technique to measure dynamics and distance constraints *in vitro* and *in-cell*. For such ESR measurements, the normally diamagnetic proteins can be functionalized with a spin-label using site-directed spin labeling methodologies<sup>16-19</sup>. The combination of ESR and spin labeling enables the measurement of the dynamics at the labeled site<sup>20,21</sup> or measuring distances between the labeled sites of a protein<sup>22-28</sup>. Distance measurements have been particularly useful for shedding light on the changes in protein conformations<sup>29-37</sup>, the assembly of large complexes<sup>38-41</sup>, and the binding of substrates and metal ions<sup>42-45</sup>. Additionally, these distance measurements have been performed *in-cell* for proteins<sup>46-48</sup> and DNA<sup>49,50</sup>. The primary challenge for distance measurements *in-cell* is the reduction of spin-labels within the highly reducing cytosolic environment<sup>51</sup>. An intriguing new strategy for *in-cell* measurements is the use of genetically encoded non-canonical amino acids technology as an *in situ* labeling strategy<sup>52-55</sup>. In particular, a photo-caged radical amino acid can be incorporated into a protein during translation<sup>56</sup>. Only after the induction of light will the photo-cage is released to expose the nitroxide radical for ESR measurements. In addition to non-canonical amino acids, reduction resistant spin-labels such as sterically shielded nitroxides<sup>57,58</sup>, Gd(III)-based spin-labels<sup>59-61</sup>, and triarylmethyls (TAMs, trityls)<sup>62-64</sup> have been developed.

Trityls have a lot of potential as a class of spin-labels for several reasons. First, trityls are highly resistant to reduction *in-cell* due to the steric-shielding of its radical<sup>65-67</sup>. Second, trityls have appreciable relaxation times even at physiological temperatures<sup>68</sup>. Third, trityls have narrow spectral shape that leads to efficient excitation of the electrons and intense ESR signal<sup>69</sup>. Overall, trityl spin-labels have proved suitable for distance measurements at physiological temperatures or *in-cell*. The most explored trityl spin-labels are based on the Finland trityl radical (FT) shown in Figure 1A, which have successfully provided distance measurements at room temperature<sup>70,71</sup> and *in-cell*<sup>72,73</sup>. However, FT-based spin-labels usage is still challenging due to the complications in the labeling process.

The spin-labeling process typically entails a reaction between the spin-label and a cysteine residue to label the protein at a specific site. However, FT can bind non-specifically to membranes<sup>74</sup> or proteins<sup>75</sup>. Additionally, FT tends to self-aggregate<sup>76,77</sup>. As a result, efficient labeling of FT requires extensive washing of proteins that are immobilized on a solid support<sup>63</sup> or maintaining FT concentration to be less than 30  $\mu\text{M}$  throughout the process to minimize aggregation<sup>78</sup>.

Even after the labeling process, the phase-memory relaxation time ( $T_m$ ) of FT is significantly reduced upon protein binding<sup>63,78</sup>, which leads to a weaker signal. Additionally, the longitudinal relaxation time ( $T_1$ ) is significantly long at temperatures that are typical for ESR distance measurements ( $\leq 50\text{K}$ )<sup>78</sup>, which leads to longer experimental time. Overall, the short  $T_m$  and long  $T_1$  of FT-based spin labels diminish the sensitivity gain from the efficient excitation of FT. As a result, FT's sensitivity for distance measurements is comparable to distance measurements using commercially available nitroxide spin-label<sup>78</sup>.

As an alternative, a hydrophilic trityl spin-label, based on the OX063 radical shown in Figure 1A, has been recently developed that allows for straightforward labeling procedure without non-specific binding or aggregation<sup>79</sup>. Interestingly, deuterated OX063 (OX063-d<sub>24</sub>) was reported to have the longest transversal relaxation time at 50K to date ( $T_m = 6.3 \mu\text{s}$ )<sup>79</sup>. Additionally, OX063-d<sub>24</sub> has been shown to also have a sufficiently long phase-memory relaxation time even at 200 K ( $T_m = 3 \mu\text{s}$ )<sup>46</sup>. Because  $T_1$  is generally shorter at higher temperatures, OX063-d<sub>24</sub> has the potential for highly sensitive distance measurements at temperatures higher than 50K. Despite OX063-d<sub>24</sub>'s improvement over FT, OX063-d<sub>24</sub> only utilized a methanethiosulfonate linker so far, which is a limiting factor for *in-cell* experiments. This linker labels a protein by forming disulfide bonds with cysteines, which can be cleaved inside cells<sup>48</sup>. On the other hand, a maleimide linker reacts with a cysteine to form a thioether bond, which is uncleavable under normal physiological condition<sup>47</sup>. In response to the need of a hydrophilic trityl with an uncleavable linker, a hybrid of OX063 and short-linker maleimide (SLIM)<sup>73</sup> known as Ox-SLIM was recently developed (Figure 1A)<sup>80</sup>. Unlike OX063, the trityl core of Ox-SLIM has one of its bithioketalaryl moieties remain unhydroxylated to bear the short maleimide linker. The hydrophilicity of Ox-SLIM

permitted the labeling efficiency of ~85%. These results motivate the development of hydrophilic trityl labels with high labeling efficiency for *in-cell* distance measurements.

To increase the viability of OX063-d<sub>24</sub>-based spin-labels, we have developed a new OX063-d<sub>24</sub> spin label with a maleimide linker (mOX063-d<sub>24</sub>) shown in Figure 1A. The maleimide linker allows for mOX063-d<sub>24</sub> to maintain its linkage with the protein *in-cell*<sup>81</sup>. We explored two aspects of mOX063-d<sub>24</sub> for distance measurements in proteins. First, we show how mOX063-d<sub>24</sub> provides highly sensitive distance measurements at temperatures higher than the typical  $\leq 50K$  *in vitro*. Second, we showcase the usage of mOX063-d<sub>24</sub> for experiments *in-cell*, specifically in *Xenopus laevis* oocytes. When exploring these two aspects, spin-labeling and distance measurements were done on the immunoglobulin binding domain of protein G (GB1)<sup>82</sup>, a 56-residue globular protein (Figure 1B).

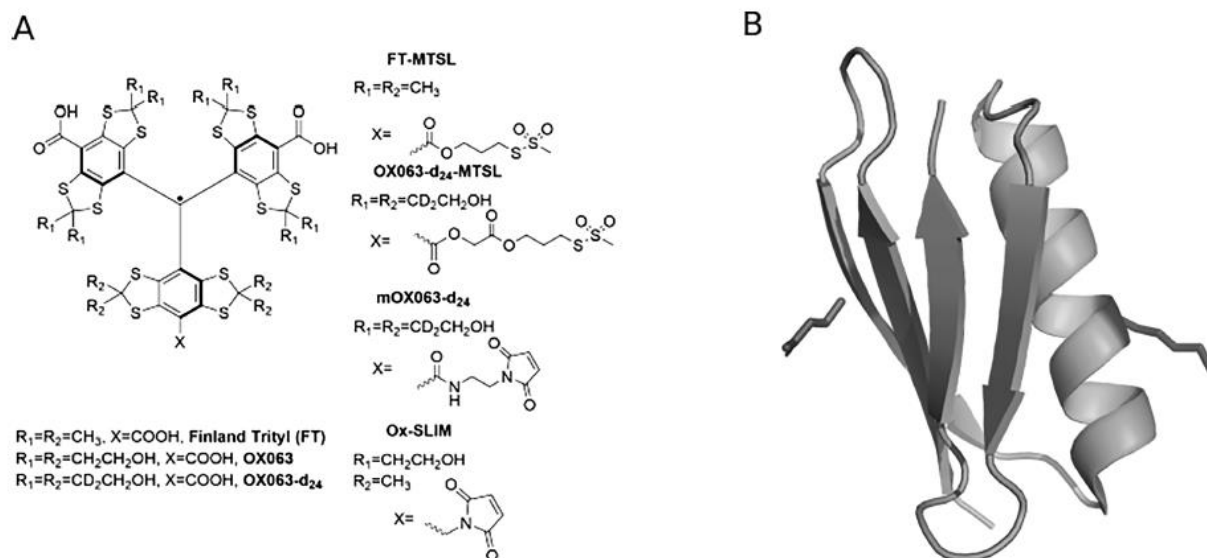


**Figure 1.** A) Representation of TAM-based spin labels, FT-MTSL, OX063-d<sub>24</sub>-MTSL, mOX063-d<sub>24</sub>, and Ox-SLIM. B) Three-dimensional model of E15C/K28C GB1 based on the wild-type GB1 crystal structure (PDB:2QMT). The side chains of the mutated cysteines are represented as lines. Reproduced from Hasanbasri, *JPC* 2021.

## Methods

**Synthesis of mOX063-d<sub>24</sub>.** OX063-d<sub>24</sub> trisodium salt (112 mg, 0.077 mmol, 1eq.), synthesized using our previously reported protocols<sup>83</sup>, was dissolved in anhydrous dimethylformamide (DMF) (100 mL) under argon at room temperature. Benzotriazol-1-yl-oxytripyridinophosphonium hexafluorophosphate (PyBOP) (28 mg, 0.054 mmol, 0.7 eq.) in DMF (1 mL) was added; the green solution turned into a red-brown colored solution. Then, N-(2-aminoethyl)maleimide trifluoroacetate salt (23 mg, 0.09 mmol, 1.2 eq.) in DMF (1 mL) and N,N-diisopropylethylamine (DIEA) (26.8  $\mu$ L, 1.4 mmol, 2eq.) were added. The solution turned back to green. The reaction mixture was diluted 20x with deionized water and acidified to approximately pH~2 with trifluoroacetic acid. The crude product was loaded into a C18 cartridge and purified by reverse-phase chromatography using a C18 column with a gradient of water/acetonitrile (both containing 0.1 % TFA) 95/5 to 85/15. The purified product was freeze-dried, then dissolved in water, titrated to pH=7 with NaOH, and freeze-dried again to provide 48 mg (40%) of mOX063-d<sub>24</sub> as a disodium salt. The purity assessed by HPLC reached >95% as shown in Figure S1. HRMS characterization is shown in Figure S2.

**GB1 labeling protocol.** E15C/K28C GB1 and E15C GB1 expression and purification were performed as previously described<sup>84</sup>. The GB1 mutant was reacted with tris(2-carboxyethyl)phosphine (TCEP) overnight at 4 °C to reduce any disulfide formation. To label the protein, GB1 was run through four 5 mL GE Healthcare Hitrap desalting columns, to remove any TCEP, directly into a solution of mOX063-d<sub>24</sub>. The final solution of 10:1 of mOX063-d<sub>24</sub>:GB1 was allowed to react overnight at 4 °C. The spin-labeled protein was concentrated using Sartorius VivaSpin Turbo 4 centrifugal filter units with a molecular weight cutoff of 5 kDa to remove the unreacted label. The final solution was prepared in PBS pH 7.4. Concentration and labeling efficiencies were calculated from UV-Vis measurement using Nanodrop2000 Spectrophotometer from Thermo Scientific. The extinction coefficient of GB1 was obtained from the ProtParam tool (<https://web.expasy.org/protparam/>).

**Cellular extracts and oocyte microinjection.** Oocytes were obtained from Carolina Biological Supplies. The cytosol was extracted following previously published protocol<sup>85</sup>. Cytosol sample was prepared at 50  $\mu$ L containing



labeled E15C GB1. This result is expected because of the detachment of the spin label during sample preparation in trifluoroacetic acid for ESI-MS and has been reported before using a maleimide-linked FT<sup>78</sup>.

The final product was characterized using UV-Vis to assess spin-labeling efficiency. This data is shown in Figure 2. The spectrum features two distinctive peaks at 280 nm and 469 nm. Only mOX063-d<sub>24</sub> contributes toward the 469-nm peak<sup>89</sup>, while both mOX063-d<sub>24</sub> and GB1 contribute toward the 280-nm peak. The UV-Vis spectrum was analyzed using the deconvolution method, as depicted in Figure 2<sup>78</sup>, which fits the mOX063-d<sub>24</sub>-GB1 spectrum using GB1's UV-Vis spectrum (dash-dotted line) and mOX063-d<sub>24</sub>'s UV-Vis spectrum (dotted line). The deconvolution allowed us to obtain the absorbance of GB1 at 280 nm ( $\epsilon_{280} = 9970 \text{ M}^{-1} \text{ cm}^{-1}$ ) and mOX063-d<sub>24</sub> at 469 nm ( $\epsilon_{469} = 16000 \text{ M}^{-1} \text{ cm}^{-1}$ )<sup>89</sup>, which were used to calculate their concentrations. The final concentrations of GB1 and mOX063-d<sub>24</sub> in the sample are 165.0  $\mu\text{M}$  and 161.9  $\mu\text{M}$ , respectively. Therefore, the ratio of GB1:mOX063-d<sub>24</sub> purified is about 1:0.98. Overall, our UV-Vis results indicate efficient mOX063-d<sub>24</sub> labeling of cysteines on GB1.

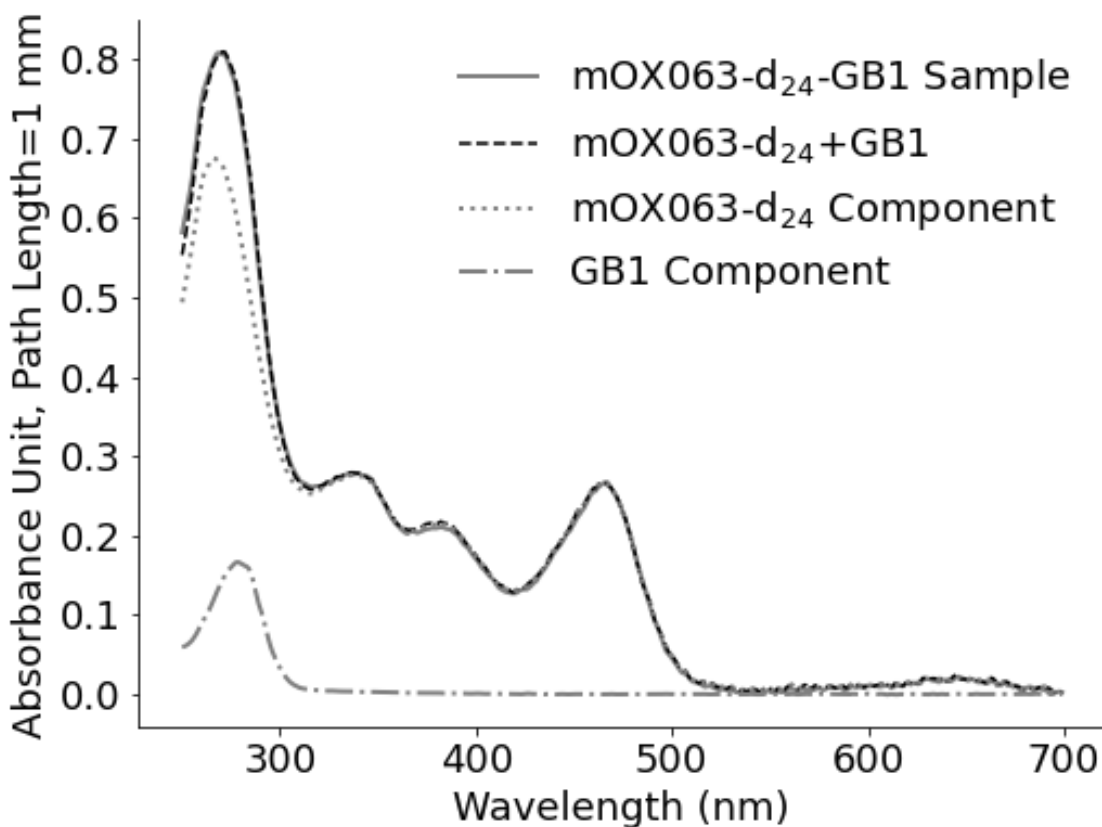


**Figure 2.** UV-Vis spectrum of mOX063-d<sub>24</sub>-GB1 sample (gray line). The mOX063-d<sub>24</sub>-GB1 spectrum was deconvoluted into its GB1 (dash-dotted line) and mOX063-d<sub>24</sub> (dotted line) components. The sum of the two components (dashed line) fits well with the mOX063-d<sub>24</sub>-GB1 spectrum. Reproduced from Hasanbasri, *JPC* 2021.

To further validate the labeling efficiency, the mOX063-d<sub>24</sub>-GB1 sample was characterized using CW-ESR at room temperature. Figure 3A and 3B show the CW-ESR spectrum of mOX063-d<sub>24</sub> bound to GB1 and free mOX063-d<sub>24</sub>. The free mOX063-d<sub>24</sub> contained a superhyperfine interaction with the amide nitrogen ( $a^N \sim 220$  mG) on the linker, depicted as a partially resolved triplet splitting of the ESR lineshape. This nitrogen hyperfine is consistent with previously published trityls with <sup>14</sup>N-containing linkers<sup>79,90,91</sup>. After mOX063-d<sub>24</sub> reacted with GB1, the superhyperfine nitrogen were broadened and unresolved due to the slower tumbling rate upon protein binding, seen in Figure 3B<sup>79</sup>. However, the tumbling rate after protein binding is still rapid enough to resolve the satellite <sup>13</sup>C peaks in the CW of GB1-bound mOX063-d<sub>24</sub>, seen in Figure 3A. This behavior has been described in a previous report of OX063-d<sub>24</sub> spin-label<sup>79</sup>. Spin-counting of the mOX063-d<sub>24</sub>-GB1 CW spectrum yields a spin concentration of 190 μM. Given the protein concentration of 194 μM, these results indicate a labeling efficiency of 97%, which agrees with the UV-Vis data.

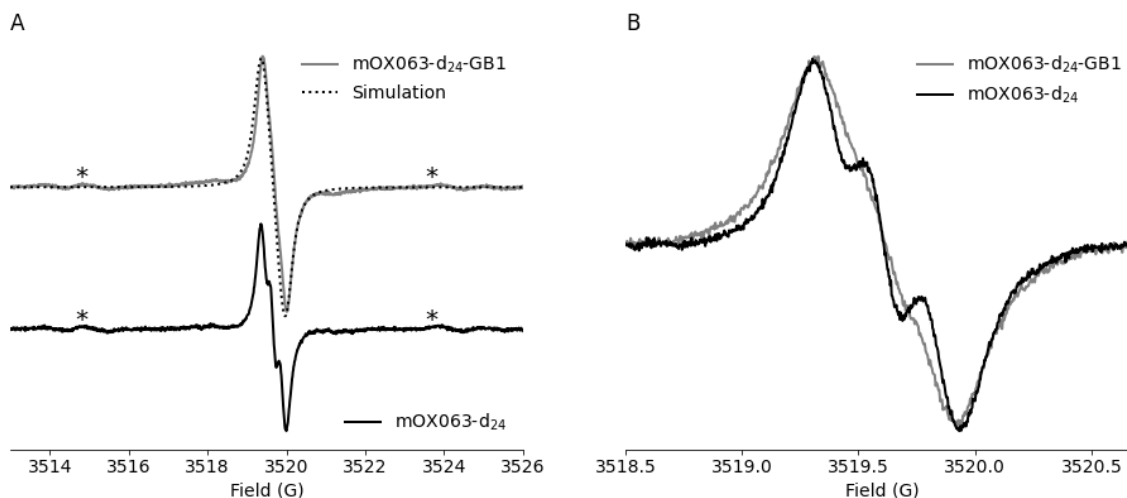


**Figure 3.** A) CW-ESR spectra of mOX063-d<sub>24</sub>-GB1 (top) and mOX063-d<sub>24</sub> (bottom). The spectrum of mOX063-d<sub>24</sub>-GB1 can be fitted with a narrow single-component simulation. The <sup>13</sup>C satellite peaks are marked with \*. B) The CW-ESR spectra of mOX063-d<sub>24</sub>-GB1 and mOX063-d<sub>24</sub> with the observation window ~2 G at the central lineshape. The nitrogen superhyperfine is partially resolved in the mOX063-d<sub>24</sub> spectrum but not in the mOX063-d<sub>24</sub>-GB1 spectrum. Reproduced from Hasanbasri, *JPC* 2021.

More importantly, the mOX063-d<sub>24</sub>-GB1 CW spectrum can be fitted with a narrow single-component simulation without a broad component, commonly seen when using FT<sup>74,75,78,92</sup>. FT's broad component has been attributed to aggregated species of FT<sup>76,77</sup> and non-specific binding in proteins<sup>75,76,79,93</sup> and membranes<sup>74</sup>. As a result, when using the simple spin-labeling workflow, FT had labeling efficiencies of 24% to 80% depending on the linker and protein<sup>67,78,79,92</sup>. On the other hand, mOX063-d<sub>24</sub> is highly soluble and does not bind non-specifically<sup>79</sup>. Therefore, the hydrophilicity of mOX063-d<sub>24</sub> allows ~100% labeling efficiency using simple protein labeling protocols. Additionally, the labeling efficiency of mOX063-d<sub>24</sub> is slightly improved from the previously developed hydrophilic trityl spin-label, Ox-SLIM, which reported to have 85% labeling efficiency<sup>80</sup>. Such differences in labeling efficiency could be due to the difference in maleimide linker length between mOX063-d<sub>24</sub> and Ox-SLIM, and potentially to the differences in solvent accessibilities between the two sites in the two proteins.

Next, pulsed-ESR was used to measure the relaxation times of GB1-bound mOX063-d<sub>24</sub> since these are critical parameters that dictate the efficacy of the label in pulsed dipolar spectroscopy. These data were acquired at a spin concentration of 5 μM and the sample was prepared in 20 mM PBS buffer at pH 7.4, and contained 20% glycerol. The phase-memory relaxation time ( $T_m$ ) was measured by echo decay experiments. The measured values of  $T_m$  are listed in Table 1 and the data is shown in Figure S4A. The  $T_m$  of GB1-bound mOX063-d<sub>24</sub> is 5.1 μs, 4.3 μs, or 3.6 μs at 80 K, 150 K, or 180 K, respectively. These relaxation measurements provided additional data points to the existing measurements from previous studies of OX063-based spin-labels (cf. Table S1). For comparison, the  $T_m$  value of 5.1 μs for GB1-bound mOX063-d<sub>24</sub> at 80 K is longer than the  $T_m$  value of 1.6 μs of protein-bound FT at 80 K<sup>78</sup>. The longest reported  $T_m$  of protein-bound FT is 2.9 μs at 50K<sup>79</sup>. Increasing the  $T_m$  can both increase the echo intensity for distance measurements and increase the range of feasible temperature of the experiment.

At higher temperatures, mOX063-d<sub>24</sub> also benefit from the shortening of  $T_1$ . GB1-bound mOX063-d<sub>24</sub> has  $T_1$  values of 1.98 ms, 0.175 ms, and 0.112 ms at 80 K, 150 K, and 180 K respectively (Table 1, Figure S4B and S4C). The mechanism for  $T_1$  relaxation of trityl radicals as a function of temperature has been previously studied<sup>94</sup>. As  $T_1$  gets shorter with increasing temperature, the amount of time required for GB1-bound mOX063-d<sub>24</sub> to completely relax becomes shorter leading to a faster rate of repeating the measurement. For comparison, the  $T_1$  value of 1.98 ms for GB1-bound mOX063-d<sub>24</sub> at 80 K listed in Table 1 is slightly longer than the  $T_1$  value of 1.7 ms of protein-bound FT at 80 K<sup>78</sup>. However, distance measurements using FT are typically done at 50 K or lower which has  $T_1$  values of 6.3 ms or longer<sup>78</sup>. Therefore, distance measurement using mOX063-d<sub>24</sub> at higher temperature leads to more scans per unit of time than the distance measurement using FT at the typical temperature of 50 K. Consequently, we expect that distance measurements using mOX063-d<sub>24</sub> at higher temperatures benefit from a shorter  $T_1$ .

**Table 1.**  $T_m$  and  $T_1$  measurements of mOX063-d<sub>24</sub>-GB1 at 80 K, 150 K, and 180 K.

Temperature	$T_m$	$T_1$
80 K	5.1 $\mu$ s	1.98 ms
150 K	4.3 $\mu$ s	0.175 ms
180 K	3.6 $\mu$ s	0.112 ms

Reproduced from Hasanbasri, *JPC* 2021.

To showcase the sensitivity of mOX063-d<sub>24</sub>, DQC experiments at 80 K or 150 K were performed on E15C/K28C GB1 doubly-labeled by mOX063-d<sub>24</sub> (dmOX063-d<sub>24</sub>-GB1), as shown in Figure 4A. The method to measure  $SNR$  is described in the methods section. The DQC time trace achieved sufficiently high  $SNR$  at 150 K within approximately 1.5 hours of runtime ( $SNR = 20 \text{ min}^{-1/2}$ ). On the other hand, at 80 K, even after 2 hours of runtime, the DQC time trace ( $SNR = 7 \text{ min}^{-1/2}$ ) is noisier than the 150 K DQC time trace. The higher  $SNR$  of 150 K DQC than the  $SNR$  of 80 K DQC can be rationalized by the following analysis of  $SNR$  for pulsed-ESR experiments<sup>95</sup>:

$$SNR(T) \propto \frac{1}{T} \exp[-t_{tot}/T_m(T)] \sqrt{\frac{1}{T_1(T)}} \text{ (Eq.1)}$$

where  $T$  is the temperature and  $t_{tot}$  is the amount of time the electron coherence evolves until the detection of the echo signal. The  $1/T$  term in Eq.1 is due to the Boltzmann factor<sup>96</sup>. Based on Eq.1, the shorter  $T_1 = 0.175 \text{ ms}$  at 150 K than the  $T_1 = 1.98 \text{ ms}$  at 80 K (Table 1, Figure S4B and S5C) contributes to 3.36 times improvement in  $SNR$ . On the other hand, the increase in temperature from 80 K to 150 K only led to a slight reduction of  $T_m$  from 5.1  $\mu$ s to 4.3  $\mu$ s. Furthermore, the increase in temperature causes a loss in echo intensity due to the reduction in spin-polarization. Based on Eq.1, the decrease in  $T_m$  and spin-polarization reduces the  $SNR$  by 0.43 times. As a result, the final  $SNR$  at 150 K is  $3.36 \times 0.43 = 1.44$  times higher than the  $SNR$  at 80 K. We can see the  $SNR$  improvement from the DQC echo comparison between 80 K and 150 K shown in Figure S5. Overall, the gain in sensitivity due to  $T_1$  was able to over-compensate the loss of echo intensity from the shortening of  $T_m$  and the reduction of spin-polarization. However, increasing the temperature further to 180 K causes the reduction in sensitivity due to reduced spin-polarization and  $T_m$ . For example, the sensitivity at 180 K is ~79% of the sensitivity at 150 K based on Eq.1. These comparisons signify the importance of experimentally evaluating the relaxation times at various temperatures, since the values can be different for different systems. While 80 K is not the most optimal temperature for mOX063-d<sub>24</sub> DQC, its  $SNR = 7 \text{ min}^{-1/2}$  is comparable to the reported FT's  $SNR$ <sup>78</sup> ranging from  $7 \text{ min}^{-1/2}$  to  $8.9 \text{ min}^{-1/2}$  at 50 K. These comparison of  $SNR$  exemplifies the sensitivity gained from performing mOX063-d<sub>24</sub> DQC experiments at the optimal temperature.

We analyzed the time traces using the DeerAnalysis2018<sup>87</sup> package and the Tikhonov Regularization method to extract the distance distributions shown in Figure 4B. Expectedly, at both temperatures, the distance distributions were close to identical, with the most probable distance of 3.6 nm. In order to predict the distance distribution, we built an *in silico* model using MTSSLWizard<sup>97</sup>. Since the mOX063-d<sub>24</sub> spin-label does not exist in the MTSSLWizard package, we first implemented the mOX063-d<sub>24</sub> model into the MTSSLWizard software. Details are provided in Figure S6. The model predicted that the most probable distance is 3.8 nm, as shown in Figure 4B, which is in reasonable agreement with the DQC results. Furthermore, the experimental results have

a standard deviation of  $\sim 0.6$  nm, which is on par with the standard deviation of  $\sim 0.8$  nm obtained using nitroxide on the same GB1 mutant<sup>85</sup>.

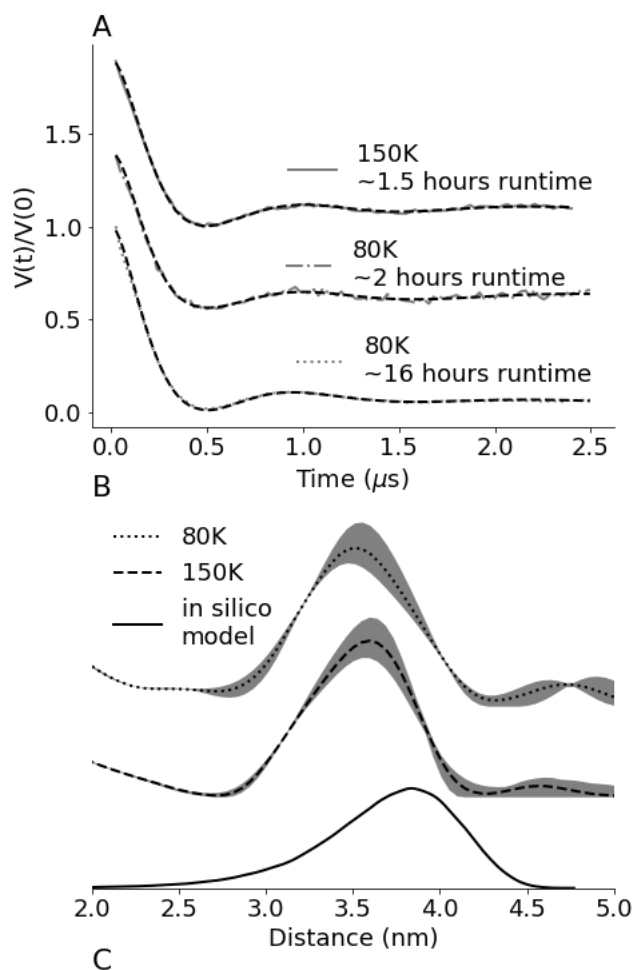


**Figure 4.** A) DQC time traces of doubly-labeled dmOX063-d<sub>24</sub>-GB1 at 150 K after 1.5 hours of runtime and at 80 K after 2 hours and 16 hours of runtime. B) Distance distributions obtained from the 150 K and 80 K DQC time traces using DeerAnalysis. The gray regions represent the error obtained from the validation function in DeerAnalysis. Additionally, a distance distribution was also obtained from *in silico* modeling using MTSSLWizard. C) *In silico* model from MTSSLWizard using GB1 (PDB:2QMT) and mOX063-d<sub>24</sub>. The two clusters represent the space occupied by the radical carbon. Reproduced from Hasanbasri, *JPC* 2021.

After the *in vitro* experiments, the viability of mOX063-d<sub>24</sub> for *in-cell* experiments was explored. Specifically, the dmOX063-d<sub>24</sub>-GB1 (200  $\mu\text{M}$  of spins) was subjected to either ten times excess of ascorbic acid or the cytosol extract of *Xenopus laevis* (African Bullfrog) oocytes. Cytosol was extracted from oocytes using previously published protocol<sup>85</sup>. The signal intensity of mOX063-d<sub>24</sub> was monitored over time using CW ESR, and the maximum intensity of each CW was plotted against time in Figure 5A. The signal intensity decays to about 97 and 95% of its original intensity in ascorbate and cytosol after 5 hours, respectively. The stability of mOX063-d<sub>24</sub>

is on par with the stability of other trityls<sup>73,80</sup>. The signal persistence of mOX063-d<sub>24</sub> showcases the reduction-resistance of mOX063-d<sub>24</sub> against the cytosolic antioxidants that play a role in reducing radicals *in-cell*<sup>98</sup>.

After measuring mOX063-d<sub>24</sub> stability, dmOX063-d<sub>24</sub>-GB1 was injected into oocytes and incubated for 30 minutes after injection before flash-freezing the sample. The 30 minutes incubation allows for dmOX063-d<sub>24</sub>-GB1 to completely diffuse in oocytes<sup>48</sup>. Echo decay experiment measured the  $T_m$  of mOX063-d<sub>24</sub> at 80 K in oocytes to be 4.3  $\mu$ s as shown in Figure S7, which is shorter than the  $T_m$  of mOX063-d<sub>24</sub> *in vitro* shown in Table 1 and Figure S4A. The lower GB1-bound mOX063-d<sub>24</sub>  $T_m$  *in-cell* compared to *in vitro* was expected because of the crowded environment *in-cell*. The crowded environment can lead to an increase in the local concentration of protons near the radical which enhances the contribution of electron-nuclei interactions to relaxation. In addition, the presence of paramagnetic metal ions, primarily Mn(II)<sup>99</sup>, in the cell can enhance relaxation. However, the  $T_m$  of mOX063-d<sub>24</sub> in oocytes is surprising since previous reports of other organic spin-labels used *in-cell* (nitroxides<sup>50,57,100</sup> and FT<sup>67,72,73</sup>) have  $T_m$  values in the range of 0.6-2  $\mu$ s. Therefore, mOX063-d<sub>24</sub> also improves the sensitivity of distance measurements *in-cell* due to the  $T_m$  that is at least 2 times longer than previously published  $T_m$  of nitroxide or FT *in-cell*.

Distance measurements of dmOX063-d<sub>24</sub>-GB1 in oocytes were done using DQC at 80 K shown in Figure 5B. We observed an artifact that overlaps the desired DQC signal at zero time. Such an artifact has been seen previously and attributed to trityl dimers and to partial labeling of non-cysteines residues such as lysine<sup>101</sup>. We repeated the labeling procedure on WT GB1 that has no cysteine residues. After concentrating the sample, UV-Vis indicates no presence of mOX063-d<sub>24</sub> as shown in Figure S8. We expected this result since our previous work using GB1 and maleimide-linked nitroxide (5-MSL) did not show over-labeling of the protein<sup>85</sup>. In addition, we did not see an ESR signal from the WT GB1 sample which also excludes the presence of dimers.

We attribute this artifact as due the formation of a small echo generated by the first and the fourth pulses in the DQC 6-pulse sequence. This interference can be readily seen in the 2D contour plot of the DQC signal shown in Figure S9A. As a result, the DQC time trace contained an artifact shown as a sharp feature at the  $t = 0$  shown in Figure S9B, which led to improper fitting of the time trace. Additionally, the artifact contributed to a short distance around 2 nm shown in Figure S10A. The artifact seemed to be a result of inefficient phase-cycling in our DQC experiment and is evident in the *in-cell* data due to the lower SNR.

To support this hypothesis, we performed the DQC experiment using the same parameters on 300  $\mu$ M TEMPOL as shown in Figure S11. The same artifact was seen crossing the desired DQC echo at a slanted angle shown in the 2D contour plot in figure S11A. As a result, a sharp feature at  $t=0$  manifested as shown in Figure S11B. The artifact was more prominent in the *in-cell* experiment than in the *in vitro* experiment for two reasons. First, the measured echo in the *in-cell* DQC was half as intense as the measured echo in the *in vitro* DQC. The lower *in-cell* echo intensity is due to the shorter  $T_m$  *in-cell* than the  $T_m$  *in vitro*. Additionally, reduction of mOX063-d<sub>24</sub> can still occur due to the contribution of oocytes' membrane-associated factors<sup>85</sup> such as thioredoxin<sup>102</sup> and glutathione reductase<sup>103</sup>, which are not accounted for in our cytosol stability measurement. These two contributions led to a less intense measured echo causing the artifact to be prominent in the *in-cell* DQC.

To remove the artifact in the DQC time trace in oocytes, DQC was performed on a sample of free mOX063-d<sub>24</sub>, which contained only the artifact shown in Figure S9B. The free mOX063-d<sub>24</sub> DQC time trace was used to subtract the artifact from the time trace of dmOX063-d<sub>24</sub>-GB1 in oocytes shown in Figure 5B. The artifact-subtracted time trace was used to extract the distance distribution shown Figure 5C, which agrees quite well with the *in vitro* distance measurements in Figure 4B. Furthermore, we were able to repeat the *in-cell* DQC experiment at 150 K, shown in Figure S12, and obtain a similar distribution as the 80 K *in-cell* distribution. Additionally, we repeated our *in-cell* experiments at 80 K using a different batch of oocytes and newly overexpressed and labeled-GB1 to ensure that the *in-cell* results are reproducible. This data is shown in Figure S13. Overall, we obtained a highly sensitive distance measurement in oocytes using mOX063-d<sub>24</sub>.

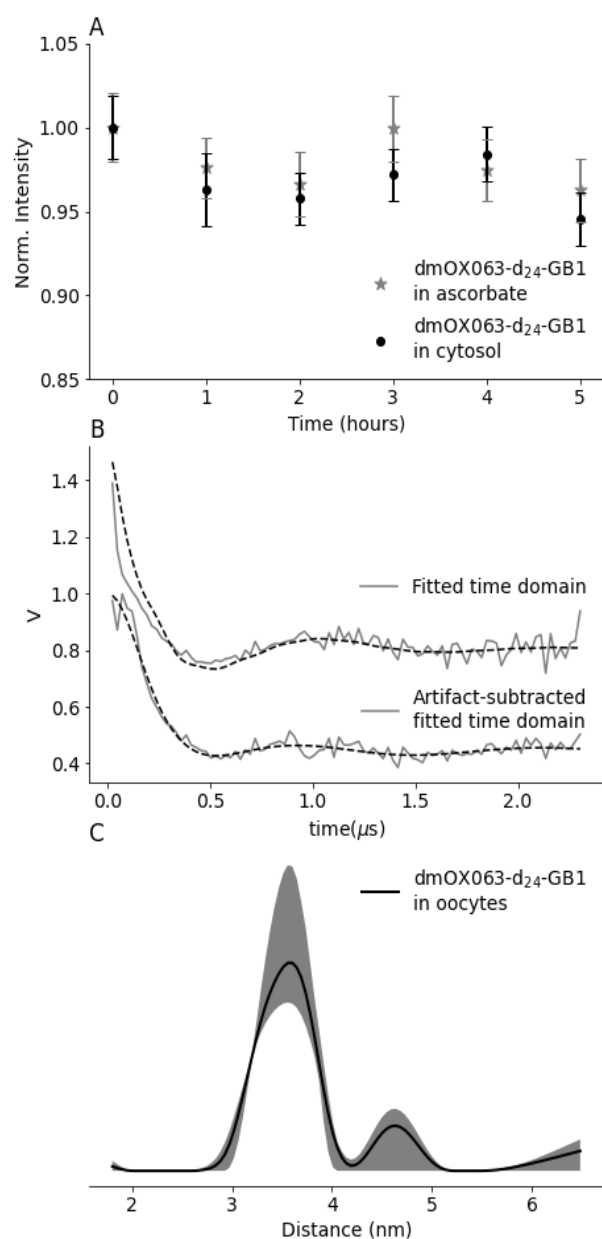


**Figure 5.** A) A plot of the maximum intensity of dmOX063-d<sub>24</sub>-GB1 vs. time in 10 times excess of ascorbate or cytosol extracted from *Xenopus laevis* oocytes. The height of the vertical bars represents the RMSD in the CW spectrum. B) DQC time trace of dmOX063-d<sub>24</sub>-GB1 at 80 K Q-band before and after artifact subtraction. C) Distance distribution (most probable distance of 3.6 nm) extracted from the artifact-subtracted time-domain signal using DeerAnalysis. The gray region represents the error obtained from the validation function. Reproduced from Hasanbasri. *JPC* 2021.

## Conclusions

In conclusion, this work showed that mOX063-d<sub>24</sub> has a high protein-labeling efficiency of ~97%. Furthermore, we showed that *in vitro* distance measurements of mOX063-d<sub>24</sub> is more sensitive at higher temperatures. Finally, we obtained distance measurements using mOX063-d<sub>24</sub> *in-cell* which agree with *in silico* modeling. This work adds to the library of spin labels that can be used for *in-cell* work. In particular, mOX063-d<sub>24</sub> is similar to Ox-SLIM<sup>80</sup> since both are hydrophilic spin-labels with a maleimide linker, as shown in Figure 1A. However, these two spin-labels differ in their trityl cores and linker lengths. These differences provide variation in the labeling efficiency,  $T_m$ , and breadth of distance distribution. In one case, Ox-SLIM's short linker length can provide narrow distance distributions that can readily resolve different protein conformations<sup>73,80</sup>. On the other hand, mOX063-d<sub>24</sub> provides longer  $T_m$  and higher labeling efficiency leading to the sensitivity improvement in the distance measurements. Overall, Ox-SLIM and mOX063-d<sub>24</sub> are complementary to each other due to their differences.

## Supporting Information

HRMS-ESI data of mOX063-d<sub>24</sub> and mOX063-d<sub>24</sub>-GB1, UV-Vis of mOX063-d<sub>24</sub> + WT GB1, pulsed-ESR relaxation measurements, details of MtsslWizard modeling, comparison of *in vitro* DQC echo of dmOX063-d<sub>24</sub>-GB1 at 80 K and 150 K, raw 1D and 2D DQC time domains, *in-cell* DQC data at 150 K and 80 K (second trial).

## Acknowledgments

This work was partially supported by the NIH grants (USA) R00EB023990, R21EB028553-01A1, and NSF-BSF MCB 2001654. Z.H. acknowledges fellowship support from NIH T32 GM 88119-9. The content is solely the responsibility of the authors and does not necessarily represent the official views of the NIH. We acknowledge use of the WVU Shared Research Facilities

## References

- (1) Dhar, A.; Girdhar, K.; Singh, D.; Gelman, H.; Ebbinghaus, S.; Gruebele, M. Protein stability and folding kinetics in the nucleus and endoplasmic reticulum of eucaryotic cells. *Biophys. J.* **2011**, *101*, 421–430.
- (2) Ignatova, Z.; Krishnan, B.; Bombardier, J. P.; Marcelino, A. M. C.; Hong, J.; Gierasch, L. M. From the test tube to the cell: exploring the folding and aggregation of a beta-clam protein. *Biopolymers* **2007**, *88*, 157–163.
- (3) Cheung, M. S.; Gasic, A. G. Towards developing principles of protein folding and dynamics in the cell. *Phys. Biol.* **2018**, *15*, 063001.
- (4) Timr, S.; Madern, D.; Sterpone, F. Protein thermal stability. *Prog Mol Biol Transl Sci* **2020**, *170*, 239–272.
- (5) Sukenik, S.; Salam, M.; Wang, Y.; Gruebele, M. In-Cell Titration of Small Solutes Controls Protein Stability and Aggregation. *J. Am. Chem. Soc.* **2018**, *140*, 10497–10503.
- (6) Silverstein, T. P.; Slade, K. Effects of macromolecular crowding on biochemical systems. *J. Chem. Educ.* **2019**, *96*(11), 2476–2487.
- (7) Gao, M.; Held, C.; Patra, S.; Arns, L.; Sadowski, G.; Winter, R. Crowders and Cosolvents-Major Contributors to the Cellular Milieu and Efficient Means to Counteract Environmental Stresses. *ChemPhysChem* **2017**, *18*, 2951–2972.
- (8) Feng, R.; Gruebele, M.; Davis, C. M. Quantifying protein dynamics and stability in a living organism. *Nat. Commun.* **2019**, *10*, 1179.
- (9) König, I.; Zarrine-Afsar, A.; Aznauryan, M.; Soranno, A.; Wunderlich, B.; Dingfelder, F.; Stüber, J. C.; Plückthun, A.; Nettels, D.; Schuler, B. Single-molecule spectroscopy of protein conformational dynamics in live eukaryotic cells. *Nat. Methods* **2015**, *12*, 773–779.
- (10) Senske, M.; Törk, L.; Born, B.; Havenith, M.; Herrmann, C.; Ebbinghaus, S. Protein stabilization by macromolecular crowding through enthalpy rather than entropy. *J. Am. Chem. Soc.* **2014**, *136*, 9036–9041.
- (11) Shahid, S.; Ahmad, F.; Hassan, M. I.; Islam, A. Relationship between protein stability and functional activity in the presence of macromolecular crowding agents alone and in mixture: An insight into stability-activity trade-off. *Arch. Biochem. Biophys.* **2015**, *584*, 42–50.
- (12) Cook, E. C.; Creamer, T. P. Calcineurin in a crowded world. *Biochemistry* **2016**, *55*, 3092–3101.
- (13) Yang, Y.; Chen, S.-N.; Yang, F.; Li, X.-Y.; Feintuch, A.; Su, X.-C.; Goldfarb, D. In-cell destabilization of a homodimeric protein complex detected by DEER spectroscopy. *Proc. Natl. Acad. Sci. USA* **2020**, *117*, 20566–20575.
- (14) Guseman, A. J.; Perez Goncalves, G. M.; Speer, S. L.; Young, G. B.; Pielak, G. J. Protein shape modulates crowding effects. *Proc. Natl. Acad. Sci. USA* **2018**, *115*, 10965–10970.
- (15) Berg, O. G. The influence of macromolecular crowding on thermodynamic activity: solubility and dimerization constants for spherical and dumbbell-shaped molecules in a hard-sphere mixture. *Biopolymers* **1990**, *30*, 1027–1037.
- (16) Goldfarb, D. Gd<sup>3+</sup> spin labeling for distance measurements by pulse EPR spectroscopy. *Phys. Chem. Chem. Phys.* **2014**, *16*, 9685–9699.
- (17) Hubbell, W. L.; López, C. J.; Altenbach, C.; Yang, Z. Technological advances in site-directed spin labeling of proteins. *Curr. Opin. Struct. Biol.* **2013**, *23*, 725–733.
- (18) Roser, P.; Schmidt, M. J.; Drescher, M.; Summerer, D. Site-directed spin labeling of proteins for distance measurements in vitro and in cells. *Org. Biomol. Chem.* **2016**, *14*, 5468–5476.
- (19) Gamble Jarvi, A.; Bogetti, X.; Singewald, K.; Ghosh, S.; Saxena, S. Going the dHis-tance: Site-Directed Cu<sup>2+</sup> Labeling of Proteins and Nucleic Acids. *Acc. Chem. Res.* **2021**, *54*, 1481–1491.
- (20) Singewald, K.; Bogetti, X.; Sinha, K.; Rule, G. S.; Saxena, S. Double Histidine Based EPR Measurements at Physiological Temperatures Permit Site-Specific Elucidation of Hidden Dynamics in Enzymes. *Angew. Chem. Int. Ed. Engl.* **2020**, *59*, 23040–23044.
- (21) Altenbach, C.; López, C. J.; Hideg, K.; Hubbell, W. L. Exploring Structure, Dynamics, and Topology of Nitroxide Spin-Labeled Proteins Using Continuous-Wave Electron Paramagnetic Resonance Spectroscopy. *Meth. Enzymol.* **2015**, *564*, 59–100.
- (22) Saxena, S.; Freed, J. H. Theory of double quantum two-dimensional electron spin resonance with application to distance measurements. *J. Chem. Phys.* **1997**, *107*, 1317–1340.
- (23) Borbat, P. P.; Freed, J. H. Multiple-quantum ESR and distance measurements. *Chem. Phys. Lett.* **1999**, *313*, 145–154.
- (24) Milov, A. D.; Maryasov, A. G.; Tsvetkov, Y. D. Pulsed electron double resonance (PELDOR) and its applications in free-radicals research. *Appl Magn Reson* **1998**, *15*, 107–143.
- (25) Pannier, M.; Veit, S.; Godt, A.; Jeschke, G.; Spiess, H. W. Dead-time free measurement of dipole-dipole interactions between electron spins. *J. Magn. Reson.* **2000**, *142*, 331–340.
- (26) Jeschke, G.; Pannier, M.; Godt, A.; Spiess, H. W. Dipolar spectroscopy and spin alignment in electron paramagnetic resonance. *Chem. Phys. Lett.* **2000**, *331*, 243–252.
- (27) Kulik, L. V.; Dzuba, S. A.; Grigoryev, I. A.; Tsvetkov, Y. D. Electron dipole-dipole interaction in ESEEM of nitroxide biradicals. *Chem. Phys. Lett.* **2001**, *343*, 315–324.

- (28) Milikisyants, S.; Scarpelli, F.; Finiguerra, M. G.; Ubbink, M.; Huber, M. A pulsed EPR method to determine distances between paramagnetic centers with strong spectral anisotropy and radicals: the dead-time free RIDME sequence. *J. Magn. Reson.* **2009**, *201*, 48–56.
- (29) Assafa, T. E.; Anders, K.; Linne, U.; Essen, L.-O.; Bordignon, E. Light-Driven Domain Mechanics of a Minimal Phytochrome Photoreceptor Module Studied by EPR. *Structure* **2018**, *26*, 1534–1545.e4.
- (30) Liu, Z.; Casey, T. M.; Blackburn, M. E.; Huang, X.; Pham, L.; de Vera, I. M. S.; Carter, J. D.; Kear-Scott, J. L.; Veloro, A. M.; Galiano, L.; et al. Pulsed EPR characterization of HIV-1 protease conformational sampling and inhibitor-induced population shifts. *Phys. Chem. Chem. Phys.* **2016**, *18*, 5819–5831.
- (31) Grytz, C. M.; Marko, A.; Cekan, P.; Sigurdsson, S. T.; Prisner, T. F. Flexibility and conformation of the cocaine aptamer studied by PELDOR. *Phys. Chem. Chem. Phys.* **2016**, *18*, 2993–3002.
- (32) Hänel, I.; Wunnicke, D.; Bordignon, E.; Steinhoff, H.-J.; Slotboom, D. J. Conformational heterogeneity of the aspartate transporter Glt(Ph). *Nat. Struct. Mol. Biol.* **2013**, *20*, 210–214.
- (33) Dalmas, O.; Sompornpisut, P.; Bezanilla, F.; Perozo, E. Molecular mechanism of Mg<sup>2+</sup>-dependent gating in CorA. *Nat. Commun.* **2014**, *5*, 3590.
- (34) Verhalen, B.; Dastvan, R.; Thangapandian, S.; Peskova, Y.; Koteiche, H. A.; Nakamoto, R. K.; Tajkhorshid, E.; Mchaourab, H. S. Energy transduction and alternating access of the mammalian ABC transporter P-glycoprotein. *Nature* **2017**, *543*, 738–741.
- (35) Dawidowski, D.; Cafiso, D. S. Munc18-1 and the Syntaxin-1 N Terminus Regulate Open-Closed States in a t-SNARE Complex. *Structure* **2016**, *24*, 392–400.
- (36) Sameach, H.; Ghosh, S.; Gevorkyan-Airapetov, L.; Saxena, S.; Ruthstein, S. EPR spectroscopy detects various active state conformations of the transcriptional regulator c-Myb. *Angew. Chem. Int. Ed. Engl.* **2019**, *58*, 3053–3056.
- (37) Stone, K.; Townsend, J.; Sarver, J.; Sapienza, P.; Saxena, S.; Jen-Jacobson, L. Electron Spin Resonance Shows Common Structural Features for Different Classes of Eco RI-DNA Complexes. *Angew. Chem. Int. Ed. Engl.* **2008**, *120*, 10346–10348.
- (38) Milikisyants, S.; Wang, S.; Munro, R. A.; Donohue, M.; Ward, M. E.; Bolton, D.; Brown, L. S.; Smirnova, T. I.; Ladizhansky, V.; Smirnov, A. I. Oligomeric Structure of Anabaena Sensory Rhodopsin in a Lipid Bilayer Environment by Combining Solid-State NMR and Long-range DEER Constraints. *J. Mol. Biol.* **2017**, *429*, 1903–1920.
- (39) Park, S.-Y.; Borbat, P. P.; Gonzalez-Bonet, G.; Bhatnagar, J.; Pollard, A. M.; Freed, J. H.; Bilwes, A. M.; Crane, B. R. Reconstruction of the chemotaxis receptor-kinase assembly. *Nat. Struct. Mol. Biol.* **2006**, *13*, 400–407.
- (40) Valera, S.; Ackermann, K.; Pliotas, C.; Huang, H.; Naismith, J. H.; Bode, B. E. Accurate extraction of nanometer distances in multimers by pulse EPR. *Chem. Eur. J* **2016**, *22*, 4700–4703.
- (41) DeBerg, H. A.; Bankston, J. R.; Rosenbaum, J. C.; Brzovic, P. S.; Zagotta, W. N.; Stoll, S. Structural mechanism for the regulation of HCN ion channels by the accessory protein TRIP8b. *Structure* **2015**, *23*, 734–744.
- (42) Upadhyay, A. K.; Borbat, P. P.; Wang, J.; Freed, J. H.; Edmondson, D. E. Determination of the oligomeric states of human and rat monoamine oxidases in the outer mitochondrial membrane and octyl beta-D-glucopyranoside micelles using pulsed dipolar electron spin resonance spectroscopy. *Biochemistry* **2008**, *47*, 1554–1566.
- (43) Yin, D. M.; Hannam, J. S.; Schmitz, A.; Schiemann, O.; Hagelueken, G.; Famulok, M. Studying the Conformation of a Receptor Tyrosine Kinase in Solution by Inhibitor-Based Spin Labeling. *Angew. Chem. Int. Ed. Engl.* **2017**, *56*, 8417–8421.
- (44) Gamble Jarvi, A.; Cunningham, T. F.; Saxena, S. Efficient localization of a native metal ion within a protein by Cu<sup>2+</sup>-based EPR distance measurements. *Phys. Chem. Chem. Phys.* **2019**, *21*, 10238–10243.
- (45) Abdullin, D.; Florin, N.; Hagelueken, G.; Schiemann, O. EPR-based approach for the localization of paramagnetic metal ions in biomolecules. *Angew. Chem. Int. Ed. Engl.* **2015**, *54*, 1827–1831.
- (46) Ketter, S.; Gopinath, A.; Rogozhnikova, O.; Trukhin, D.; Tormyshev, V. M.; Bagryanskaya, E. G.; Joseph, B. In Situ Labeling and Distance Measurements of Membrane Proteins in E. coli Using Finland and OX063 Trityl Labels. *Chem. Eur. J* **2021**, *27*, 2299–2304.
- (47) Igarashi, R.; Sakai, T.; Hara, H.; Tenno, T.; Tanaka, T.; Tochio, H.; Shirakawa, M. Distance determination in proteins inside *Xenopus laevis* oocytes by double electron-electron resonance experiments. *J. Am. Chem. Soc.* **2010**, *132*, 8228–8229.
- (48) Lawless, M. J.; Shimshi, A.; Cunningham, T. F.; Kinde, M. N.; Tang, P.; Saxena, S. Analysis of Nitroxide-Based Distance Measurements in Cell Extracts and in Cells by Pulsed ESR Spectroscopy. *ChemPhysChem* **2017**, *18*, 1653–1660.
- (49) Wojciechowski, F.; Groß, A.; Holder, I. T.; Knörr, L.; Drescher, M.; Hartig, J. S. Pulsed EPR spectroscopy distance measurements of DNA internally labelled with Gd(3+)-DOTA. *Chem. Commun.* **2015**, *51*, 13850–13853.
- (50) Krstić, I.; Hänsel, R.; Romainczyk, O.; Engels, J. W.; Dötsch, V.; Prisner, T. F. Long-range distance measurements on nucleic acids in cells by pulsed EPR spectroscopy. *Angew. Chem. Int. Ed. Engl.* **2011**, *50*, 5070–5074.
- (51) Azarkh, M.; Okle, O.; Eyring, P.; Dietrich, D. R.; Drescher, M. Evaluation of spin labels for in-cell EPR by analysis of nitroxide reduction in cell extract of *Xenopus laevis* oocytes. *J. Magn. Reson.* **2011**, *212*, 450–454.
- (52) Schmidt, M. J.; Fedoseev, A.; Bucker, D.; Borbas, J.; Peter, C.; Drescher, M.; Summerer, D. EPR Distance Measurements in Native Proteins with Genetically Encoded Spin Labels. *ACS Chem. Biol.* **2015**, *10*, 2764–2771.
- (53) Fleissner, M. R.; Brustad, E. M.; Kálai, T.; Altenbach, C.; Cascio, D.; Peters, F. B.; Hideg, K.; Peuker, S.; Schultz, P. G.; Hubbell, W. L. Site-directed spin labeling of a genetically encoded unnatural amino acid. *Proc. Natl. Acad. Sci. USA* **2009**, *106*, 21637–21642.
- (54) Mascali, F. C.; Ching, H. Y. V.; Rasia, R. M.; Un, S.; Tabares, L. C. Using Genetically Encodable Self-Assembling Gd(III) Spin Labels To Make In-Cell Nanometric Distance Measurements. *Angew. Chem. Int. Ed. Engl.* **2016**, *55*, 11041–11043.
- (55) Kucher, S.; Korneev, S.; Tyagi, S.; Apfelbaum, R.; Grohmann, D.; Lemke, E. A.; Klare, J. P.; Steinhoff, H.-J.; Klose, D. Orthogonal spin labeling using click chemistry for in vitro and in vivo applications. *J. Magn. Reson.* **2017**, *275*, 38–45.
- (56) Kugele, A.; Silkenath, B.; Langer, J.; Wittmann, V.; Drescher, M. Protein Spin Labeling with a Photocaged Nitroxide Using Diels-Alder Chemistry. *ChemBiochem* **2019**, *20*, 2479–2484.
- (57) Karthikeyan, G.; Bonucci, A.; Casano, G.; Gerbaud, G.; Abel, S.; Thomé, V.; Kodjabachian, L.; Magalon, A.; Guigliarelli, B.; Belle, V.; et al. A Bioresistant Nitroxide Spin Label for In-Cell EPR Spectroscopy: In Vitro and In Oocytes Protein Structural Dynamics Studies. *Angew. Chem. Int. Ed. Engl.* **2018**, *57*, 1366–1370.
- (58) Paletta, J. T.; Pink, M.; Foley, B.; Rajca, S.; Rajca, A. Synthesis and reduction kinetics of sterically shielded pyrrolidine nitroxides. *Org. Lett.* **2012**, *14*, 5322–5325.

- (59) Qi, M.; Gross, A.; Jeschke, G.; Godt, A.; Drescher, M. Gd(III)-PyMTA label is suitable for in-cell EPR. *J. Am. Chem. Soc.* **2014**, *136*, 15366–15378.
- (60) Martorana, A.; Bellapadrona, G.; Feintuch, A.; Di Gregorio, E.; Aime, S.; Goldfarb, D. Probing protein conformation in cells by EPR distance measurements using Gd<sup>3+</sup> spin labeling. *J. Am. Chem. Soc.* **2014**, *136*, 13458–13465.
- (61) Thonon, D.; Jacques, V.; Desreux, J. F. A gadolinium triacetic monoamide DOTA derivative with a methanethiosulfonate anchor group. Relaxivity properties and conjugation with albumin and thiolated particles. *Contrast Media Mol. Imaging* **2007**, *2*, 24–34.
- (62) Shevelev, G. Y.; Krumkacheva, O. A.; Lomzov, A. A.; Kuzhelev, A. A.; Trukhin, D. V.; Rogozhnikova, O. Y.; Tormyshev, V. M.; Pyshnyi, D. V.; Fedin, M. V.; Bagryanskaya, E. G. Triarylmethyl labels: toward improving the accuracy of EPR nanoscale distance measurements in dnas. *J. Phys. Chem. B* **2015**, *119*, 13641–13648.
- (63) Yang, Z.; Liu, Y.; Borbat, P.; Zweier, J. L.; Freed, J. H.; Hubbell, W. L. Pulsed ESR dipolar spectroscopy for distance measurements in immobilized spin labeled proteins in liquid solution. *J. Am. Chem. Soc.* **2012**, *134*, 9950–9952.
- (64) Reginsson, G. W.; Kunjir, N. C.; Sigurdsson, S. T.; Schiemann, O. Trityl radicals: spin labels for nanometer-distance measurements. *Chem. Eur. J* **2012**, *18*, 13580–13584.
- (65) Dhimitruka, I.; Bobko, A. A.; Eubank, T. D.; Komarov, D. A.; Khramtsov, V. V. Phosphonated trityl probes for concurrent in vivo tissue oxygen and pH monitoring using electron paramagnetic resonance-based techniques. *J. Am. Chem. Soc.* **2013**, *135*, 5904–5910.
- (66) Liu, W.; Nie, J.; Tan, X.; Liu, H.; Yu, N.; Han, G.; Zhu, Y.; Villamena, F. A.; Song, Y.; Zweier, J. L.; et al. Synthesis and characterization of pegylated trityl radicals: effect of pegylation on physicochemical properties. *J. Org. Chem.* **2017**, *82*, 588–596.
- (67) Jassoy, J. J.; Berndhäuser, A.; Duthie, F.; Kühn, S. P.; Hagelueken, G.; Schiemann, O. Versatile Trityl Spin Labels for Nanometer Distance Measurements on Biomolecules In Vitro and within Cells. *Angew. Chem. Int. Ed. Engl.* **2017**, *56*, 177–181.
- (68) Owenius, R.; Eaton, G. R.; Eaton, S. S. Frequency (250 MHz to 9.2 GHz) and viscosity dependence of electron spin relaxation of triarylmethyl radicals at room temperature. *J. Magn. Reson.* **2005**, *172*, 168–175.
- (69) Khramtsov, V. V.; Bobko, A. A.; Tseytlin, M.; Driesschaert, B. Exchange phenomena in the electron paramagnetic resonance spectra of the nitroxyl and trityl radicals: multifunctional spectroscopy and imaging of local chemical microenvironment. *Anal. Chem.* **2017**, *89*, 4758–4771.
- (70) Yang, Z.; Bridges, M. D.; López, C. J.; Rogozhnikova, O. Y.; Trukhin, D. V.; Brooks, E. K.; Tormyshev, V.; Halpern, H. J.; Hubbell, W. L. A triarylmethyl spin label for long-range distance measurement at physiological temperatures using T1 relaxation enhancement. *J. Magn. Reson.* **2016**, *269*, 50–54.
- (71) Kuzhelev, A. A.; Krumkacheva, O. A.; Shevelev, G. Y.; Yulikov, M.; Fedin, M. V.; Bagryanskaya, E. G. Room-temperature distance measurements using RIDME and the orthogonal spin labels trityl/nitroxide. *Phys. Chem. Chem. Phys.* **2018**, *20*, 10224–10230.
- (72) Yang, Y.; Pan, B.-B.; Tan, X.; Yang, F.; Liu, Y.; Su, X.-C.; Goldfarb, D. In-Cell Trityl-Trityl Distance Measurements on Proteins. *J. Phys. Chem. Lett.* **2020**, *11*, 1141–1147.
- (73) Fleck, N.; Heubach, C. A.; Hett, T.; Haege, F. R.; Bawol, P. P.; Baltruschat, H.; Schiemann, O. SLIM: A Short-Linked, Highly Redox-Stable Trityl Label for High-Sensitivity In-Cell EPR Distance Measurements. *Angew. Chem. Int. Ed. Engl.* **2020**, *59*, 9767–9772.
- (74) Joseph, B.; Tormyshev, V. M.; Rogozhnikova, O. Y.; Akhmetzyanov, D.; Bagryanskaya, E. G.; Prisner, T. F. Selective High-Resolution Detection of Membrane Protein-Ligand Interaction in Native Membranes Using Trityl-Nitroxide PELDOR. *Angew. Chem. Int. Ed. Engl.* **2016**, *55*, 11538–11542.
- (75) Song, Y.; Liu, Y.; Liu, W.; Villamena, F. A.; Zweier, J. L. Characterization of the Binding of the Finland Trityl Radical with Bovine Serum Albumin. *RSC Adv.* **2014**, *4*, 47649–47656.
- (76) Dhimitruka, I.; Velayutham, M.; Bobko, A. A.; Khramtsov, V. V.; Villamena, F. A.; Hadad, C. M.; Zweier, J. L. Large-scale synthesis of a persistent trityl radical for use in biomedical EPR applications and imaging. *Bioorg. Med. Chem. Lett.* **2007**, *17*, 6801–6805.
- (77) Marin-Montesinos, I.; Paniagua, J. C.; Peman, A.; Vilaseca, M.; Luis, F.; Van Doorslaer, S.; Pons, M. Paramagnetic spherical nanoparticles by the self-assembly of persistent trityl radicals. *Phys. Chem. Chem. Phys.* **2016**, *18*, 3151–3158.
- (78) Jassoy, J. J.; Heubach, C. A.; Hett, T.; Bernhard, F.; Haege, F. R.; Hagelueken, G.; Schiemann, O. Site Selective and Efficient Spin Labeling of Proteins with a Maleimide-Functionalized Trityl Radical for Pulsed Dipolar EPR Spectroscopy. *Molecules* **2019**, *24*.
- (79) Tormyshev, V. M.; Chubarov, A. S.; Krumkacheva, O. A.; Trukhin, D. V.; Rogozhnikova, O. Y.; Spitsyna, A. S.; Kuzhelev, A. A.; Koval, V. V.; Fedin, M. V.; Godovikova, T. S.; et al. Methanethiosulfonate Derivative of OX063 Trityl: A Promising and Efficient Reagent for Side-Directed Spin Labeling of Proteins. *Chem. Eur. J* **2020**, *26*, 2705–2712.
- (80) Fleck, N.; Heubach, C.; Hett, T.; Spicher, S.; Grimme, S.; Schiemann, O. Ox-SLIM: Synthesis of and Site-Specific Labelling with a Highly Hydrophilic Trityl Spin Label. *Chem. Eur. J* **2021**, *27*, 5292–5297.
- (81) Girvin, M. E.; Fillingame, R. H. Determination of local protein structure by spin label difference 2D NMR: the region neighboring Asp61 of subunit c of the F1F0 ATP synthase. *Biochemistry* **1995**, *34*, 1635–1645.
- (82) Gronenborn, A. M.; Filipula, D. R.; Essig, N. Z.; Achari, A.; Whitlow, M.; Wingfield, P. T.; Clore, G. M. A novel, highly stable fold of the immunoglobulin binding domain of streptococcal protein G. *Science* **1991**, *253*, 657–661.
- (83) Poncelet, M.; Huffman, J. L.; Khramtsov, V. V.; Dhimitruka, I.; Driesschaert, B. Synthesis of hydroxyethyl tetrathiarylmethyl radicals OX063 and OX071. *RSC Adv.* **2019**, *9*, 35073–35076.
- (84) Cunningham, T. F.; McGoff, M. S.; Sengupta, I.; Jaroniec, C. P.; Horne, W. S.; Saxena, S. High-resolution structure of a protein spin-label in a solvent-exposed  $\beta$ -sheet and comparison with DEER spectroscopy. *Biochemistry* **2012**, *51*, 6350–6359.
- (85) Singewald, K.; Lawless, M. J.; Saxena, S. Increasing nitroxide lifetime in cells to enable in-cell protein structure and dynamics measurements by electron spin resonance spectroscopy. *J. Magn. Reson.* **2019**, *299*, 21–27.
- (86) Saxena, S.; Freed, J. H. Double quantum two-dimensional Fourier transform electron spin resonance: Distance measurements. *Chem. Phys. Lett.* **1996**, *251*, 102–110.

- (87) Jeschke, G.; Chechik, V.; Ionita, P.; Godt, A.; Zimmermann, H.; Banham, J.; Timmel, C. R.; Hilger, D.; Jung, H. DeerAnalysis2006—a comprehensive software package for analyzing pulsed ELDOR data. *Appl Magn Reson* **2006**, *30*, 473–498.
- (88) Abdullin, D.; Brehm, P.; Fleck, N.; Spicher, S.; Grimme, S.; Schiemann, O. Pulsed EPR Dipolar Spectroscopy on Spin Pairs with one Highly Anisotropic Spin Center: The Low-Spin FeIII Case. *Chem. Eur. J* **2019**, *25*, 14388–14398.
- (89) Decroos, C.; Li, Y.; Soltani, A.; Frapart, Y.; Mansuy, D.; Boucher, J.-L. Oxidative decarboxylation of tris-(p-carboxyltetraaryl)methyl radical EPR probes by peroxidases and related heme proteins: intermediate formation and characterization of the corresponding cations. *Arch. Biochem. Biophys.* **2010**, *502*, 74–80.
- (90) Kuzhelev, A. A.; Trukhin, D. V.; Krumkacheva, O. A.; Strizhakov, R. K.; Rogozhnikova, O. Y.; Troitskaya, T. I.; Fedin, M. V.; Tormyshev, V. M.; Bagryanskaya, E. G. Room-Temperature Electron Spin Relaxation of Triarylmethyl Radicals at the X- and Q-Bands. *J. Phys. Chem. B* **2015**, *119*, 13630–13640.
- (91) Shevelev, G. Y.; Krumkacheva, O. A.; Lomzov, A. A.; Kuzhelev, A. A.; Rogozhnikova, O. Y.; Trukhin, D. V.; Troitskaya, T. I.; Tormyshev, V. M.; Fedin, M. V.; Pyshnyi, D. V.; et al. Physiological-temperature distance measurement in nucleic acid using triarylmethyl-based spin labels and pulsed dipolar EPR spectroscopy. *J. Am. Chem. Soc.* **2014**, *136*, 9874–9877.
- (92) Giannoulis, A.; Yang, Y.; Gong, Y.-J.; Tan, X.; Feintuch, A.; Carmieli, R.; Bahrenberg, T.; Liu, Y.; Su, X.-C.; Goldfarb, D. DEER distance measurements on trityl/trityl and Gd(III)/trityl labelled proteins. *Phys. Chem. Chem. Phys.* **2019**, *21*, 10217–10227.
- (93) Song, Y.; Liu, Y.; Hemann, C.; Villamena, F. A.; Zweier, J. L. Esterified dendritic TAM radicals with very high stability and enhanced oxygen sensitivity. *J. Org. Chem.* **2013**, *78*, 1371–1376.
- (94) Chen, H.; Maryasov, A. G.; Rogozhnikova, O. Y.; Trukhin, D. V.; Tormyshev, V. M.; Bowman, M. K. Electron spin dynamics and spin-lattice relaxation of trityl radicals in frozen solutions. *Phys. Chem. Chem. Phys.* **2016**, *18*, 24954–24965.
- (95) Jeschke, G.; Polyhach, Y. Distance measurements on spin-labelled biomacromolecules by pulsed electron paramagnetic resonance. *Phys. Chem. Chem. Phys.* **2007**, *9*, 1895–1910.
- (96) Schweiger, A.; Jeschke, G. *Principles of Pulse Electron Paramagnetic Resonance*; illustrated, reprint.; Oxford University Press, 2001.
- (97) Hagelueken, G.; Ward, R.; Naismith, J. H.; Schiemann, O. MtsslWizard: In Silico Spin-Labeling and Generation of Distance Distributions in PyMOL. *Appl Magn Reson* **2012**, *42*, 377–391.
- (98) Bobko, A. A.; Kirilyuk, I. A.; Grigor'ev, I. A.; Zweier, J. L.; Khramtsov, V. V. Reversible reduction of nitroxides to hydroxylamines: roles for ascorbate and glutathione. *Free Radic. Biol. Med.* **2007**, *42*, 404–412.
- (99) Sunda, W. G.; Huntsman, S. A. Regulation of cellular manganese and manganese transport rates in the unicellular alga *Chlamydomonas* 1. *Limnol. Oceanogr.* **1985**, *30*, 71–80.
- (100) Widder, P.; Schuck, J.; Summerer, D.; Drescher, M. Combining site-directed spin labeling in vivo and in-cell EPR distance determination. *Phys. Chem. Chem. Phys.* **2020**, *22*, 4875–4879.
- (101) Brewer, C. F.; Riehm, J. P. Evidence for possible nonspecific reactions between N-ethylmaleimide and proteins. *Anal. Biochem.* **1967**, *18*, 248–255.
- (102) Rhee, S. G.; Chae, H. Z.; Kim, K. Peroxiredoxins: a historical overview and speculative preview of novel mechanisms and emerging concepts in cell signaling. *Free Radic. Biol. Med.* **2005**, *38*, 1543–1552.
- (103) Ziegler, D. M. Role of reversible oxidation-reduction of enzyme thiols-disulfides in metabolic regulation. *Annu. Rev. Biochem.* **1985**, *54*, 305–329.